Peder Sørlie Rustad

Bimetallic Aluminum - Copper Hybrid Metal Extrusion & Bonding Welded Electrical Busbars

Master's thesis in Mechanical Engineering - TMM4960
Supervisor: Filippo Berto
July 2021

Master's thesis

NTNU
Norwegian University of Science and Technology
Faculty of Engineering
Department of Mechanical and Industrial Engineering

NTNU
Norwegian University of
Science and Technology

Peder Sørlie Rustad

Bimetallic Aluminum - Copper Hybrid Metal Extrusion & Bonding Welded Electrical Busbars

Master's thesis in Mechanical Engineering - TMM4960
Supervisor: Filippo Berto
July 2021

Norwegian University of Science and Technology
Faculty of Engineering
Department of Mechanical and Industrial Engineering

Department of Mechanical
and Industrial Engineering

Department of Mechanical Engineering

TMM4960 - Master's Thesis

Bimetallic Aluminum - Copper Hybrid Metal Extrusion & Bonding Welded Electrical Busbars

Author:
Peder Sørlie Rustad

July, 2021

Abstract

Interest in dissimilar metal welding for electrical applications is increasing. Aluminum (Al) - Copper (Cu) connections were originally bolted, but due to the frequent maintenance required, solid-state bonding techniques have been sought after for bonding Al - Cu conductors. The Hybrid Metal Extrusion & Bonding (HYB) is a new solid-state welding technique. HYB has been used to bond various metals and metal combinations, but this thesis will cover its capability when bonding Al - Cu. Al - Cu HYB bonded samples are tested and analyzed in regard to their usability as electrical busbars. Electrical busbars require good mechanical properties for their structural integrity. Electrical properties and mechanical properties are also highly linked, making mechanical properties a good indicator of electrical properties. Intermetallic Compounds (IMCs) are produced at the interface of the weld. IMCs are needed to create a bond, but have inherently more resistivity and brittle properties; deteriorating both the electrical and the mechanical properties. IMC layers grow at high temperatures making them important factors in how the busbars need to be dimensioned. A small cross-section will decrease its lifetime by the rapid growth of IMC. The thesis measured IMC growth by using Transmission Electron Microscope (TEM) and TEM Energy Dispersive X-ray Spectroscopy (EDX), as well as using Scanning Electron Microscope (SEM) and SEM EDX. Samples were heated up at two different temperatures; 200 °C and 250 °C. The data from these temperatures made both an isothermal and isokinetic model for the HYB IMC growth. The conductivity of one unheated HYB sample, as well as three HYB samples heated at 250 °C was tested. Electrical measurements found an increase in resistance at the weld interface for all samples, but the measurement errors were too big to show how much the resistance increase, was caused by IMC growth.

Abstract

Interessen for ulik metallsveising for elektriske applikasjoner øker. Aluminium (Al) - Kobber (Cu) forbindelser var opprinnelig boltet, men på grunn av hyppig vedlikehold har kaldsveis bindingsteknikker vært ettertraktet for binding av Al - Cu ledere. Hybrid Metal Extrusion Bonding (HYB) er en ny kaldsveiseteknikk. HYB har blitt brukt til å binde forskjellige metaller og metallkombinasjoner, men denne oppgaven vil dekke dens kapasitet ved binding av Al - Cu. Al - Cu HYB bundne prøver testes og analyseres når det kommer til deres brukbarhet som elektriske samleskinner. Elektriske samleskinner krever gode mekaniske egenskaper for deres strukturelle integritet. Elektriske egenskaper og mekaniske egenskaper er også sterkt koblet sammen, noe som gjør mekaniske egenskaper til en god indikator for elektriske egenskaper. Intermetalliske forbindelser (IMCs) produseres ved grensesnittet til sveisen. IMC er nødvendig å skape et bånd, men har iboende mer motstand og sprø egenskaper. IMC-lag vokser ved høye temperaturer og det er viktige faktorer i hvordan samleskinnene må dimensjoneres. Et lite tverrsnitt vil redusere levetiden ved rask vekst av IMC. Oppgaven målte IMC-vekst ved hjelp av Transmisjonselektronmikroskop (TEM) og TEM Energy Dispersive X-ray Spectroscopy (EDX), samt å bruke Scanning Electron Microscope (SEM) og SEM EDX. Prøver ble varmet opp ved to forskjellige temperaturer; 200 °C og 250 °C. Dataene fra disse temperaturene laget både en isotermisk og isokinetisk modell for HYB IMC-veksten. Ledningsevnen av en uoppvarmet HYB-prøve, samt tre HYB-prøver oppvarmet til 250 °C ble testet. Elektriske målinger fant en økning i motstand ved sveisegrensesnittet for alle prøvene, men målefeilene var for store til å vise hvor mye motstandsøkningen ble forårsaket av IMC-vekst.

Preface and Acknowledgements

This master thesis is written during the spring semester of 2021 to fulfill the requirement for the MSc degree at the Department of Mechanical and Industrial Engineering (MTP) at the Norwegian University of Science and Technology (NTNU) in Trondheim, Norway. The supervisor for this thesis has been Professor Filippo Berto.

I want to thank the doctoral candidate Aksel Elkjaer as his cooperation and insight has been instrumental throughout the entirety of this project. I would also like to thank Professor Øystein Grong for his willingness to help by sharing his knowledge on HYB and diffusion theory. Furthermore, the help by Berit Kramer has been essential to achieving such good SEM results after struggling with grinding and polishing for most of the master thesis, and the whole pre-master project. Lastly, I would like to thank everyone who assisted me with this work. For this, I am very grateful.

Abbreviations

Al Aluminum.

AS Advancing Side.

BM Base Material.

BSE Backscattered Electrons.

Cu Copper.

CUT Conductor Under Test.

EDX Energy Dispersive X-ray Spectroscopy.

EV Electric vehicle.

EZ Extrusion Zone.

Fe Steel.

FIB Focused Ion Beam.

FM Filler Material.

FSW Friction Stir Welding.

GMAW Gas Metal Arc Welding.

HAZ Heat Affected Zone.

HV Hardness Vickers.

HYB Hybrid Metal Extrusion & Bonding.

IACS International Annealed Copper Standard.

IMC Intermetallic Compound.

NTNU Norwegian University of Science and Technology.

OM Optical Microscope.

RS Retreating Side.

SE Secondary Electrons.

SEM Scanning Electron Microscope.

STEM Scanning Transmission Electron Microscope.

SZ Stir Zone.

TEM Transmission Electron Microscope.

Contents

List of Figures iii

List of Tables v

1 Introduction 1

1.1 Busbar . . . 1

1.2 Metals for busbars . . . 2

2 Hybrid Metal Extrusion & Bonding 4

2.1 HYB busbar specification . . . 6

2.1.1 HYB busbar materials . . . 6

2.1.2 HYB busbar manufactor method . . . 7

2.2 Mechanical properties . . . 7

2.2.1 Hardness test . . . 8

2.2.2 Tensile test . . . 9

2.2.3 Bending test . . . 10

3 Conductivity and Structure in Intermetallic Compounds 11

3.1 Conductivity overview . . . 11

3.1.1 Type of circuit . . . 11

3.2 Intermetallic compounds . . . 13

3.3 Al - Cu intermetallic compounds . . . 13

3.4 Intermetallic phases . . . 14

3.5 Intermetallic conductivity . . . 16

4 Conductivity test 18

4.1 Test method . . . 18

4.2 Setup . . . 20

4.3 Dimensions . . . 22

4.4 Electrical measurement results . . . 24

5 IMC Growth Diffusion 29

5.1 Fick's law . . . 30

5.2 Diffusion coefficient . . . 31

5.3 Fick's second law . . . 33

5.4 Binary alloy diffusion . . . 33

5.5 Isothermal IMC thickness model . . . 35
5.6 Isokinetic IMC thickness model . . . 36

6 Aluminum Copper Diffusion Bonding from Literature 37
6.1 Liu et al. . . . 39
6.2 Xu et al. . . . 40
6.3 Braunovic and Aleksandrov . . . 41
6.4 Kim et al. . . . 42
6.5 Comparison . . . 43

7 Observing IMC thickness 44
7.1 Optical microscope . . . 44
7.2 Scanning electron microscope . . . 45
7.3 IMC thickness measurments . . . 47
7.3.1 Unheated 6101 TEM samble . . . 47
7.3.2 Heated samples . . . 50
7.3.3 200 degrees Celsius . . . 50
7.3.4 250 degrees Celsius . . . 51
7.4 HYB intermetallic growth model . . . 52

8 Discussion 55
8.1 structural . . . 55
8.2 Conductivity . . . 55
8.3 IMC thickness model . . . 55

9 Conclusion 58

Bibliography 59

Appendix 63
A Busbar specifications . . . 63
B Temperature increase code . . . 63
C Error function plotter . . . 66
D Diffusion Coefficient . . . 67
E Isothermal IMC growth model . . . 68
F Isokinetic growth model . . . 69
G Calculate interdiffusion coefficient from experimental data . . . 70
H Calculate the relationship between measured and average area . . . 71

I Hardness plots 73
J TEM EDX 74
K Distance from interface to wires 76
L SEM EDX analysis 78
M IMC phase characterization 80
N Excel files 82
O Pre-master project 82

List of Figures

1 Battery capacity trend 2
2 Temperature increase with equal volume 3
3 Temperature increase with equal weight 4
4 HYB machine illustration 5
5 HYB machine illustration and picture 5
6 Conductivity and hardness after heat treatment 6
7 HYB weld illustration 7
8 HYB groove and 7
9 Hardness result plotted 8
10 Hardness result plotted 9
11 HYB tensile test 1 10
12 HYB tensile test 2 10
13 HYB weld bending test 10
14 Series and parallel circuit 12
15 Cold roll weld, peeling force to IMC width graph 13
16 Al - Cu phase diagram 14
17 Phase and total interdiffusion coefficient 15
18 Schematic illustration of possible IMC layers 16
19 IMC in parallel 17
20 IMC growth and resistivity at 250°C 17
21 IMC in series 18
22 Four-terminal sensing schematic drawing 19
23 Two-terminal sensing schematic drawing 19
24 Voltage drop plot with no IMC resistance 20
25 Voltage drop plot with 5 microvolts IMC voltage drop 21

26 IMC growth and resistivity at 250°C 21
27 Jig wires and measuring hole for interface distance 22
28 Interface outlined 23
29 E0 and E1 cross section area relationship with linear functions 24
30 E2 and E3 cross section area relationship with linear functions 24
31 E0 graph 25
32 E0 graph zoomed 25
33 E1 graph 26
34 E1 graph zoomed 26
35 E2 graph 27
36 E2 graph zoomed 27
37 E3 graph 28
38 E3 graph zoomed 28
39 Self-diffusion schematic drawing 29
40 Interdiffusion schematic drawing 29
41 Crystal lattice illustration 30
42 Al and Cu diffusion high temperature 31
43 Al and Cu diffusion high temperature with regression line 32
44 Al and Cu diffusion coefficient high temperature with regression line 32
45 Fick's second law schematic illustration 33
46 Flux sum schematic illustration 34
47 Concentration dependent on position and time 35
48 Phase interdiffusion coefficient 37
49 Phase and total interdiffusion coefficient 38
50 Shift in interdiffusion coefficient 39
51 Liu et al. interdiffusion coefficient 40
52 Xu et al. interdiffusion coefficient 41
53 Braunovic and Aleksandrov interdiffusion coefficient 42
54 Kim et al. interdiffusion coefficient 43
55 IMC growth from literature 44
56 Macro perspective 45
57 50 and 200 magnification of HYB weld 45
58 500X magnification OM 45
59 Unheated 100X and 1000X magnification of HYB weld in SEM 46
60 30kX magnification SEM 46

61 TEM sample post FIB . . . 47
62 TEM sample post FIB . . . 48
63 TEM sample post FIB . . . 49
64 TEM EDX concentration profile . . . 50
65 SEM SE 200°C . . . 51
66 SEM BSE 200°C . . . 51
67 250°C for 242 h and 430 h SEM images . . . 52
68 250°C for 731 h SEM image . . . 52
69 200°C and 250°C temperature and time growth . . . 53
70 Interdiffusion from experimental data at 200°C and 250°C . . . 53
71 HYB k value . . . 54
72 IMC growth from experimental data at different temperatures . . . 54
73 Isothermal growth with HYB . . . 56
74 Liu et al. and HYB comparison . . . 56
75 Temperature in HYB weld . . . 57
76 Isokinetic solution for IMC thickness in welding . . . 57

List of Tables

1 Conductivity and density properties for Al and Cu. . . . 3
2 AA6101 chemical composition . . . 6
3 AA6082-T4 chemical condition . . . 6
4 The achievable phases using the HYB method with composition properties, Pearson Symbol (PS), Space Group (SG), and Lattice Parameters . . . 15
5 IMC phase resistivity and temperature coefficeint . . . 16
6 Electrical sample matrix . . . 22
7 Electrical sample matrix . . . 23
8 Electrical sample results . . . 29
9 Cu and Al diffusion coefficients at high temperatures . . . 31
10 Liu et al. interdiffusion coefficient at different temperatures[71] . . . 39
11 Xu et al. interdiffusion coefficient . . . 40
12 Braunovic and Aleksandrov interdiffusion coefficient . . . 41
13 Kim et al. interdiffusion coefficient . . . 42
14 IMC thickness sample matrix . . . 47
15 IMC thickness measurements with standard deviation and standard error . . . 52

1 Introduction

There is a big incentive towards substituting Copper (Cu) with Aluminum (Al) in electrical applications. Al is around two times as conductive as Cu per kilogram. However, Cu is around one and a half times as conductive per square meter. Using Al will cut costs as Al is approximately a quarter of the price of Cu [1]. The cost and weight advantage as well as the abundant amount of Al drives the industry to use Al in electric applications[2, 3]. Using Cu with Al requires a way of connecting the two metals. These connections were originally bolted, but they need regular maintenance due to the connections loosening by creep[4]. The conventional welding techniques like Gas Metal Arc Welding (GMAW), are unable to bond Al - Cu. The metals do not bond well when they are melted as the solidification process creates hard and brittle Intermetallic Compounds (IMCs). Therefore, solid-state welding has been utilized to bond these metals. The solid-state welding techniques that have been either utilized or studied for Al - Cu bonding, include diffusion, friction, cold roll and ultrasonic welding[5, 6, 7, 8]. These welding methods have all been characterized and compared in the pre-master project[9]. The nature of Al - Cu welding has proved a great challenge. Combinations of solid-state welding techniques are studied as well, but there is not a lot of data. Hybrid Metal Extrusion & Bonding (HYB) is a relatively new solid-state welding technique. The technique has been studied with various metals and metal combinations. It has so far shown promise with its Al - Al welding as well as Al - Fe welding[10, 11, 12, 13].

This thesis aims to give a sound report on how the HYB performs as a busbar in electrical applications. A busbar requires acceptable structural integrity by a solid bond. In addition, mechanical properties are closely tied to electrical properties, as voids and other weld defects increase electrical resistance[14]. Initial tensile, initial bending, and hardness tests are produced to characterize its structural integrity and give an indication of the electrical performance. Current can heat up the busbar making it operate at temperatures above 120 °C. This is above the activation energy for Al and Cu which allows for the movement of their atoms. The movement of atoms is a diffusion process that creates IMC growth. IMCs are highly electrical resistant and brittle which deteriorates both mechanical and electrical properties[15]. A model was created to determine how fast the IMC grows with regards to temperature and time. This allows for the prediction of the lifetime for the HYB busbar. To achieve this, five samples were used to measure IMC layer thickness; one unheated, one at 200 °C and three at 250 °C heated samples. The three samples heated at 250 °C were all heated for different times. Electrical resistance was also measured. To compare the electrical resistance with IMC thickness, one unheated and three samples heated at 250 °C were used. The three samples were heated together with the IMC thickness samples for the same amount of time. This ensures the same IMC thickness for both the electrical and IMC thickness measurement samples.

1.1 Busbar

A busbar is a metallic strip or a bar used in electric power distribution. It is usually housed inside a type of enclosure where it allows for local high current power distribution. It has mechanical integrity which allows for it to stand on pillars. They are most often not insulated and the pillar support allows for them to be cooled by the surrounding air. Busbars are designed for large amounts of current to pass through and are used in applications like battery packs and electrical switchyards. A wide array of cable connections can be substituted by a busbar structure, which can help with layout problems of high-density electronic systems. Other advantages are anti-interference, excellent high-frequency filtering effect, space-saving, reliability, quick assembling, less complicated, and low inductance. There are mainly seven different types of busbars. The type is selected depending on the circumstances, the factors include current, voltage, reliability, frequency environment, safety, etc. The seven types are divided into the following:

1) Open phase conductors insulated by the air.
2) Different phase conductors with segregating barriers, insulated by the air.
3) The structure is like type (1) and (2), but is totally enclosed.
4) Isolated phase busbars: an earthed enclosure where the different phases are fully isolated from

each other through the air.
5) Force-cooled busbar: the structure is like type (1) to (2), however, it uses a cooling medium like water or air where it is applied using for example a pump or fan.
6) the structure is like type (5), however, it uses gasses like hexafluoride or sulfur for cooling instead of air.
7) A totally enclosed system with an insulation medium like an oil compound.

There are four common joining methods for busbars. These should have low resistance and the resistance should be roughly constant throughout the joint's lifetime. Welding is one way of joining busbars and the advantage is the potential resistivity in the joint being the inherent resistivity of the base materials (BMs). A drawback is the difficulty in installation, and welding can be difficult depending on the metal/metals. The joint can be created through clamping as well, and these have many advantages with the downside being it's high cost. Clamping is easy and the joint interface area is controllable enabling cooling at the joint. Clamping creates an even contact pressure and is easy to assemble. Bolted connections are easy, versatile, and reliable. However, they create a distortion in the current flow lines and the bolts aren't able to apply a constant contact pressure. Another downside is its shorter lifetime compared to other joining methods. Riveted joining methods are highly efficient, but are more difficult to undo or tighten compared to bolted connections. Installation is also more complicated [16].

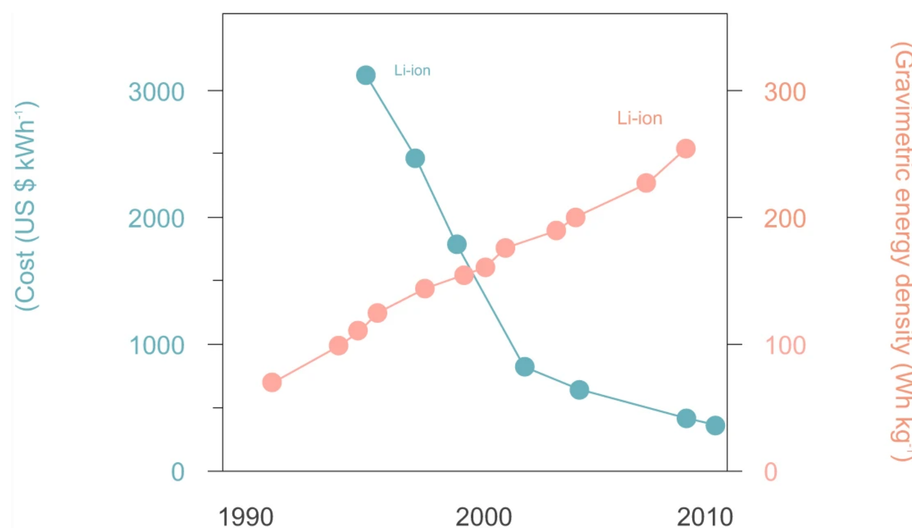

Figure 1: Battery capacity trend.

Source: [17]

Battery packs are widely used in electric vehicles (EVs). Busbar strips and bars are vital to the battery systems. A busbar carries all the current in a system which is necessary for any EV. The last decade has seen a rising trend in EV market share. In addition to the technological innovations making the EVs better, a subsidiary approach from many governments in Europe and around the world has made the trend even more likely to continue [18]. Technological advancements has seen innovation in batteries and improvements within each battery technology. There has been many advancements in lithium-ion cells and figure 1 shows the improvements made both in cost to capacity (kWh) and gravimetric energy density (Whkg).

1.2 Metals for busbars

The increasement in capacity for these battery cells will increase the size of the busbars. A busbar is limited to how much current it can carry by the materials resistivity and the cross-section area. A larger cross-section allows for more current due to lower resistance. Both environmental and cost is a driver to decrease the weight of busbars in vehicles. Cu is the most conventional metal in

busbars, but Al is also widely used. These materials adhere most to the requirements for busbars. The requirements include low electrical and thermal resistivity, good mechanical properties like high resistance to corrosion, fatigue failure, and high shear, tension, and compression strength. These materials are also the most cost-efficient. Cu has a better conductivity to volume ratio while the Al has a better conductivity to weight ratio shown in table 1.

Property	Copper	Aluminum
Conductivity $(m/\Omega mm^2)$	58	35.5
Density (g/mm^3)	8.93	2.70

Table 1: Conductivity and density properties for Al and Cu.

Source: [1]

Al gives more conductivity for the cost compared to Cu, but is more complicated due to Al being the more reactive metal. Al is therefore very susceptible to galvanic corrosion[19]. Figure 2 predicts the temperature increase from an iterative script shown in Appendix B with equal volume having a cross-section area of 75 mm^2 and 100 amps running through the material. It shows the copper outperforming the aluminum over time. This is due to the lower resistance per area. Note that the script does not calculate dissipating heat making it unrealistic. The script uses the theory described in section 3.1.

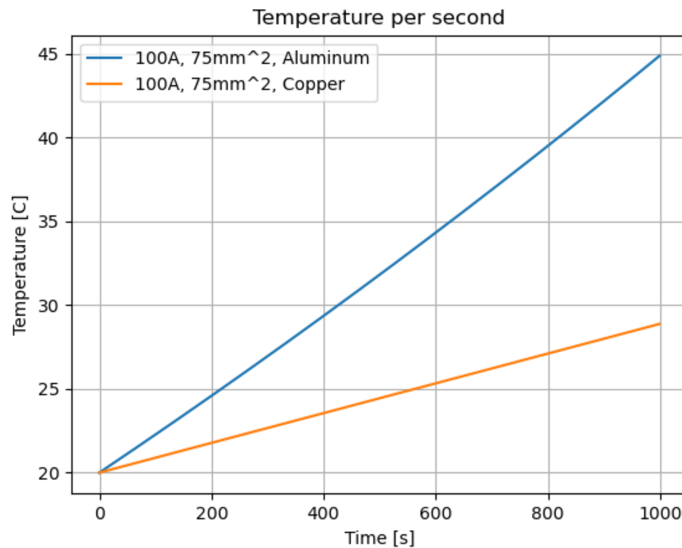

Figure 2: Temperature increase with equal volume.

Source: This work.

Figure 3 has the same script with 100 amps predicting the temperature increase when Cu and Al. The difference this time is that the Al has a cross-section that is 3.3 times larger than Cu. At that cross-section Al and Cu has the same weight. Figure 3 shows Al vastly outperforming Cu when they are the same weight. The large inherent weight of the Cu in conjunction with its higher cost have made bimetallic busbars attractive[20]. Dissimilar metal welded busbars either have the metals transfer current in parallel or in series. Two common ways of welding parallel busbars are with cold roll and diffusion welding. Cu is placed around the aluminum and thereafter bonded through pressure and temperature. They offer financial and weight saving benefits over copper. When comparing a Cu pole to the Al - Cu bimetallic pole, the bimetallic pole was found to be 40 - 60 % lighter and 30 - 40 % less expensive[21].

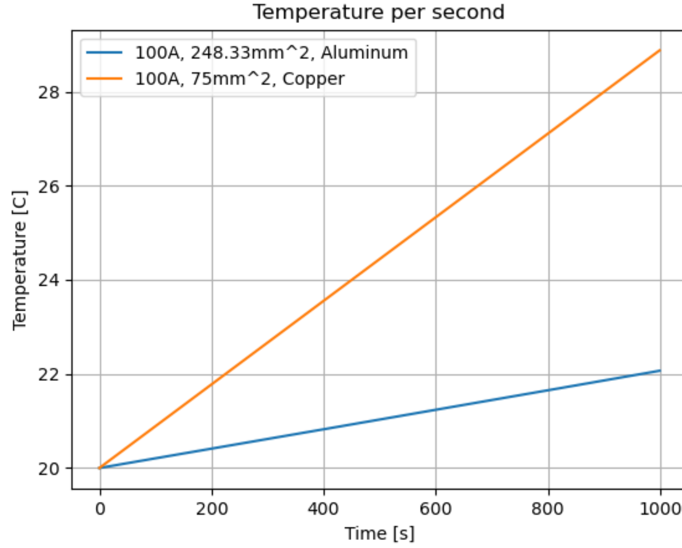

Figure 3: Temperature increase with equal weight.

Source: This work.

2 Hybrid Metal Extrusion & Bonding

HYB welding is a solid-state joining process where two metal plates or sheets called Base Materials (BMs), are held in place. Butt jointing is the usual procedure, but it has the capability to create both tee joints and corner joints. A gap is left between the two metals which are filled out by a Filler Material (FM). The filled-out zone is called the Extrusion Zone (EZ). A rotating tool extrudes the FM in the form of a wire and is pressed down onto and between the BMs. The tool inhibits grooves acting as dies where the wire is fed through. As the pin/extrusion head rotates, the wire is fed through due to the friction applied by the grooves. The grooves on the extrusion head are open, which means the wire is exposed to the BMs once it gets past the shoulder. The Helicoid-shaped dies on the extrusion head prevents pressure from dropping during welding, an important mechanism that allows continuous FM extrusion. The velocity of the filler wire (v_w) is given with relation to the spindle radius (r_s), wire slipping in the die (β), and spindle rotation speed (N_s). The relation is shown in equation 1[22].

$$v_w = \beta \cdot N_s \cdot \frac{2\pi r_s}{60} \tag{1}$$

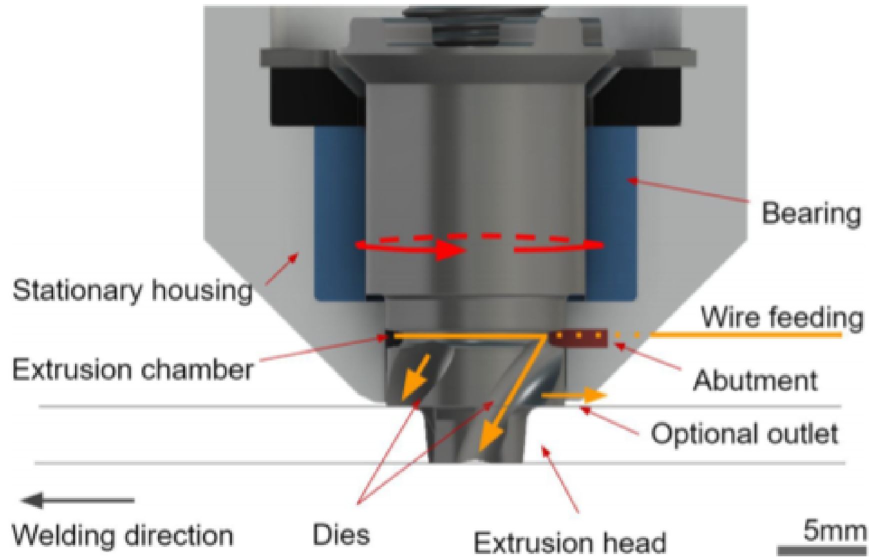

Figure 4: HYB machine illustration

Source: [22]

Friction is generating heat and plasticizing the BMs. Almost all the mechanical work applied on the metals is converted to heat, approximately 95 %. The CO_2 cooling system shown in Figure 5b allows most of this heat to be absorbed by the extrusion head[22] which has a positive effect, reducing the Heat Affected Zone (HAZ). When the FM is being extruded through the extrusion head, it plasticizes together with the BMs. This in turn makes it possible for the filler to bond with the BMs[23]. Furthermore, the FM takes a lot of the deformation in the welding process which would otherwise be applied to the BMs. This makes the welding process more flexible and less susceptible to undercuts and other weld defects when compared to more conventional solid-state joining techniques. An important factor when the weld is of dissimilar metals is where the BMs are placed with regard to the pin rotation and welding direction. The side that makes contact with the pin having the same rotation direction as the welding direction, is called the Advancing Side (AS). The side which makes contact with the pin having a rotation direction opposite of the welding direction is called the Retreating Side (RS). Figure 7 illustrates the Al - Cu HYB weld where Cu is on the AS and Al on the RS. Apart from cold roll welding, reports on operating temperature measures lower for HYB than other solid joining processes, which includes the often compared Friction Stir Welding (FSW) method[10].

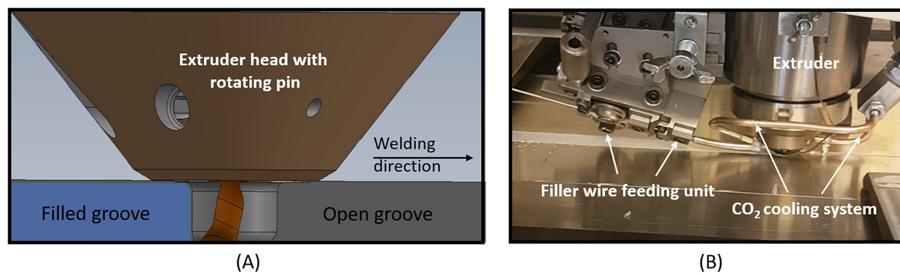

Figure 5: HYB machine illustration (A) and picture (B)

Source: [22]

2.1 HYB busbar specification

2.1.1 HYB busbar materials

The FM and Al BM are both AlMgSi - Alloys (AA6xxx). Several studies have shown that AA6xxx series have good mechanical and electrical properties through thermomechanical processing. The AA6xxx series is also able to maintain good properties after undergoing severe plastic deformation, making the alloy a good candidate for a Al - Cu HYB welded busbar[24, 25, 26]. The Al BM is an AA6101 provided by Hydro. All the previously mentioned benefits apply to this alloy. The alloy is produced through extrusion or cold rolling and is heat treatable. Isothermal heat treatment has shown to increase the conductivity substantially. Cyclical heat treatment increases conductivity at a higher rate than constant heat. Hardness seems to increase with heat treatment up to 90 HV before declining. Conductivity will however continue to increase. This is demonstrated in Figure 6 where the blue plots represent a cyclical temperature test while the red is non - cyclical. The heat set for both the cyclical and non - cyclical test was 170°C[27]. The conductivity effect on AA6101 heated for days is unknown. The alloy used in the HYB weld is produced through cold rolling, but further treatment was not provided by Hydro. However, hardness tests to the Al BM shown in Figure 10 can be compared to Figure 6b. It is very plausible this alloy is heat-treated to be conductivity optimized, the hardness result would then be a match.

Alloy	Si	Fe	Cu	Mn	Mg	Cr	Zn	Ti	B	Others
6101	0.3-0.7	0.5	0.1	0.03	0.35-0.8	0.03	0.1	-	0.06	0.1

Table 2: AA6082-T4 chemical composition.

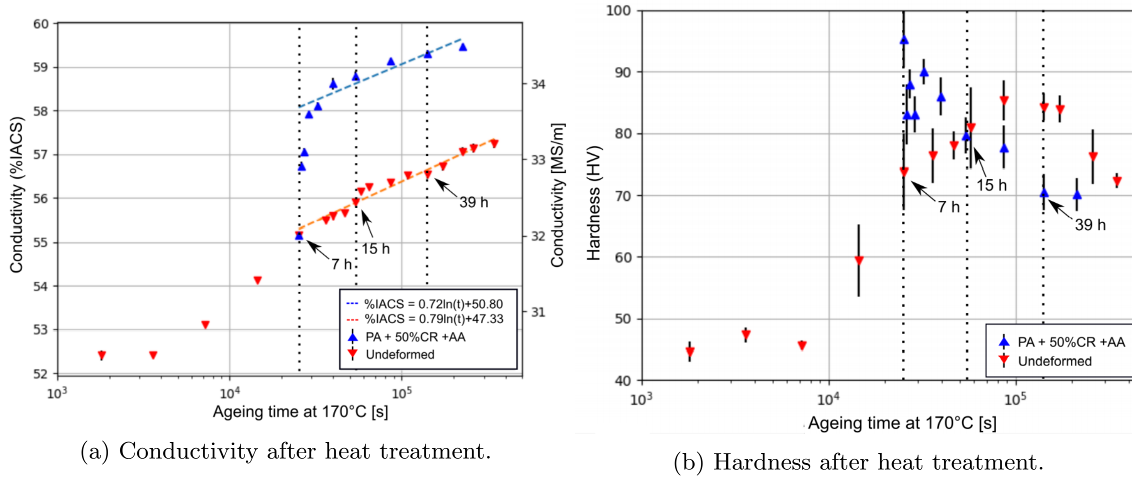

(a) Conductivity after heat treatment.

(b) Hardness after heat treatment.

Figure 6: Conductivity and hardness after heat treatment.

Source: [27]

The filler material is an AA6082 - T4. The chemical composition is shown in table 3. The Al is cast with the desired alloying elements. Mixing of the alloys is done before a direct-chill casting. IMC formation occurs as non - equilibrium phases but undergoes a homogenization process to convert the phases to be in equilibrium. The alloy is homogenized by heating to 540°C for 2 hours and 15 minutes before it is cooled. The heating rate is around 200°C/h and the cooling rate is around 300°C/h[28].

Alloy	Si	Mg	Cu	Mn	Fe	Cr	Zr	Ti	B	others
6082-T4	1.11	0.61	0.002	0.51	0.2	0.14	0.13	0.043	0.006	0.029

Table 3: AA6082-T4 chemical condition.

2.1.2 HYB busbar manufactor method

The busbars were constructed by welding two 3 mm Cu plates on each side of a 3 mm Al plate. As Cu is the harder material, it was placed on the Advancing Side (AS) of the welding pin. Having Cu on the Retreating Side (RS) would create a bad weld as reported by Hursanay[29]. The pin rotation was set to 350 RPM and the welding speed was 12 mm/s and 9 mm/s depending on the plate. The busbars were cut out to be 25 mm wide illustrated in Figure 7. Every busbar weld was visibly consistent apart from the two coming from each end of the plate. Defects at the start and end position were clearly visible although 9 mm/s created fewer defects compared to 12 mm/s. Holes were then machined out to create a bolted connection point for electrical current.

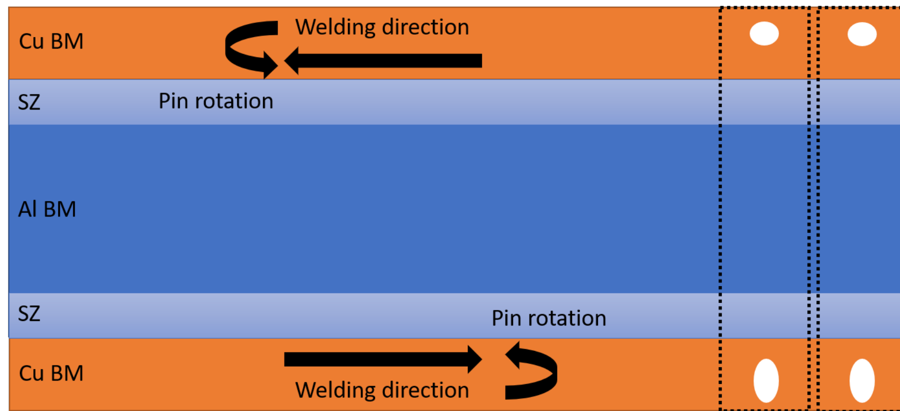

Figure 7: HYB weld illustration.

Source: This work.

Figure 8 illustrates the position of the plates. The BMs are ground with 150 grit mesh sandpaper and cleaned with acetone. Both on top where the shoulder is in contact, and on the side where the pin is in contact. The distance between the BMs is 4 mm. The pin diameter is 7 mm and penetrates the Al BM. HYB has shown to create dissimilar metal bonding without the pin making contact with the harder material[11]. In this case, the pin keeps a slight contact with the Cu BM throughout the weld. Multiple plates were welded and some showed some disbursement of Cu and some showed no disbursement.

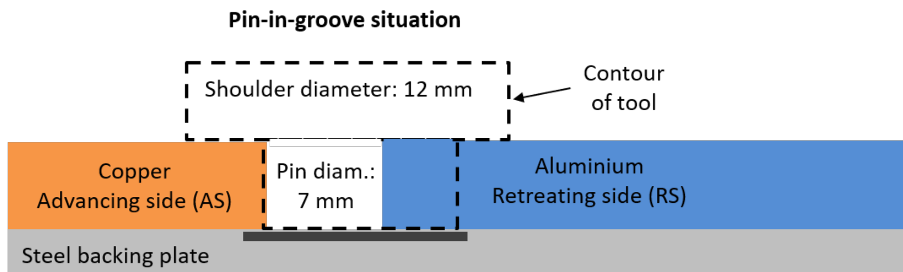

Figure 8: HYB machine illustration (A) and picture (B)

Source: [13]

2.2 Mechanical properties

Initial mechanical tests were conducted on HYB samples. The mechanical properties are strongly correlated with electrical properties. Busbars can also be under strenuous conditions requiring a solid bond. The weld was tested with regard to bending and strength (tensile testing). The purpose of these is to determine where the weak point of the weld is. As these tests are of dissimilar metal

bonds, no standard was used for the tensile and bending tests, meaning these results can differ slightly from what would be the true mechanical properties. During the pre-master project, the weld was hardness tested[9]. One AA6101 - Cu weld was cut out into a specimen. This specimen was tested and ground down to be tested again resulting in three hardness tests. Figure 9 shows all plots from the testes. The values can be seen with standard error and deviation in Appendix I.

2.2.1 Hardness test

The hardness profile shows numerous properties of the weld interface. HAZ characteristics are determined as well as the hardness of the BMs. Hardness is also correlated to tensile strength demonstrating where a fracture should occur during a tensile test. Each indent is placed 0.5 mm apart resulting in 40 measurements along the 2 cm long specimen. The position of the indenter needs to be recalibrated each time the specimen is ground down and polished. This is a manual process using the microscope in conjunction with a distance instrument. All three tests had the last Al indent at 3.5 mm on the specimen, and the first Cu indent at 4.0 mm. This indicates a moderately accurate position for the indenter on all tests.

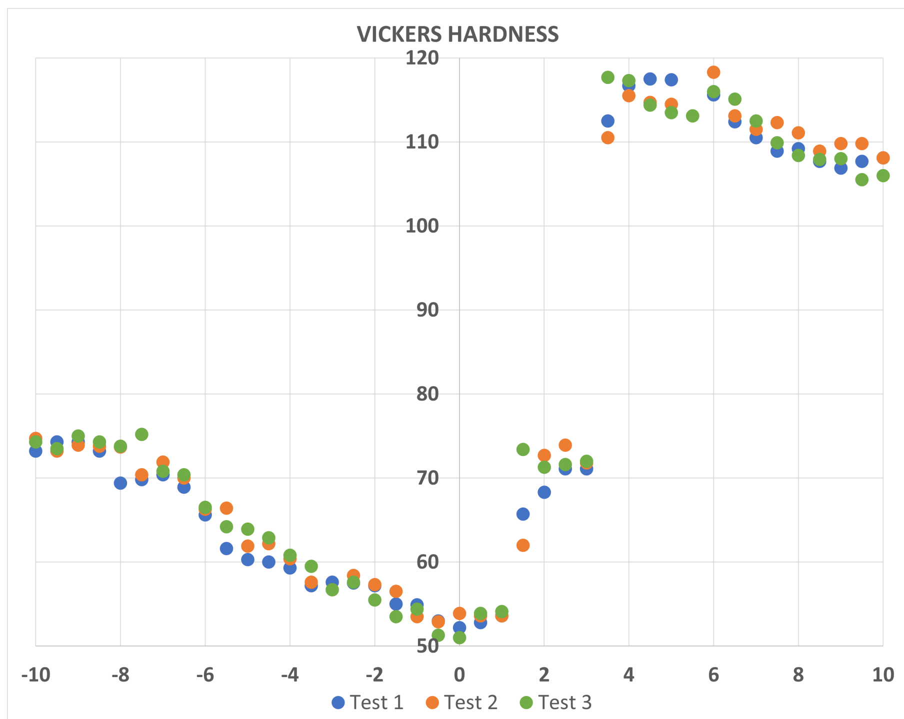

Figure 9: Hardness results plotted.

Source: [9]

A more comprehensible graph is made by using the standard deviation to create the standard error (SE). This represents the error in each measurement better. The standard error for the plot on each point of the weld was calculated using equation 2 and 3.

$$S = \sqrt{\frac{\sum(X_i - \bar{X})^2}{N}} \quad (2)$$

S = Standard deviation
X_i = Specific value from population
$\bar{X}$ = Mean value from population
N = Total population, which is equal to three in all cases

$$SE = \frac{S}{\sqrt{N}} \tag{3}$$

SE = Standard error

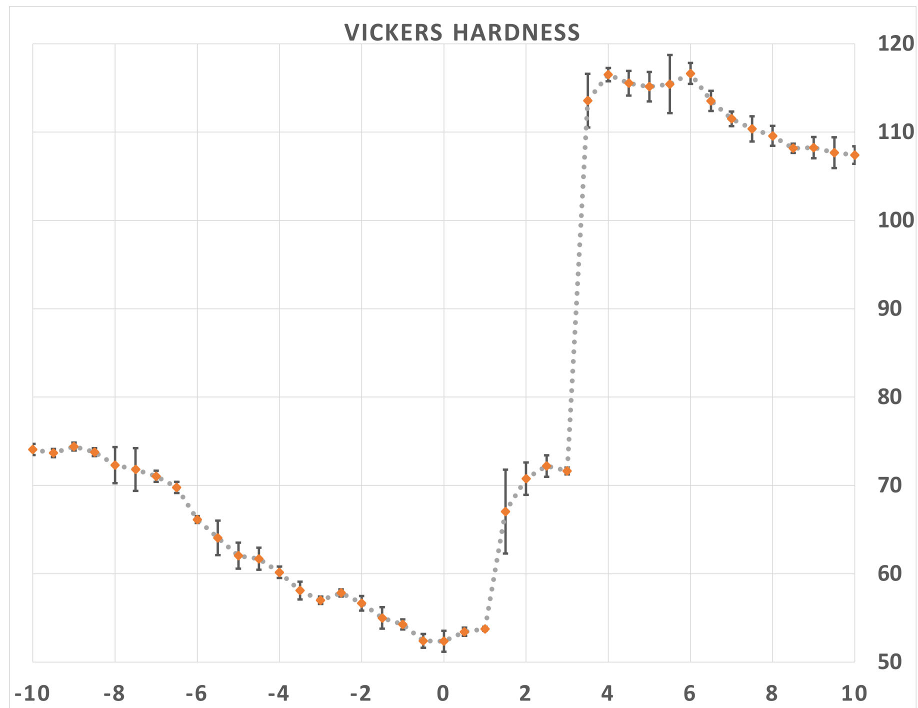

Figure 10: Hardness results plotted.

Source: [9]

The HAZ affects Al differently compared to Cu. Al experiences a strain softening while Cu a strain hardening. The hardness profile in Al shows the weakest point is 3.5 mm from the weld interface indicating that is where it should fracture during a tensile test. Total HAZ width is 18 mm. However 6 mm of these are strain strengthened resulting in a strain weakened HAZ width of 12 mm. Al BM hardness is measured to be 74.04 HV and Cu BM is measured to be 107.9 HV.

2.2.2 Tensile test

Two initial tensile tests were conducted. One resulted in a fracture deep in Al HAZ shown in Figure 11. This weld is ”reinforced” by adding FM to create what is shown, a thick SZ. This is probably the reason the fracture occurs outside of the SZ even though the hardness test in Figure 10 would indicate a fracture in the middle of the SZ; 3.5 mm from the interface into Al. The orange circle shows a crack that had started to evolve. The tensile strength for this specimen was 183 MPa. The interface bond strength outperformed the strength of the weakest point in HAZ, and the Al BM tensile strength as the fracture occurred outside of HAZ.

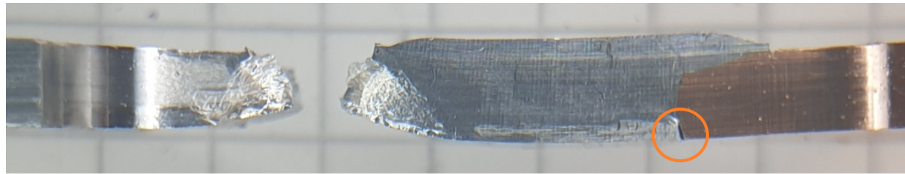

Figure 11: HYB tensile test 1.

Source: [13]

The other tensile test fractured close to the interface. Al covered the fracture with a small layer shown in Figure 12. The root error shown in Figure 11 is where the fracture started in the second test, resulting in the interface fracture. The second tensile test didn't have a "reinforced" SZ like the first. The tensile strength for this specimen was 134 MPa. As the fracture occurred at or close to the interface, the cause was the root defect and not the HAZ.

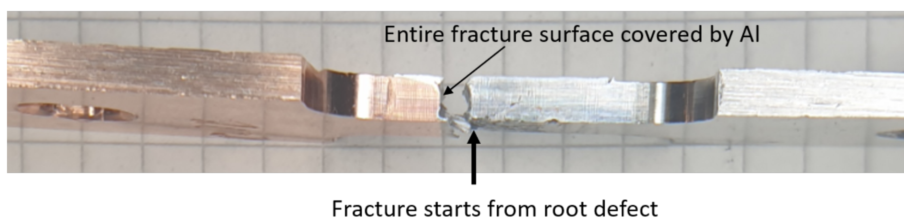

Figure 12: HYB tensile test 2.

Source: [13]

2.2.3 Bending test

Bending tests from both the top and bottom resulted in failure at different positions. Both of these samples are "reinforced". Bending from the top downwards created a fracture in the Al BM demonstrating a strong weld bond shown in Figure 13a. However, when bending from the bottom upwards, the fracture occurred in the interface shown in Figure 13b; the same root effect as the other two tensile tests is observed at the same position. That root error is what caused the fracture.

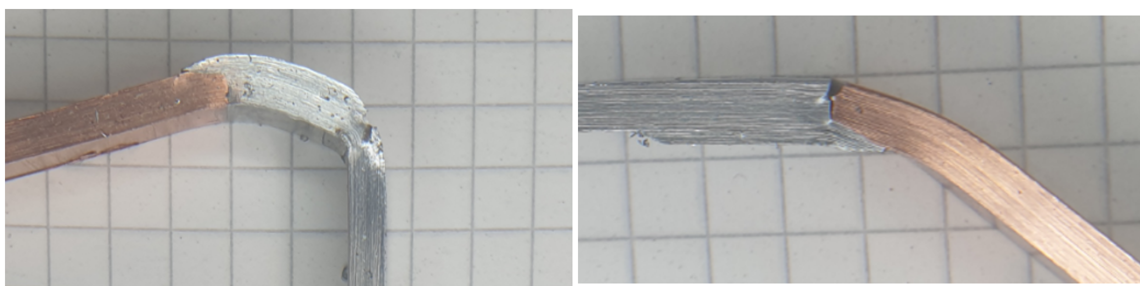

(a) Bending from top down.

(b) Bending from bottom up.

Figure 13: HYB weld bending test.

Source: [13]

3 Conductivity and Structure in Intermetallic Compounds

3.1 Conductivity overview

A conductor allows for the flow of electrical current and has an inherent amount of resistivity (ρ). Resistivity is a measurement that describes the restriction of electrical current; it is not dependent on geometry. The resistivity of a conductor is constant at constant temperatures, and is largely correlated with temperature. The temperature is managed by its environment and the amount of current passing through the material. Lowering the temperature of the conductor will increase its ability to transfer electrical current, thereby lowering its resistivity.
Resistance like resistivity, also describes the restriction of electric current, but it's specific to the conductors geometry. The correlation between resistance and resistivity is dependent on the length and cross-section area. An electrical conductor works similarly to a water pipe. A larger diameter allows for the transfer of more water volume per second, and the length of the water pipe increases the drag, lowering the amount of volume per second. Like the water pipe, a large cross-section area for a conductor allows for an increase in electrons per second (electrical current). At the same time, the length lowers its ability to transfer current. Equation 4 demonstrates the relationship between resistance and resistivity[30].

$$R = \frac{\rho L}{A} \tag{4}$$

Running a current through a conductor generates heat. The heat generated into the part, depends on the material's heat capacity and weight. Cu has a heat capacity (c) of 385 J/kgK and Al has a heat capacity of 887 J/kgK. The variable C in equation 5 is the heat capacity times mass of the conductor. Cu increases more in temperature at the same weight compared to Al. However, Cu is also more dense.

$$\Delta T = \frac{E}{C} \tag{5}$$

The relationship is described by equation 6 with α being the temperature coefficient of resistance[31]. Al and Cu has similar temperature coefficients of resistance with Cu having 0.00404 $K^{-}1$[32] and Al having 0.00393 $K^{-}1$[33]. This implies a similar increase in resistance per temperature when they are constructed to have the same resistance.

$$R = R_0(1 - \alpha(T - T_0)) \tag{6}$$

Power (P) is generally defined as energy (E) over time (t). It can be produced by the current (I) times the electric potential difference (V). Power is also defined as heat (Q) over time (s), known as joule heating. These sets of equations can calculate the heat generated in a resistor and the corresponding increase in resistance; script in Appendix B.

$$V = IR,\ P = IV,\ P = I^2 R,\ \frac{E}{t} = I^2 R$$

(7)

3.1.1 Type of circuit

A circuit uses various elements to control the flow, such as resistors, capacitors, and inductors. A complicated circuit uses many of these parameters in many different combinations and is often referred to as networks. The way current passes through a circuit is either by a series or parallel

configuration. Combinations of both series and parallel are also used. A series circuit has all the parameters aligned in a chain, leaving the current only one path. A parallel circuit has more than one path for the current[34]. Figure 14 shows two circuits with energy source and resistors. The top shows a circuit in series, while the bottom shows a parallel circuit.

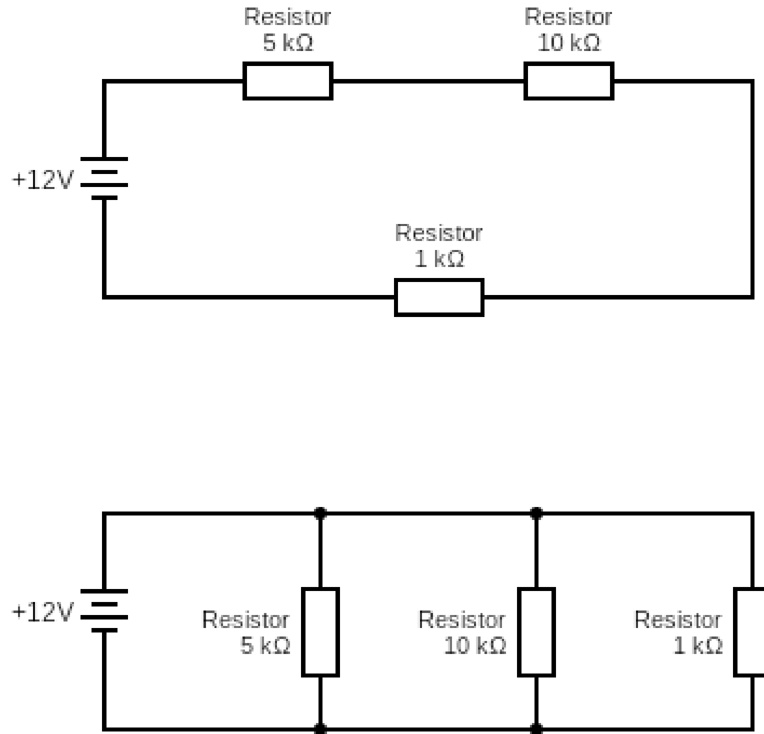

Figure 14: Series and parallel circuit.

Source: This work

When a current passes through a circuit, a voltage drop occurs. A voltage drop is a decrease in electrical potential along the path of the current. The total voltage drop in a series is the individual voltage drops added together. A parallel circuit has a constant voltage drop in each component which means the current varies in each one. In this case, the total resistance for series is shown in equation 8.

$$\begin{gathered} R_t = R_1 + R_2 + R_3 + ..., \\ R_t = 5k + 10k + 1k = 16k \end{gathered} \tag{8}$$

The voltage drop is constant across each resistor in parallel configurations. The total resistance is described in equation 9.

$$\begin{gathered} R_t = \frac{1}{\frac{1}{R_1} + \frac{1}{R_2} + \frac{1}{R_3}}, \\ R_t = \frac{1}{\frac{1}{5k} + \frac{1}{10k} + \frac{1}{1k}} = 0.769k \end{gathered} \tag{9}$$

The same three resistors create vastly different resistance depending on their configuration. A busbar is a part of an electrical circuit and acts as a conductor. The purpose of a conductor is to allow as much electrical current with as little resistance as possible. Bimetallic busbars have one metal acting as one resistor and another acting as another resistor. These are made operating both in parallel and series[35, 36, 21].

3.2 Intermetallic compounds

IMC is one of the three general classes of elementary constituents of alloys. The other two classes are pure metals or metalloids and solid solutions[37]. IMC is defined as a metal alloy that is created by two or more metallic elements. They are divided into two categories, stoichiometric and nonstoichiometric IMCs. Stoichiometric IMCs follows the law of definite proportions in the chemical reaction and can therefore be described by chemical equilibrium using natural numbers. Nonstoichiometric IMCs, however, cannot be described by natural numbers and violate the law of definite proportions[38]. The difference is essentially their ability to be described by a ratio of natural numbers. The intermetallic metal alloys often inhibit brittle properties and are generally hard. A general problem in IMCs is constitutional defects[39].

3.3 Al - Cu intermetallic compounds

Al - Cu welding is problematic due to the metals being incompatible from the welding point of view. IMCs are created because of their high affinity at temperatures above 120 °C. Chemical or interdiffusion occurs at this temperature and above. IMCs are more brittle and lower strength compared to both Al and Cu. An Al - Cu IMC joint will therefore either fracture in a weakened HAZ zone or on the IMC layer[40, 41]. However, a metallurgically bonded Al - Cu joint requires a certain thickness of the IMC layer to create a sound bond. Excessive amounts of IMC will, in turn, degrade the soundness of the joint. Braunović and Alexandrov states that mechanical properties radically decline once IMC thickness passes 2 μm[40]. This is substantiated and illustrated in Figure 15 done by Abbasi et al. in 2001[42].

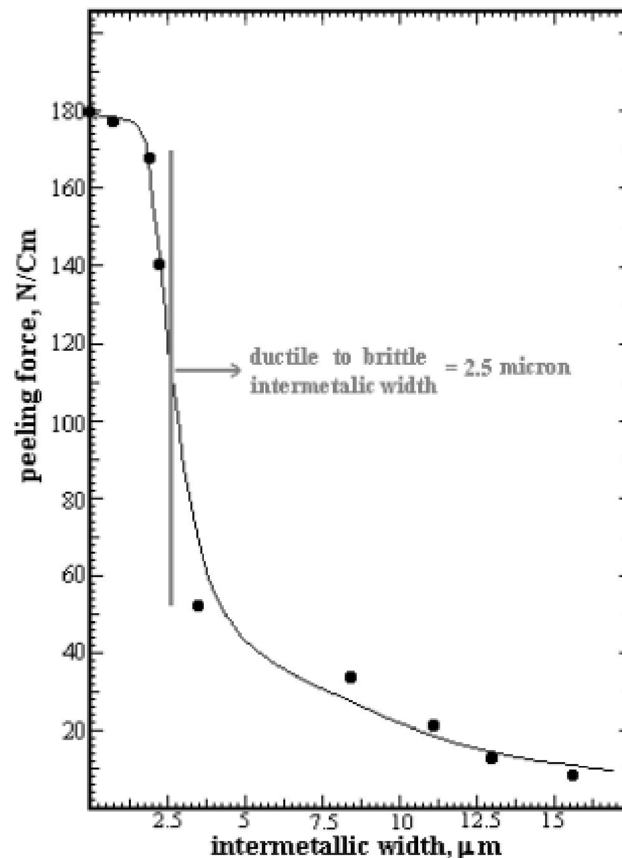

Figure 15: Cold roll weld, peeling force to IMC width graph.[42]

Source: [42]

3.4 Intermetallic phases

The interdiffusion process creates intermetallic phases. Al and Cu bond in different ways depending on temperature and time. Figure 16 shows the Al - Cu phase diagram representing what phases are possible at different temperatures. The phase diagram between Al and Cu has been widely studied, and iterations have been done since Murray made a major assessment of the system in 1985[43].

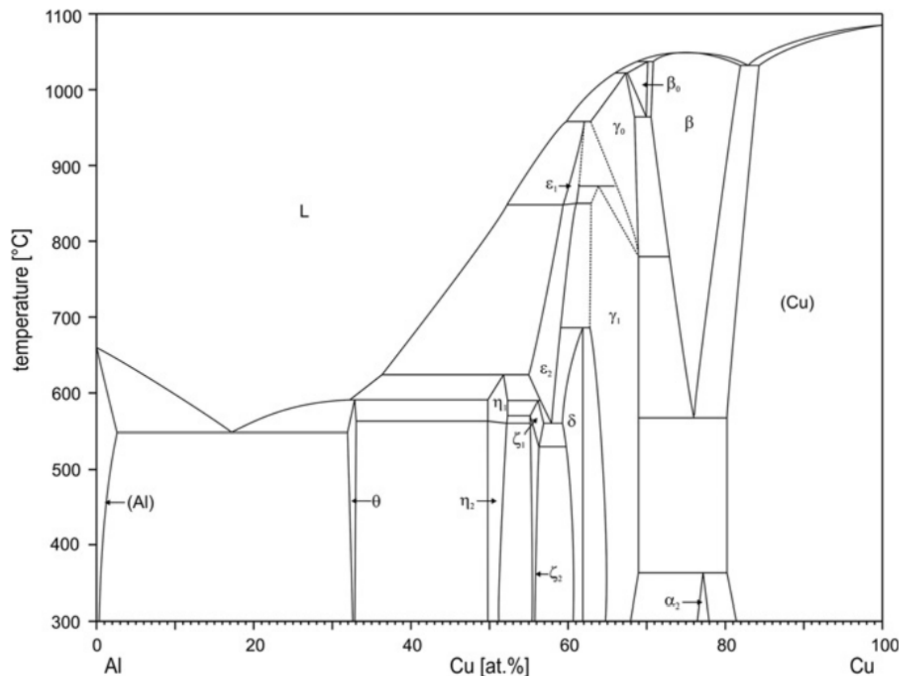

Figure 16: Al - Cu phase diagram.

Source: [44]

The temperature achieved during HYB welding is around 400 °C to 500°C. Therefore, the IMC structures that can occur during the HYB process, are $Al_2Cu(\theta)$, $AlCu(\eta)$, $Al_3Cu_{4-\delta}$ (ζ_2), Al_4Cu_9(rhombic)(δ) and $Al_4Cu_9(\gamma_1)$. The different structures are categorized with regard to their symmetry, geometry and composition range in table 4.

Different weld studies can confirm that the different structures found in the IMC region at various temperatures, conforms with the Al - Cu phase diagram. F. A. Calvo et al. studied the characteristics of the IMC formation in diffusion welding Al - Cu. The IMCs found in the weld interface were Al_2Cu, AlCu and Al_4Cu_9[48]. Interdiffusion can take place even after welding; if temperatures are elevated. Higher temperatures accelerate the rate of interdiffusion. The relationship between the thickness of the IMC structures and the time is parabolic and described in section 5.5. Each phase has a different rate of diffusion, shown in Figure 42. Multiple plots are measured, and since the growth is parabolic, the time has to be square rooted to create the linear regression.

Structure	%Cu	PS	SG	Lattice parameters	Reference
Al_2Cu	31.9-33.0	$tI12$	$I4/mcm$	$a = b = 5.949$ Å $c = 4.821$ Å $\alpha = \beta = \gamma = 90°$	[45]
AlCu	49.8-52.3	$mC20$	$C2/m$	$a = 11.973$ Å $b = 4.061$ Å $c = 6.807$ Å $\alpha = \gamma = 90°$ $\beta = 124.882°$	[45]
$Al_3Cu_{4-\delta}$	55.2-56.3	$oI24 - 3.5$	$Imm2$	$a = 4.0972$ Å $b = 7.0313$ Å $c = 9.9793$ Å $\alpha = \beta = \gamma = 90°$	[44]
Al_4Cu_9 (r)	59.3-61.9	$hR52$	$R3m$	$a = b = c = 8.7066$ Å $\alpha = 89.74°$ $\beta = \gamma = 90°$	[46]
Al_4Cu_9	52.5-59	$cP52$	$P - 43m$	$a = b = c = 8.7068$ Å $\alpha = \beta = \gamma = 90°$	[47]

Table 4: The achievable phases using the HYB method with composition properties, Pearson Symbol (PS), Space Group (SG), and Lattice Parameters

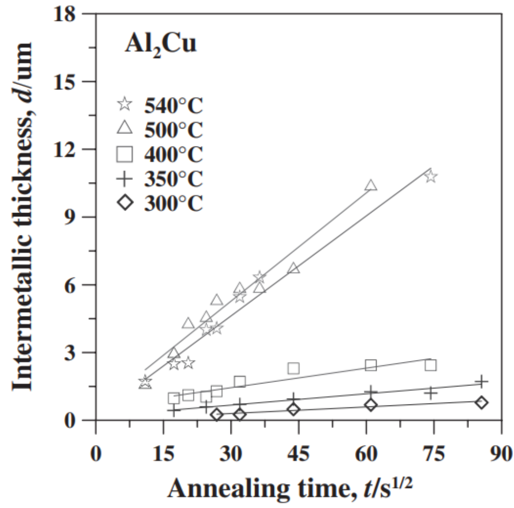

(a) θ.

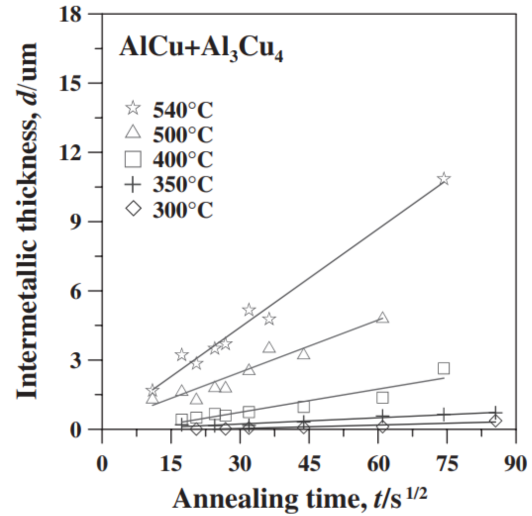

(b) η and ζ_2 phase diffusion coefficient.

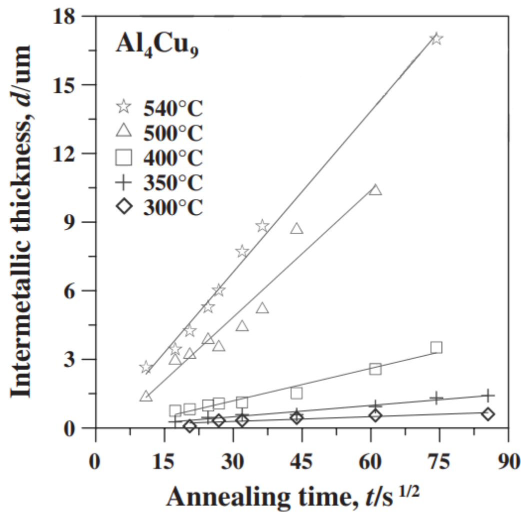

(c) δ phase .

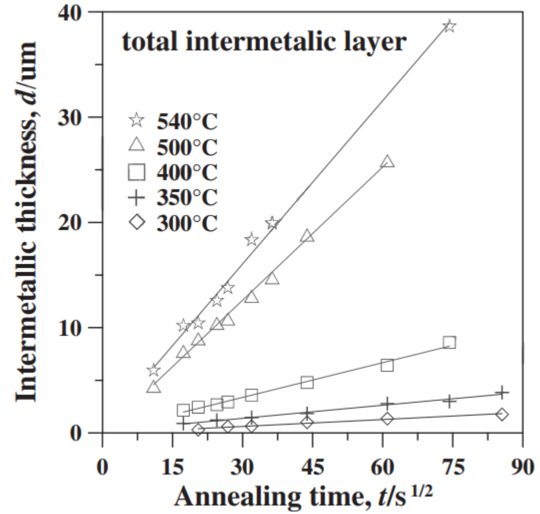

(d) Diffusion Cu high temperature.

Figure 17: Phase and total interdiffusion coefficient.

Source: [49]

The IMC phases sort into layers with Figure 18 as an example of how the IMC phases could be layered[7, 50, 51]. These layers are visibly distinct from one another when observing in the microscope after etching. SEM and TEM images are also able to discern the layers.

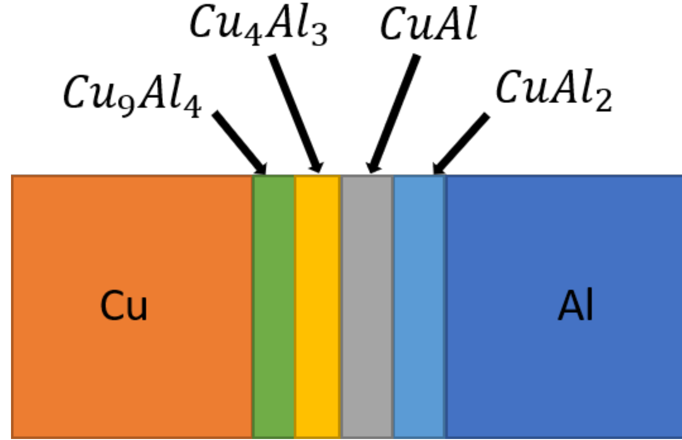

Figure 18: Schematic illustration of possible IMC layers.

Source: This work.

3.5 Intermetallic conductivity

The nature of the IMCs creates increased resistivity in the joint. Moiseenko et al. got a resistivity of 0.0776 $\Omega mm^2/m$ for the bulk IMC resistance[52]. That is 2.8 times the resistivity of Al and 4.51 times that of Cu looking at the general numbers from table 1. Research on phases has been able to identify the specific resistivity of each phase. These vary somewhat demonstrated in table 5.

Property	AlCu	Al_2Cu	Al_4Cu_9	Reference
Resistivity ($\Omega mm^2/m$)	$0.0744 \pm 6.7\%$	$0.0649 \pm 6.7\%$	$0.188 \pm 6.7\%$	[53]
	0.114	0.08	0.142	[54]
	-	0.076	0.17 - 0.26	[55]
Temperature coefficient (10^{-3}/K)	$3.31 \pm 4.2\%$	$3.45 \pm 2\%$	$1.64 \pm 6.1\%$	[53]
	-	3.6	3.85	[55]

Table 5: IMC phase resistivity and temperature coefficeint of resistance.

Some Al - Cu joints are welded so that Al BM carries current in parallel with Cu BM. In other joints like HYB and FSW, the BMs carry the current in series. This changes how the resistivities of the phases affect the total resistance. Each phase acts as a small conductor, and its resistance can be calculated by using equation 4. In the case of HYB and other similar solid welding techniques, θ, η, ζ_2, and δ are the phases possible in the interface. IMC phases have been observed to be separated into layers. This makes it possible to estimate a total IMC layer resistance by the different phases resistivities, through simple parallel and series theory described in section 3.1.1. Figure 21 demonstrates a busbar where Al - Cu IMC and BMs are in parallel. The volume fraction of each phase plus its resistivity is needed, as shown in equation 10. The equation includes all possible phases for HYB.

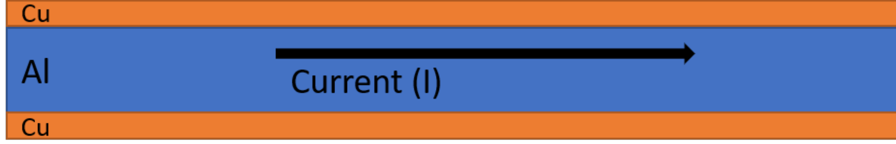

Figure 19: IMC in parallel.

Source: This work.

$$\frac{1}{\rho_{IMC}} = \frac{\nu_\theta}{\rho_\theta} + \frac{\nu_\eta}{\rho_\eta} + \frac{\nu_\zeta}{\rho_\zeta} + \frac{\nu_\delta}{\rho_\delta} \tag{10}$$

Abbasi et al. bonded a busbar by cold rolling, then annealing the busbar for up to 1000 hours at 250°C. The busbar is a conductor where the Al and Cu carry the current in parallel, like what is demonstrated in Figure 21 with Cu on both sides. Peeling force, electrical conductivity, and IMC thickness was measured at different annealing times. Figure 20 demonstrates both IMC growth over time and the IMC resistivity correlation. The Al plate was 13 mm before rolling and 3.48 mm after. The Cu was 1 mm before and 0.36 mm after. Resulting in a total reduction of 72 %.

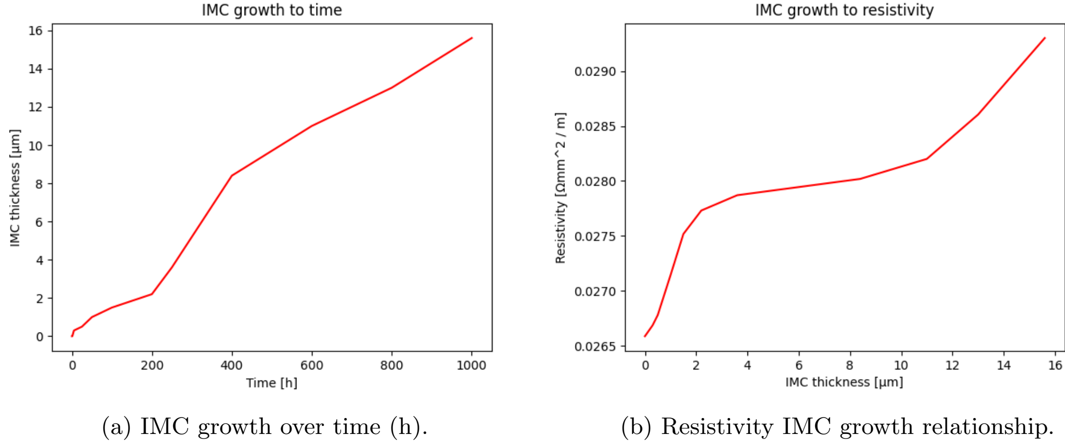

(a) IMC growth over time (h). (b) Resistivity IMC growth relationship.

Figure 20: IMC growth and resistivity at 250°C.

Source: [42]

No IMC is detected directly after cold rolling or after one-hour annealing. Measurements before annealing and after one hour gave 0.02659 $\Omega mm^2/m$. This created a reference resistivity. The reference resistivity is higher than what their resistivity should have been according to their calculation. The report attributes the reduction in conductivity to a hidden bond resistance. Some disconnect in IMC resistance theory is observed as the resistivity almost plateaus from 2 to 9 μm seen in Figure 20b. However, looking at the range 0 - 2 μm, a sharp increase in resistivity is observed.

It is impossible to calculate the increase in resistivity seen in Figure 20a using the theoretical equation 9 for parallel conductivity. The resistance should not be that high based on the theoretical formula. It is caused by the IMC being in between the BMs, but the exact mechanisms are unknown.

HYB has its BMs acting in series and therefore the IMCs acts in series. One way of solving the resistance for IMCs is to measure how thick (d) each layer of IMC phases is and what resistivity each phase has. In the case of HYB, θ, η, ζ_2 and δ are the phases possible in the interface. Figure 18 illustrates a possible layering of the IMC phases. Assuming each layer has the same interface

surface area like Figure 18, equation 11 solves resistance for HYB IMC phases.

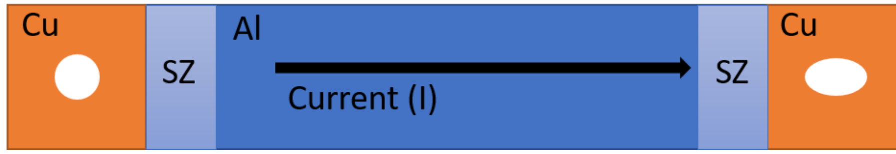

Figure 21: IMC in series.

Source: This work.

$$R_f = \frac{\rho_\theta \cdot d_\theta + \rho_\eta \cdot d_\eta + \rho_\zeta \cdot d_\zeta + \rho_\delta \cdot d_\delta}{A} \tag{11}$$

4 Conductivity test

4.1 Test method

The conductivity tests measure the resistance of HYB samples. The joint has a resistance in both BMs and also the interface. The interface has a resistance due to the nature of the IMCs, but weld defects are also a source of resistance. Two commonly used methods for resistance measuring are two-terminal sensing and four-terminal sensing.

Figure 23 represents the two-terminal sensing method. A constant current is applied, and the key problem regarding the two-terminal approach for low resistance measurements is that the total lead resistance is included in the measurements. The voltage determined by the voltmeter, would not be the same as the voltage coming directly across the test resistance, since the test current induces a slight but noticeable voltage decrease across the lead resistances. Since typical lead resistances vary from 10 mΩ to 1 Ω, reliable two-terminal sensing measurements are difficult to achieve when resistance is less than 100 Ω. Lead resistance is the largest source of error in this method. Using test leads with a combined resistance of 50 mΩ when measuring a 500 mΩ resistor, for example, would result in a 10 % measurement error not accounting for the instrument's error. A test method which largely nullifies the lead resistance error is called the four-terminal sensing method.

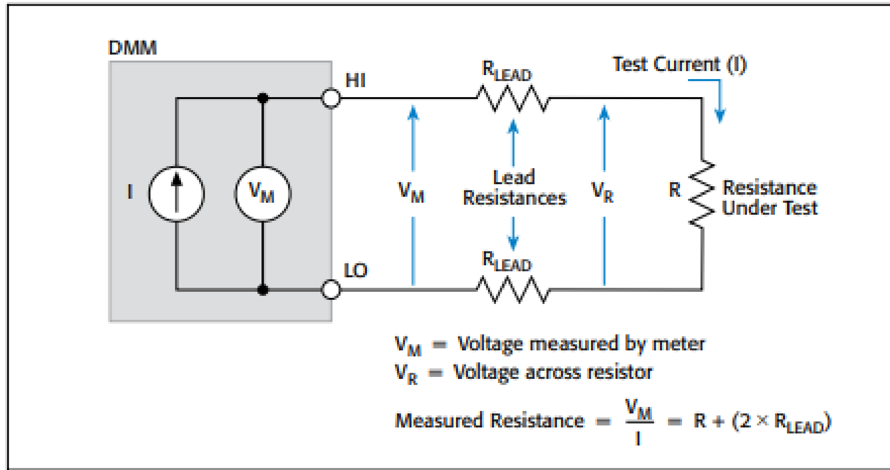

Figure 22: Four-terminal sensing schematic drawing.

Source: [56]

For low resistance tests, a different technique is used to reduce the impact of test lead resistance. One may use the four-terminal sensing method shown in Figure 22, to measure conductors with a resistance equal to or lower than 1 kΩ. Voltage drop in the test leads is avoided since the voltage is calculated on the Conductor Under Test (CUT). Thus, nullifying a significant source of error. The test current is pushed through the test resistance through one set of test leads. The voltage across the CUT is measured through a second set of test leads in this configuration. These are what are called sense leads. Although the sense leads can carry a small current, it is usually negligible and can be ignored for most purposes. As a result, the voltage determined by the voltmeter is almost identical to the voltage across the CUT. Compared to the two-terminal sensing, the resistance can be measured much more precisely. The current that passes through the sense leads is in the pico amps scale[56].

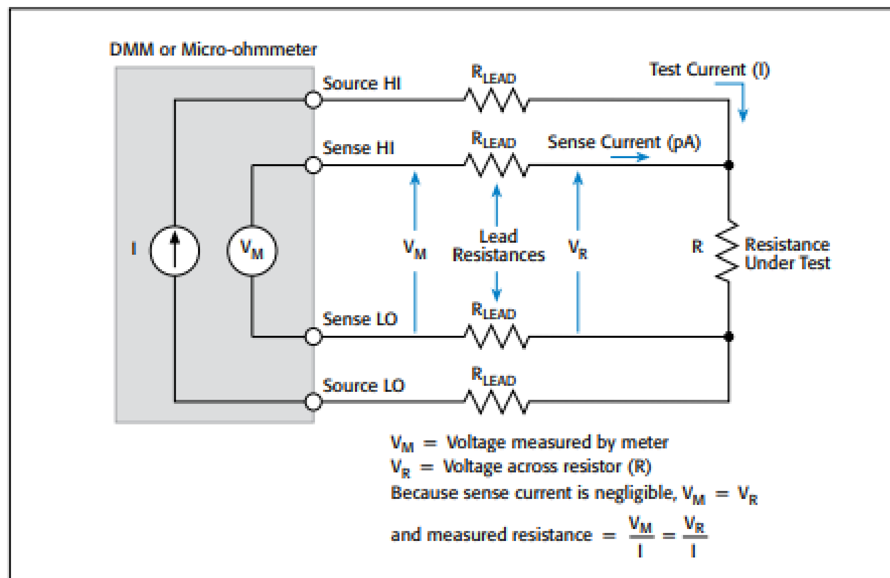

Figure 23: Two-terminal sensing schematic drawing.

Source: [56]

4.2 Setup

Electrical characterization of the HYB weld is important for how to dimension it for practical applications and whether it performs well. A power supply and a multimeter were set up to conduct the four-terminal sensing technique for measuring voltage drop. The voltage drop will then give us the resistance because the power supply gives the current; look equation 8. Voltage drops across 2.2 mm are tiny, resulting in measuring microvolts. Therefore the high precision Fluke 8846A Digit Precision Multimeter was used to measure each voltage drop. The current passed through the test piece came from a PeakTech 6135, Switching Mode Power Supply. Using the numbers from table 1, Figure 24 demonstrates how voltage drops along with each measuring point when the test piece is subjected to 2 amperes (A) with a cross-sectional area of 6 mm^2. The interface is placed exactly in the middle between measure points 6 and 7. Meaning the Cu ends at 14.2 mm and Al begins at 14.2 mm. With these parameters in mind, Figure 24 shows no voltage drop caused by the IMC; hence, no IMC resistance is present. The deduction is made by observing the line being continuous at the interface.

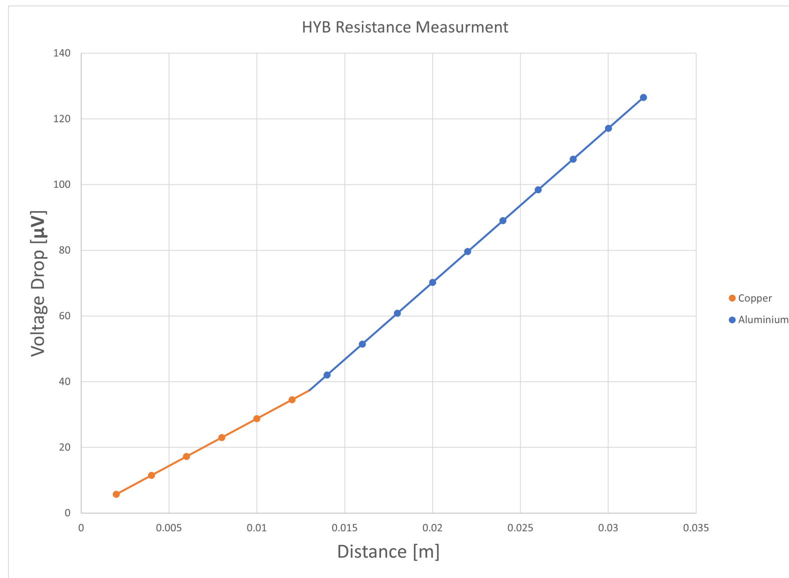

Figure 24: Voltage drop plot no IMC resistance.

Source: This work.

Assuming the same geometry and position of the interface, Figure 25 shows a disconnect of the voltage drop at the interface. This demonstrates a resistance caused by the Al - Cu bond. Weld defects can create resistance in the bond interface, and the Al - Cu IMC phases are known to have an increased amount of resistance compared to Al and Cu BMs. Figure 25 shows how a bond can create a 5 μV additional voltage drop compared to the BM. Total IMC resistivity can then be calculated by measuring its surface area and length.

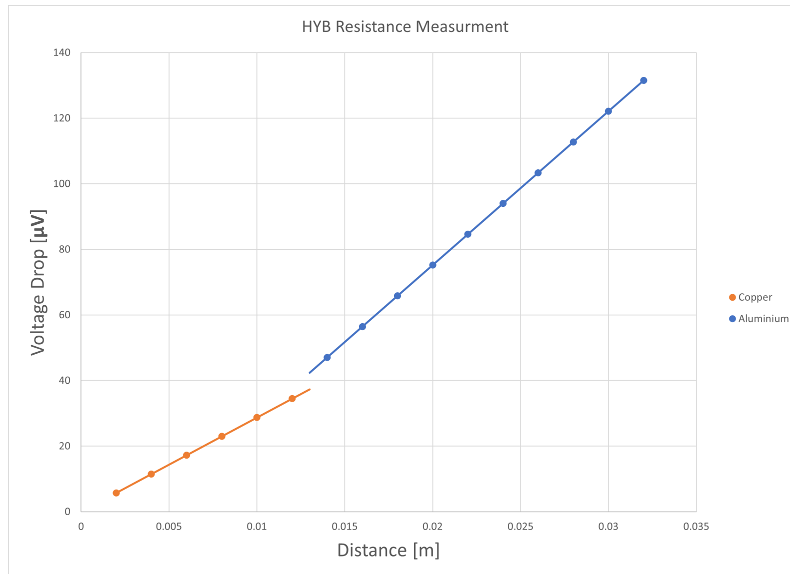

Figure 25: Voltage drop plot 5 IMC voltage drop.

Source: This work.

Test pieces are cut out from the HYB weld. These pieces are 55 mm long and 2 mm thick. A test jig was 3d printed to be able to measure at the same positions consistently. Many iterations of the jig were created, and the final one is shown in Figure 26. The red component has wires connected to the samples, which are where the current is applied. The yellow component is the lid which has the wires measuring voltage drop; the sense leads.

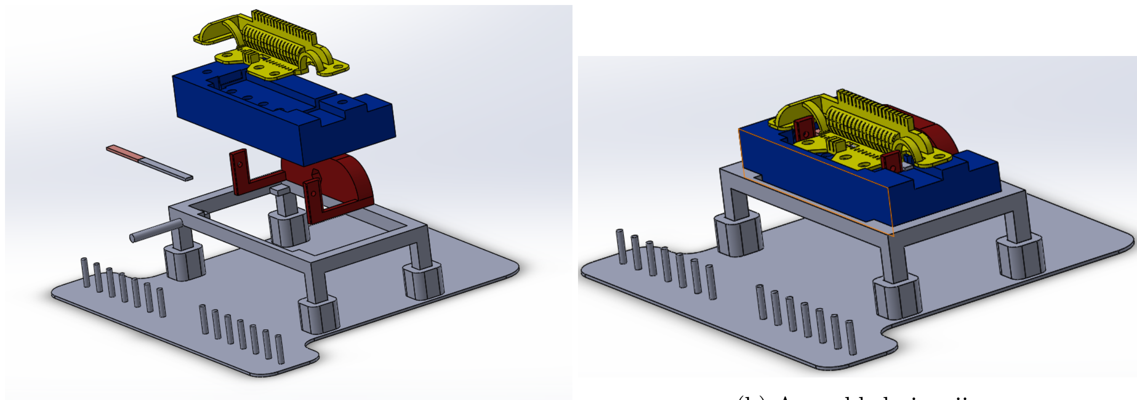

(a) Exploded view of jig.

(b) Assembled view jig.

Figure 26: IMC growth and resistivity at 250°C.

Source: This work

Figure 27a shows the bottom of the jig lid that is in contact with the specimen. Voltage drop is measured over 17 wires, resulting in 16 measurements. The orange circle shows the hole where the Cu - Al interface is. The interface is between the seventh and eighth wire. The hole is placed so that the distance from the interface to the wire can be measured; the picture is shown in Figure 27b. The holes drilled for connecting the busbars, shown in Figure 7, limited how long the Cu could be cut. The samples (CUTs) and jig were made to have the most amount of measuring points possible on the Cu BM. The wires stand 2.2 mm apart from one another. resulting in a total distance of 35.2 mm. The main testing was run on samples that were heated to 250°C, as it became apparent that it would be too difficult to measure resistance over the IMC layer at a lower

temperature. Testing on a piece heated at 200°C for 19 days gave no conclusive results for IMC resistivity.

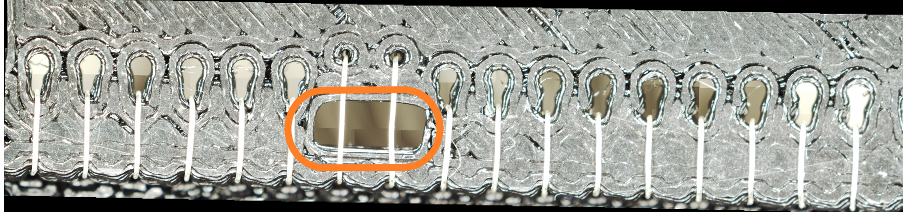

(a) Jig wires.

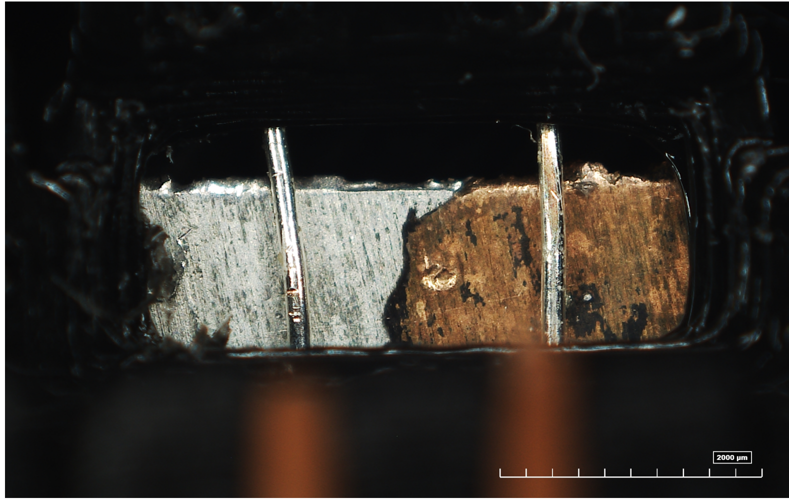

(b) Interface view in the jig.

Source: This work.

Figure 27: Jig wires and measuring hole for interface distance.

A digital microscope does the measurements conducted on the highlighted area in Figure 27a. There are in total four samples tested with conductivity called E0, E1, E2, and E3. The distance from the wires to the interface in each sample is shown in Appendix K. The values are shown in table 6.

Sample	Temperature ($°C$)	Holding time (h)	Length (mm)	Distance to interface from Cu	Distance from Al
E0	0	0	50	1.381	0.819
E1	250	242	50	1.011	1.189
E2	250	430	50	1.26	0.94
E3	250	731	50	1.08	1.12

Table 6: Electrical sample matrix.

4.3 Dimensions

The weld interface has a large contact area at around 1.6 times the cross-section of the sample due to the Al FM flowing on to the Cu BM while being pressured downwards by the weld shoulder. Figure 28 shows the weld interface with FM highlighted by etching.

Figure 28: Interface outlined.

Source: This work.

An increase in the weld contact area will decrease the resistance of the bond. This, makes the characterization of the interface resistance difficult. The excess filler on top of the weld also span more than 2.2 mm in length which makes the IMC resistance go over multiple measuring points. This is undesirable as the IMC resistance should only be between two wires. Testing without addressing this problem, did not produce usable data. The solution was to grind down the top of the weld to reduce the excess FM, reducing the weld contact area and therefore increasing the interface resistance. The height of the weld was originally constant 3 mm, and without special tools, the grinding had to be done manually. This created an uneven height throughout the samples. As for the thickness, it was cut with the Struers Accutom-50 cutter. The thickness also varied shown from control measurements. Table 7 shows the cross-section area (mm^2) at position (mm) for each sample.

Position(mm)	Sample E0 (mm^2)	Sample E1 (mm^2)	Sample E2 (mm^2)	Sample E3 (mm^2)
0	3.589	3.8316	4.1001	3.6091
12,5	3.96	3.7635	4.1625	3.7044
25	4.0804	3.7056	4.114	3.627
37,5	4.1209	3.6864	4.0796	3.667
50	4.0804	3.5144	4.0232	3.648
Average	3.96614	3.7003	4.09588	3.6511

Table 7: Electrical sample matrix.

The measurements conducted are voltage drops. A larger area will decrease the voltage drop from each measurement. The area affects the voltage drop one to one, as shown in equation 4. An example is sample E1 which has a higher area at position zero, so the voltage drop will be lower than the average. Therefore, the resistance should be adjusted to be higher. The way this is done is by dividing the measured area by the average area. This creates a ratio that makes up for the sample being uneven. Between each measuring point, a linear function from interpolation is made. That is a simplification as the surfaces might be more curved. The script in appendix H creates the linear functions in each interval as well as Figure 29 and 30.

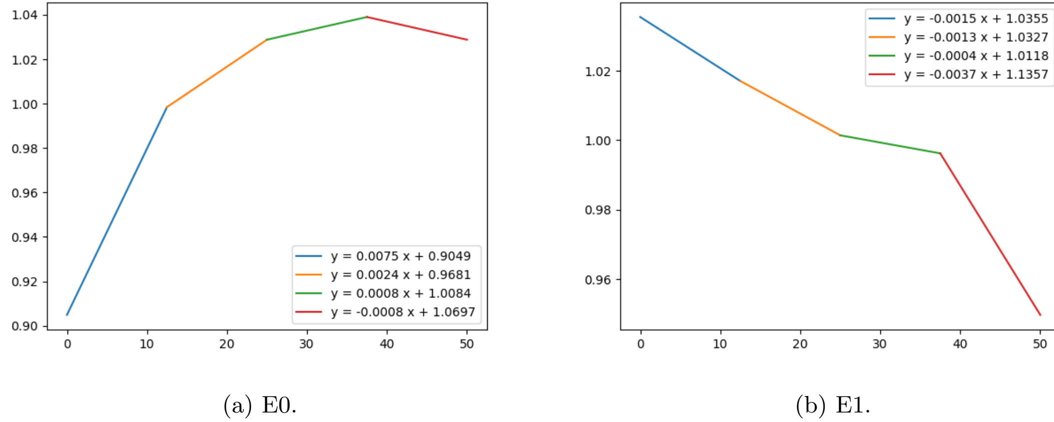

(a) E0. (b) E1.

Figure 29: E0 and E1 cross section area relationship with linear functions.

Source: This work.

E0 has around 10 % less area than average at the start and reaches around 4 % more at 37.5 mm. E1 has a range of around 4 % more and 5 % less than average. Figure 30 shows E2 having 1.5 % more and 1.5 % less than the average. E3 varies with 1.5 % more and 1 % less than the average. So E2 and E3 were very well ground down, while E0 and E1 were quite a bit worse.

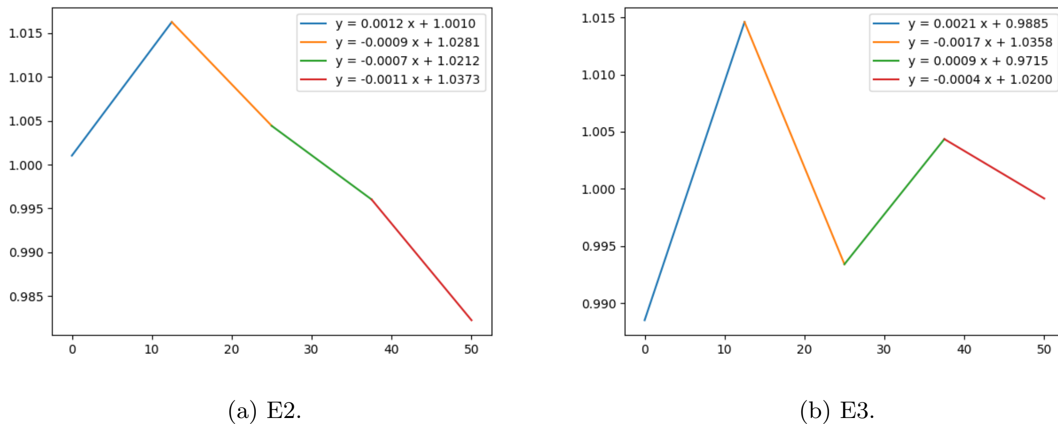

(a) E2. (b) E3.

Figure 30: E2 and E3 cross section area relationship with linear functions.

Source: This work.

These linear functions that approximate the cross-section ratio allow for calculating the average thickness at each point. A moving average cross-section relationship is created for each measuring point. Meaning, the relationship between the average cross-section area and the total average cross-section area for 0 - 2.2 mm, 0 - 4.4 mm, 0 - 6.6 mm, etc., up to 0 - 35.2 mm, is calculated and accounted for. Simply put, the measured voltage drop accounts only for the average cross-section area of the measured interval. The moving average is shown in Appendix N.

4.4 Electrical measurement results

The graphs are shown with resistance ($\mu\Omega$) on the y-axis and distance (mm) on the x-axis. 20 automatic measurements at a minimum were conducted at each measuring point. The average of

these measurements are what is shown on the graphs. They are also what the standard deviation is based upon. Figure 31 and 32 shows the resistance in sample E0. The standard deviation at each measurement was between a minimum of 26 and a maximum of 140 nano volts. The current reported by the power supply was 3.036 A. The 0 - 35.2 mm voltage drop at the start of testing was 647.5 μV, and at the end of testing, it was 646.0 μV. The reduction in volt was 0.23 %.

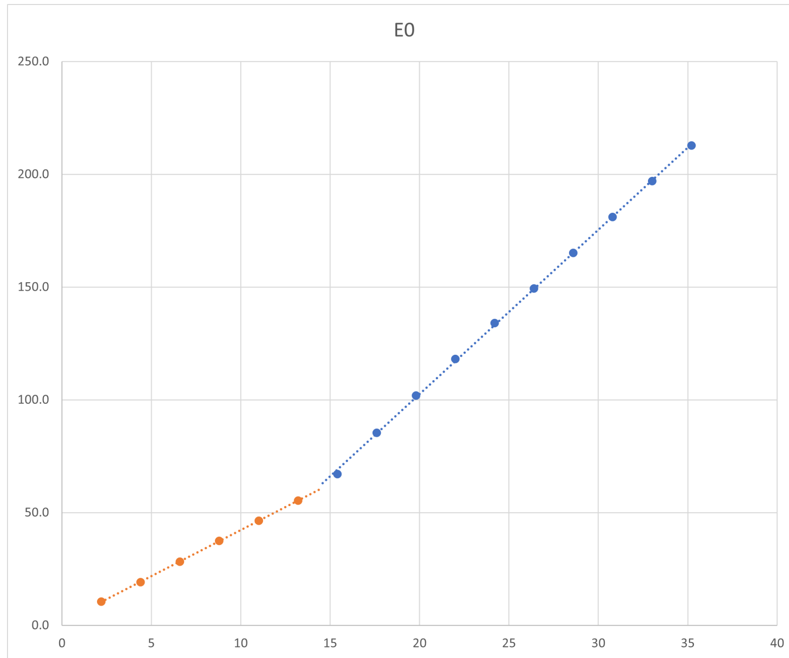

Figure 31: E0 graph.

Source: This work.

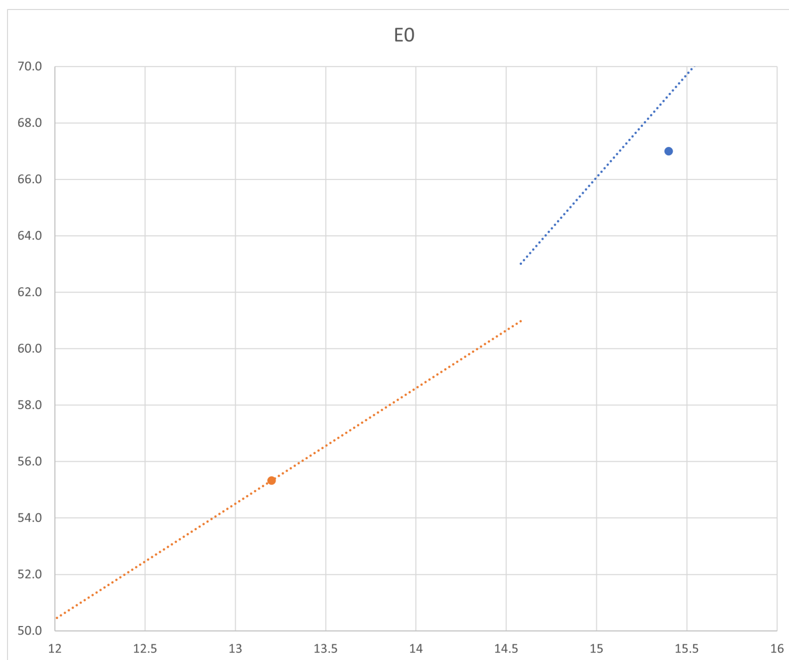

Figure 32: E0 graph zoomed.

Source: This work.

Figure 33 and 34 shows the resistance in sample E1. The standard deviation at each measurement

was between a minimum of 24 and a maximum of 167 nano volts. The current reported by the power supply was 3.036 A. The 0 - 35.2 mm voltage drop at the start of testing was 667.6 μV, and at the end of testing, it was 665.4 μV. The reduction in volt was 0.33 %.

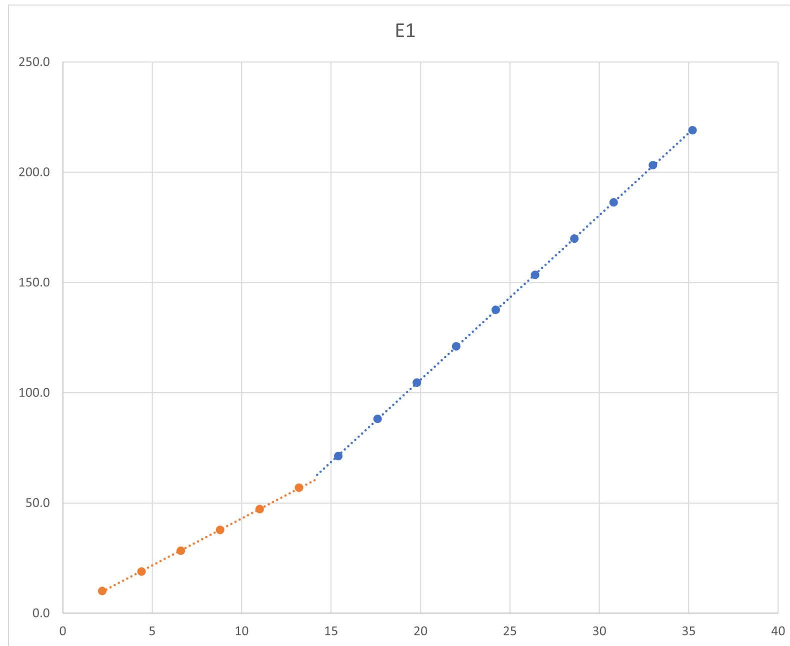

Figure 33: E1 graph.

Source: This work.

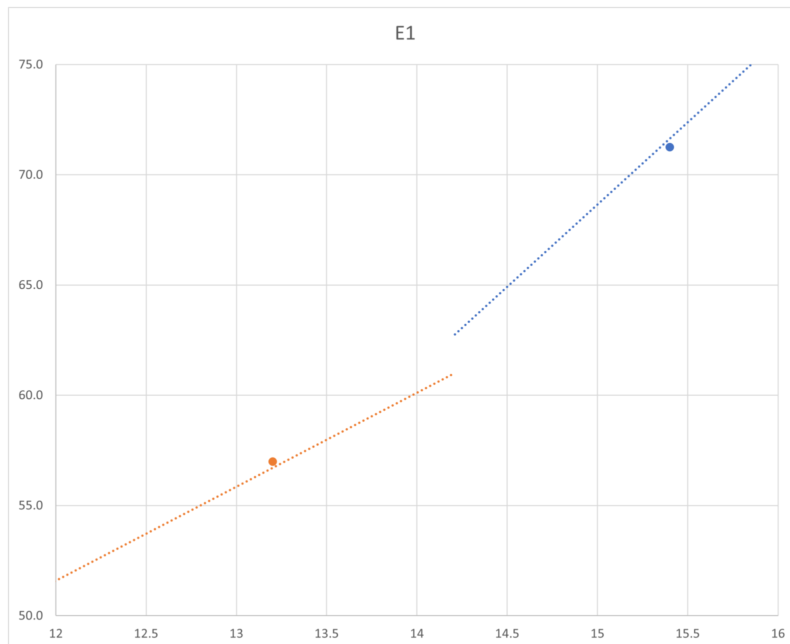

Figure 34: E1 graph zoomed.

Source: This work.

Figure 35 and 36 shows the resistance in sample E2. The standard deviation at each measurement was between a minimum of 17 and a maximum of 195 nano volts. The current reported by the power supply was 3.037 A. The 0 - 35.2 mm voltage drop at the start of testing was 594.2 μV, and

at the end of testing, it was 592.9 μV. The reduction in volt was 0.22 %.

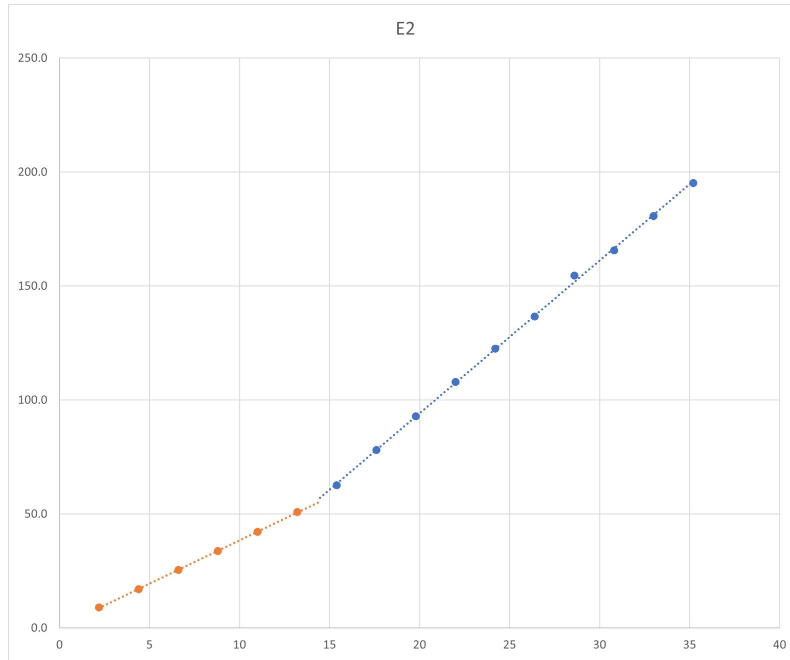

Figure 35: E2 graph.

Source: This work.

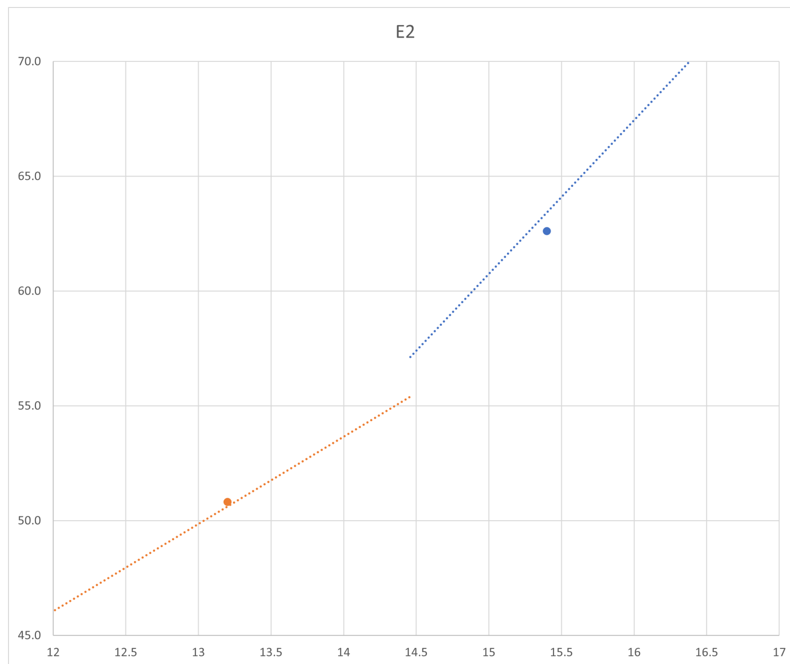

Figure 36: E2 graph zoomed.

Source: This work.

Figure 37 and 38 shows the resistance in sample E3. The standard deviation at each measurement was between a minimum of 22 and a maximum of 147 nano volts. The current reported by the power supply was 3.037 A. The 0 - 35.2 mm voltage drop at the start of testing was 670.4 μV, and at the end of testing, it was 669.7 μV. The reduction in volt was 0.10 %.

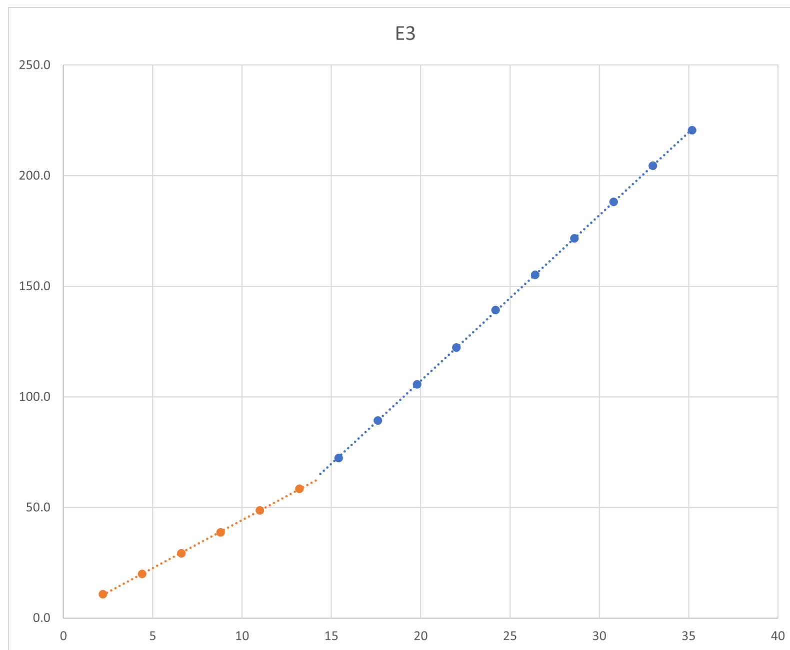

Figure 37: E3 graph.

Source: This work.

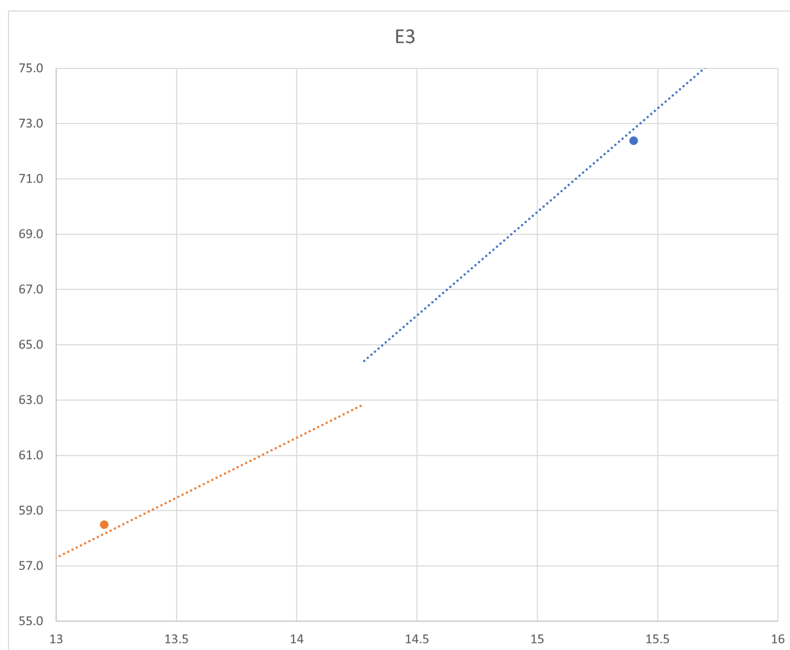

Figure 38: E3 graph zoomed.

Source: This work.

The standard deviation was really low compared to the measurements being in microvolts. The current was also quite stable throughout the testing according to the power supply. It shows no heating in the sample throughout the testing period. The IMC resistance are shown in table 8 as well as the Cu and Al %International Annealed Copper Standard (IACS). The %IACS is a standard way of demonstrating the conductance of a material relative to Cu. Cu has, therefore, an IACS of 100 % at room temperature. Figure 6a uses on the left side %IACS to demonstrate Al conductivity. Table 8 shows Cu with higher than 100 %IACS. This cannot be, and there is

something wrong with the measurements.

Sample	IMC resistance ($\mu\Omega$)	Cu %IACS (%)	Al %IACS (%)
E0	1.72	119.6	63.9
E1	2.03	104.0	62.0
E2	1.94	104.4	61.5
E3	1.80	108.5	64.1

Table 8: Electrical sample results.

5 IMC Growth Diffusion

Diffusion is a wide term used to describe the movement of everything. The term is used for the distribution of, among others, ideas, people, and matter. Atoms can move and bond with each other in solids. The mechanisms that cause this are vacancy- and interstitial diffusion. These mechanisms happen in both homogeneous metals and two different metal alloys. When this occurs in a homogeneous pure metal or alloy, it is called self-diffusion. All the atoms are of the same type and are able to exchange positions illustrated in Figure 39 [57].

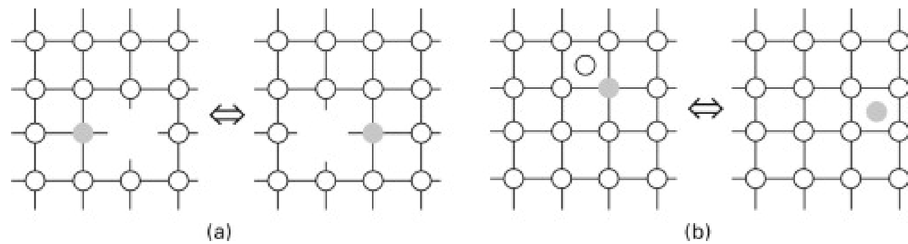

Figure 39: Self-diffusion schematic drawing.

Source: [58]

Interdiffusion, or chemical diffusion, is the diffusion between two metals. Atoms in the metals move due to a concentration gradient, and the movement is illustrated in Figure 40.

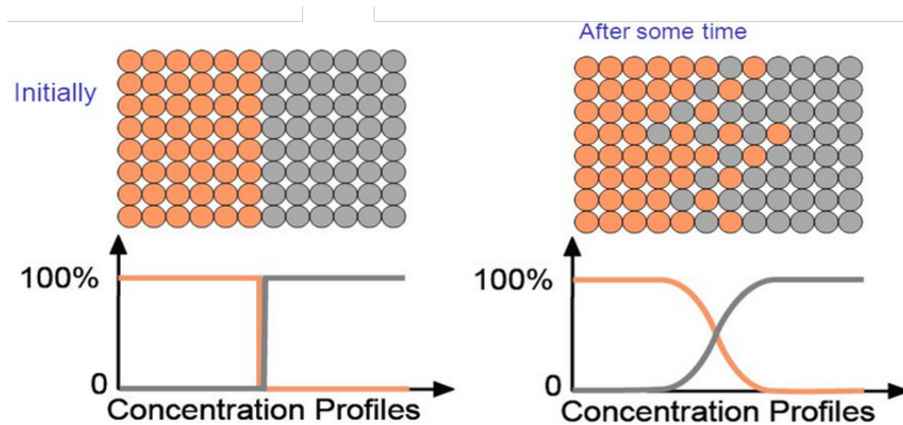

Figure 40: Interdiffusion schematic drawing.

Source: [59]

A Cu - Al welded joint bonds due to the vacancy and interstitial mechanisms. Atoms are arranged in crystal lattices. A lattice site is the position of an atom in its crystal lattice illustrated in Figure 41. Vacancies, meaning the lack of an atom, can be present within the crystal. An atom can jump

from its lattice site over to the vacancy. Enough energy for the atom to break its bond will enable the jump, and it is in the form of thermal energy. This is called vacancy diffusion. Its diffusion rate depends on the number of vacancies and the activation energy for the exchange[60].

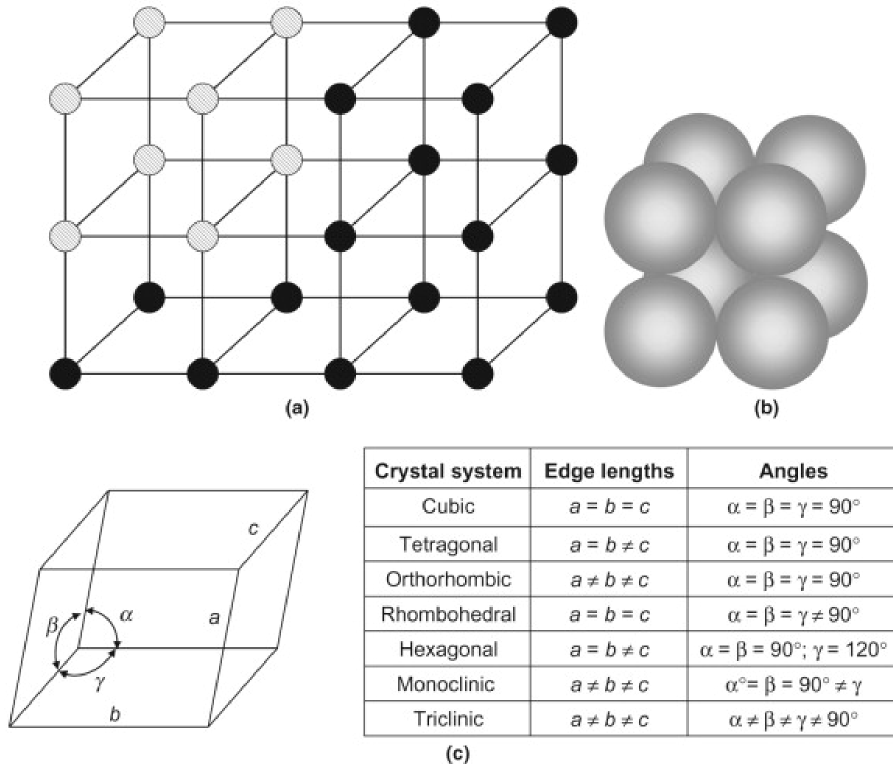

Crystal system	Edge lengths	Angles
Cubic	a = b = c	α = β = γ = 90°
Tetragonal	a = b ≠ c	α = β = γ = 90°
Orthorhombic	a ≠ b ≠ c	α = β = γ = 90°
Rhombohedral	a = b = c	α = β = γ ≠ 90°
Hexagonal	a = b ≠ c	α = β = 90°; γ = 120°
Monoclinic	a ≠ b ≠ c	α°= β = 90° ≠ γ
Triclinic	a ≠ b ≠ c	α ≠ β ≠ γ ≠ 90°

Figure 41: Crystal lattice illustration.

Source: [60]

Interstitial diffusion can only occur with two different types of atoms. One has to be smaller than the other. The smaller atom can diffuse between the bigger atoms without a need for a vacancy. This mechanism is faster than vacancy diffusion.

5.1 Fick's law

Fick's first and second law is one way to describe the diffusion process. Fick's first law predicts the rate of mass diffusing through an area. This is called flux. Fick's first law requires a constant concentration gradient which is called steady-state diffusion[61]. The gradient is only dependent on the position.

$$J = -D\frac{dc}{dx} \tag{12}$$

J = Flux $[mol/m^2s]$
D = Diffusion coefficient $[m^2s]$
c = Concentration gradient $[m^{-3}]$
x = Length in the direction of the flux $[m]$

The change in x will always be positive, but the change in concentration gradient will always be negative. This is due to the concentration being larger at the beginning thus having $c_1 > c_2$ making $dc = c_2 - c_1$ negative. That is the reason the negative sign is before the diffusion coefficient. The diffusion coefficient describes how fast the diffusion happens. There is no universal diffusion coefficient for metal; it depends on what metal it is diffusing into. Hence, Al will diffuse into Cu at

a different rate than it will diffuse into Fe. The diffusion coefficient formula is shown in equation 13.

5.2 Diffusion coefficient

$$D = D_0 e^{-\frac{Q_d}{RT}} \tag{13}$$

D_0 = Pre-exponential diffusion coefficient $[m^2/s]$
Q_d = Activation energy $[J/mol]$
R = Gas constant $[J/mol - K]$
T = Temperature $[K]$

The activation energy in diffusion is the minimum amount of energy required to press the atoms past one another. Like the rate of diffusion, the activation energy depends on whether it's interstitial or vacancy diffusion. Pushing an interstitial atom through the surrounding atoms normally requires less energy, meaning interstitial diffusion requires lower activation energy than vacancy diffusion[62]. The pre-exponential diffusion coefficient is a constant that is experimentally produced. Looking at the function with no context, an infinitely large temperature would make the diffusion coefficient equal to the pre-exponential coefficient. How the diffusion coefficient is illustrated is with a logarithmic y- and x-axis. The y-axis is the natural logarithm of the diffusion coefficient (lnD), while the x-axis is often a thousand divided by the temperature in Kelvin (1000/Temperature[K]). This way, the lnD is a linear graph. Mao et al. (2020) measured the diffusion coefficient in Cu to Al near Al - melting temperature[63]. Al is at a semi-solid-state at this temperature. The diffusion coefficients are shown in the table 9.

Temperature (K)	800	850	900	950
$D_{Cu}(10^-11m^2/s)$	2.12	10.04	23.34	48.33
$D_{Al}(10^-11m^2/s)$	131.4	157.85	177.7	207.55

Table 9: Diffusion coefficients at different temperatures[63].

These are plotted in a logarithmic graph shown in Figure 42.

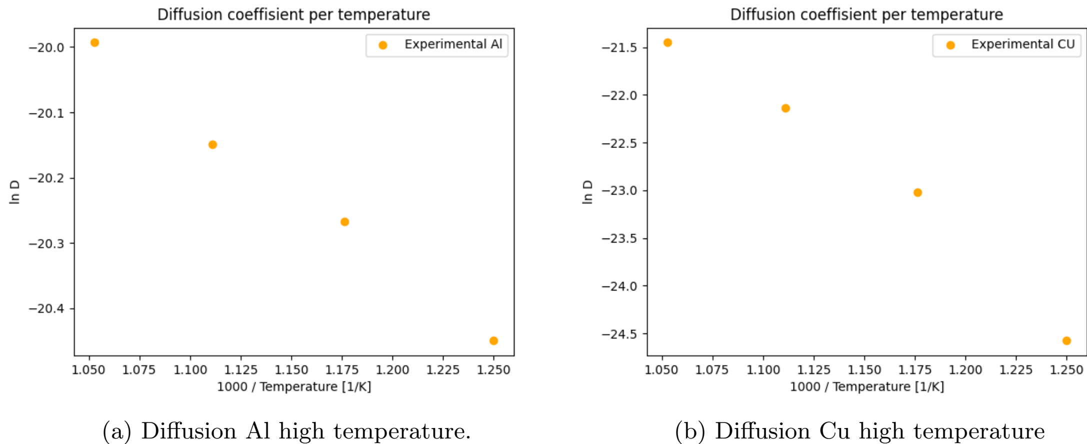

(a) Diffusion Al high temperature.

(b) Diffusion Cu high temperature

Figure 42: Al and Cu diffusion high temperature.

Source: [63]

Using the machine learning tool scikit-learn, we get a model for retrieving the graph for ln D [64]. The model is in Appendix D. The graph is shown in Figure 43

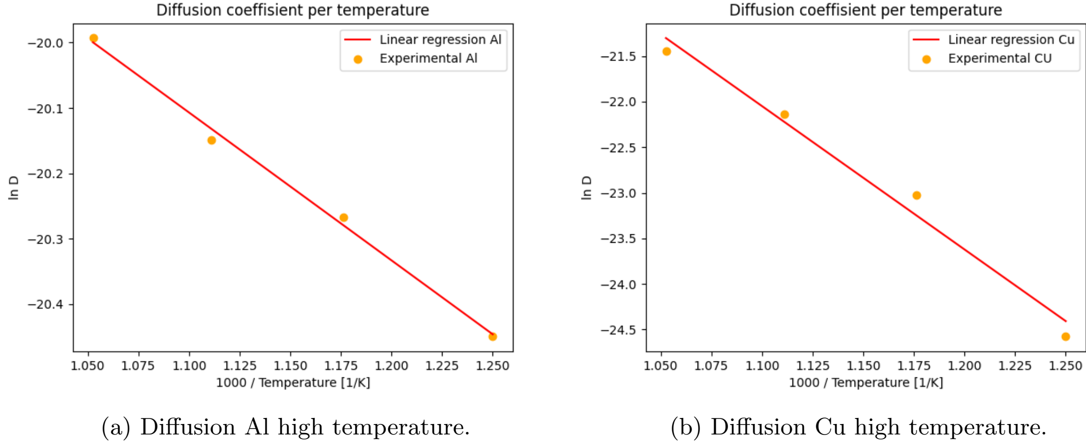

(a) Diffusion Al high temperature. (b) Diffusion Cu high temperature.

Figure 43: Al and Cu diffusion high temperature with regression line.

Source: This work and [63]

The model in Appendix D also retrieves the function of the lnD graph and calculates the activation energy (Q_d) and the pre-exponential diffusion coefficient (D_0). The only needed input variables are the diffusion coefficients per temperature. For Al, the linear function looks like; $lnD = a(1000/T) + b = -2.265(1000/T) - 17.615$. When comparing this to equation 13, the only unknown is the activation energy. The diffusion coefficient is equal to the e raised to the bth power; $D_0 = e^b$. In this case; $D_0 = 2.238 \cdot 10^{-08} m^2/s$.
The activation energy is derived by; $a(1000/T) = -Q_d/(RT)$. R is known ($8.3145J/molK$) and the temperature cancels out leaving; $Q_d = -1000aR = -1000 \cdot (-2.265) \cdot 8.3145 = 18834.66J/mol = 18.8kJ/mol$. The diffusion coefficient formula for mao et al. is described in equation 14 and 15.

$$D_{Al} = 2.265 \cdot 10^{-8} e^{-\frac{-18835}{R \cdot T}} \tag{14}$$

$$D_{Cu} = 8.644 \cdot 10^{-3} e^{-\frac{-130747}{R \cdot T}} \tag{15}$$

Equation 14 and 15 describes the exponential growth nature of the diffusion rate. From this it is observed that Al has a lower pre-exponential diffusion coefficient and a lower activation energy. However, the growth of the diffusion rate is significantly higher in Cu. In the temperature range where Al is semi-solid, Al has a higher diffusion rate shown in Figure 44.

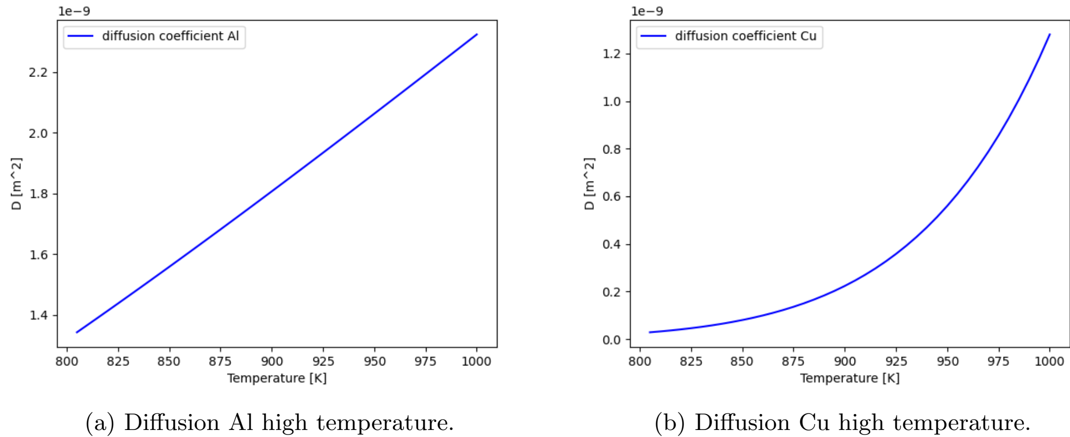

(a) Diffusion Al high temperature. (b) Diffusion Cu high temperature.

Figure 44: Al and Cu diffusion high temperature with regression line.

Source: This work and [63]

5.3 Fick's second law

Fick's second law describes non-steady state diffusion. The concentration gradient is described as a function depending on position and time ($c(x, t)$). Fick's first law is also applicable to non-steady state diffusion, which is why it can be used to derive Fick's second law [65].

$$dc(x) = \frac{(J(x) - J(x + dx))dtA}{Adx}, J(x + dx) = J(x) + dJ$$

When simplifying the equation we have the derivative of flux with regard to x;

$$\frac{\partial c(x,t)}{\partial t} = -\frac{\partial J}{\partial x}$$

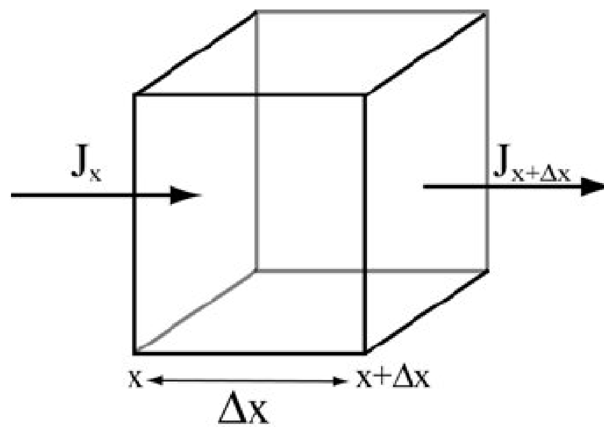

Figure 45: Fick's second law schematic illustration.

Source: [66]

The derivative of flux by thickness in Fick's first law, Equation 12, combined with the simplified equation of the non-steady state concentration gradient creates Fick's second law. Shown in Equation 16. Figure 45 illustrates how the flux differs through a medium.

$$-\frac{\partial J}{\partial x} = D\frac{\partial^2 c}{\partial x^2} = \frac{\partial c(x,t)}{\partial t} \tag{16}$$

The assumption for steady-state diffusion is no accumulation of concentration over time ($\partial c/\partial t = 0$). Applying this to Fick's second law results in Fick's first law.

5.4 Binary alloy diffusion

The previously mentioned driving force for diffusion is the concentration gradient, but a multiphase medium has a different fundamental driving force, namely, the chemical potential gradient. The concentration gradient is only proportional to the chemical potential gradient when the system is ideal in term of the enthalpy of mixing is zero, in other words, the system is dilute. This is not the case for an Al - Cu weld. The chemical potential gradient (or "internal" driving force) for the Al - Cu system is concentration-dependent. The name for the internal driving force is both chemical- and interdiffusion coefficient. A single interdiffusion coefficient that is most often dependent on the composition, describes the rate of diffusion. Kirkendall described this by proving the atoms

switched places with vacancies, rather than what was believed earlier, that atoms switched places with atoms[67]. The conservation of matter is upheld in interdiffusion theory, meaning the sum of flux is zero. Equation 17 represents this with J_V being vacancy flux.

$$J_{Al} + J_{Cu} + J_V = 0 \tag{17}$$

Figure 46 is a vector illustration of equation 17. The smaller atoms have a larger rate of diffusion, meaning $D_{Al} > D_{Cu}$. This in turn creates a higher flux of atoms from Al to Cu and more vacancies travel from Cu to Al.

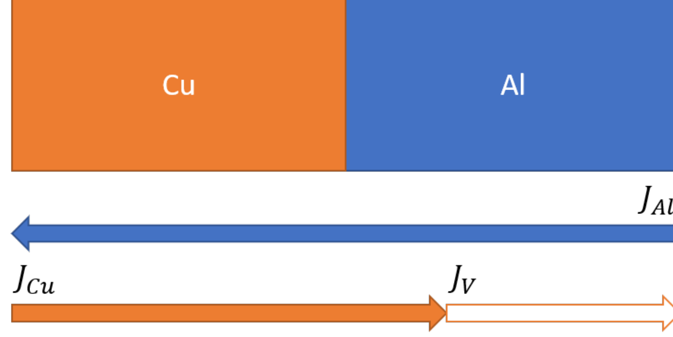

Figure 46: Flux sum schematic illustration.

Source: This work.

Interdiffusion was found to be a function of composition and temperature. This was found through experimentation in the 20th century. Darken had the first theoretical description of the interdiffusion coefficient. He utilized the two intrinsic diffusion coefficients to produce the interdiffusion coefficient. This interdiffusion coefficient is able to produce the depth of the diffusion penetration. Shown in Figure 46, both materials diffuses into each other with different depths. Darken produced equation 18, where $\tilde{D}$ is the interdiffusion coefficient and $\tilde{V}$ is the molar volumes which is the molar mass (M) over density (ρ) [68].

$$\tilde{D} = C_{Al}\tilde{V}_{Al}D_{Cu} + C_{Cu}\tilde{V}_{Cu}D_{Al} \tag{18}$$

This interdiffusion coefficient is used when calculating the concentration profile illustrated in Figure 40. When calculating the concentration profile, the depth of diffusion is calculated. This depth is what determines the IMC thickness. In Fick's second law, the concentration is as mentioned, a function of time and position. This function is showed in equation 19 [69].

$$\frac{c(x,t) - C_0}{C_s - C_0} = 1 - erf(\frac{x}{2\sqrt{\tilde{D}t}}) \tag{19}$$

We assume an infinite long bimetallic bar in our concentration model, meaning, the concentration of is 100% at x = $-\infty$ and the concentration of is 100% at x = ∞ when referencing Figure 46. The modified equation for a bimetallic bar is shown in equation 20.

$$c(x,t) = \frac{C_0}{2}(1 - erf(\frac{x}{2\sqrt{\tilde{D}t}})) \tag{20}$$

A model for concentration profile utilizing equation 20 is shown in Appendix C. It produces an illustration on how the concentration changes over time in Figure 47. The start concentration(C_0) is equal to 1 in our case.

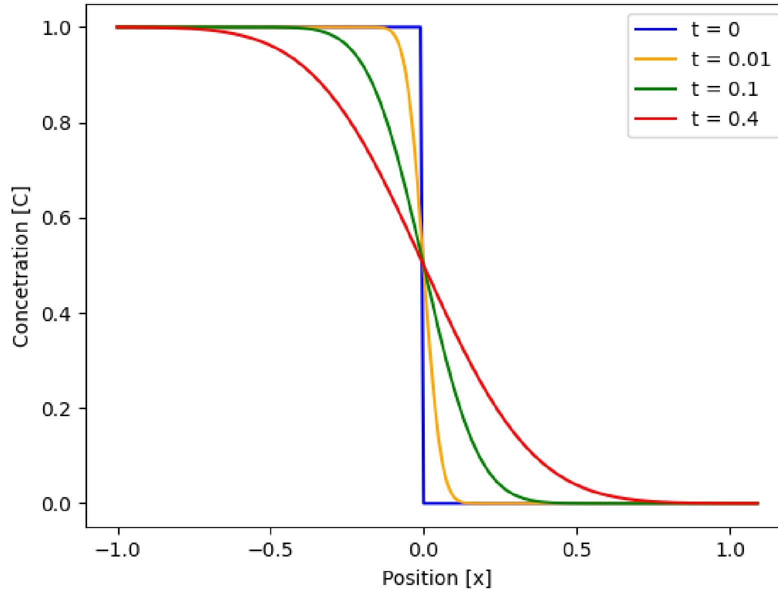

Figure 47: Concentration dependent on position and time.

Source: This work.

The interface is at position x = 0. The graphs conform with the illustration in Figure 40. No mixture of the materials is present at t = 0. As the time goes on, the diffusion increases the mixture of concentration and depth of the diffusion. This model assumes a symmetrical disparity of the alloys. This is a simplification. In reality, the interface can move and the concentration is not evenly spread across the two alloys.

5.5 Isothermal IMC thickness model

The model assumes no accumulation of concentration over time. This is written mathematically in Fick's second law as $\partial J/\partial x = \partial c(x,t)/\partial t = 0$. The only dependent variable for the concentration gradient is now the position of the flux leaving Fick's first law shown in equation 12. The flux in one concentration gradient using Fick's first law is shown in equation 21. The x for position in Fick's first law is replaced with δ.

$$J = \frac{\tilde{D}[C(0) - C(\delta)]}{\delta} \tag{21}$$

The growth rate of the IMC thickness (v) can be described by the change in δ over time, $v = d\delta(t)/dt$. Flux is the mass transporting through an area per time and due to the bonding process being stoichiometric, $Al_xCu_y = Al_x + Cu_y$. Flux can be written as the speed of flux times the inverse of molar volume, $\tilde{V}$[70, 71].

$$J = \frac{\partial \delta}{\partial t} \cdot \tilde{V}^{-1} \tag{22}$$

The molar volume is the molar mass(M) over the density(ρ), $\tilde{V} = M_{Al_xCu_y}/\rho_{Al_xCu_y}$. The flux from equation 22 and 21 can now be combined shown in equation 23.

$$\tilde{V}J = \frac{\partial \delta(t)}{\partial t} = \frac{\tilde{V}\tilde{D}[C(0) - C(\delta)]}{\delta(t)} \tag{23}$$

The concentration coefficient (mol/m^3) cancels out the molar volume(m^3/mol) leaving a simplified version of the equation.

$$\frac{\partial\delta(t)}{\partial t} = \frac{\tilde{D}}{\delta(t)} = \frac{k}{\delta(t)} \tag{24}$$

The $\tilde{D}$ is switched to k. This is the constant used in the literature when the diffusion rate represent the growth of the IMC. Equation 24 is a separable differential equation and is solvable through integration.

$$\int_0^{\delta(t)} \delta(t)\, d\delta(t) = k \int_0^t dt$$

This results in a solution for δ.

$$\delta(t)^2 - \delta(0)^2 = 2kt$$

If the IMC thickness at the start is zero ($\delta(0) = 0$), the function for IMC layer thickness is shown in equation 25.

$$\delta(t) = \sqrt{kt} \tag{25}$$

This theoretical IMC growth formula is used widely by many researchers[72, 71, 70, 73]. The number 2 is included in the diffusion coefficient (k). As shown in equation 13, the diffusion growth coefficient is dependent on temperature creating a growth formula dependent on both time and temperature.

$$\delta(T,t) = \sqrt{2tK_0 e^{-\frac{Q_d}{RT}}} \tag{26}$$

Equation 26 is able to solve a process where the temperature is constant. It can also be used to solve problems which are not constant, like a thermal cycling. However, further steps has to be made.

5.6 Isokinetic IMC thickness model

The isothermal model is not directly applicable to an isokinetic solution where the temperature varies. Certain steps has to take place. Øystein Grong has a method for transforming the isothermal model in an isokinetic solution[74]. This method uses JW Christian's principles[69]. After the isothermal solution is established a reference state is chosen. Two out of the thickness, temperature and time has to be chosen. The third will then be given. Equation 27 shows the temperature and time being chosen to determine the reference thickness.

$$\delta = \delta_r \text{ at } T = T_r \text{ and } t = t_r \tag{27}$$

With the parameters from Equation 27, Equation 25 can be written as shown in Equation 30. This is derived by doing the division described in Equation 28

$$\frac{\delta}{\delta_r} = \sqrt{\frac{k_p t}{k_p^r t_r}} \tag{28}$$

Introduce the timeconstant t^* in Equation 29 and substitute in Equation 28 will then produce Equation 30

$$t^* = t_r \frac{k_p^r}{k_p} \tag{29}$$

$$\delta = \delta_r \sqrt{\frac{t}{t^*}} \tag{30}$$

Substituting t/t^* in Equation 27 with the Scheil integral gives Equation 31. This integral can be numerically integrated and therefore solved iteratively.

$$\delta = \delta_r \sqrt{\int_0^t \frac{dt}{t^*}} \tag{31}$$

This equation works as a sort of 'master curve' in the temperature - time space allowing the function to be used in non - isothermal cases[74]. The reference values has little effect on the outcome. Appendix F is a script utilizing the isokinetic solution that is non - isothermal. The reference time and temperature can be changed and it will not affect the outcome.

6 Aluminum Copper Diffusion Bonding from Literature

The example for diffusion coefficients mentioned in Section 5.2 are at near melting point for Al. HYB busbars are operating at lower temperatures. The threshold for HYB operating temperature is determined by how thick the IMC layer grows. Studies have determined interdiffusion coefficients for IMC growth. These varies depending on the study. This work analyses the IMC growth and compares it with the theoretical model described in Section 5.5. Each IMC phase have a different activation energy and rate of diffusion. Chen and Hwang reported the diffusion rate in phase θ, η, ζ_2 and δ. The diffusion rate was determined with temperatures ranging form 300 - 500°C. Figure 48 and 49 shows the resulting interdiffusion rate of the bulk IMC as well as each phase.

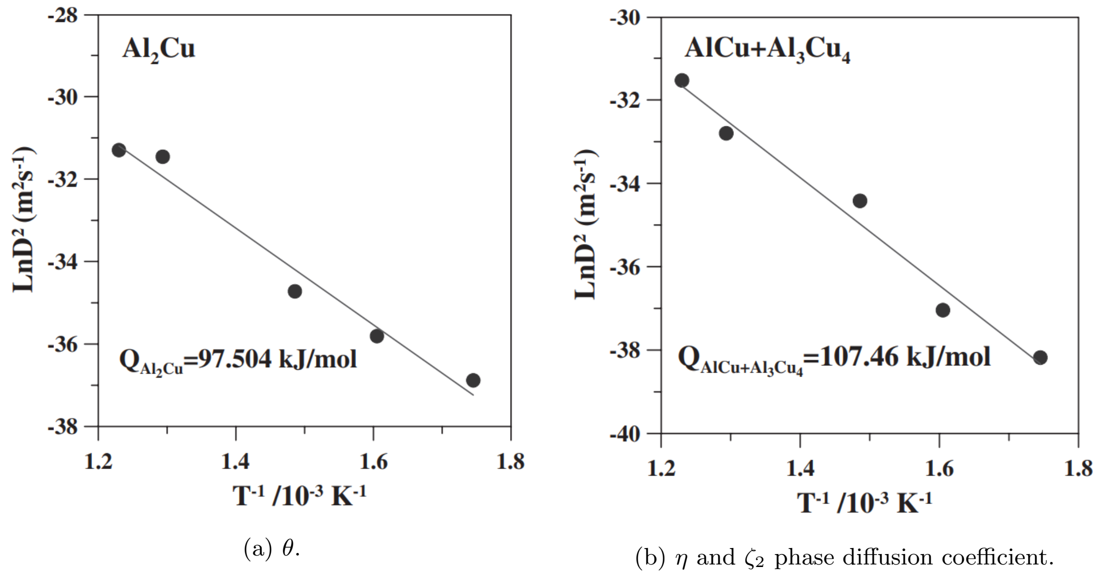

(a) θ.

(b) η and ζ_2 phase diffusion coefficient.

Figure 48: Phase interdiffusion coefficient.

Source: [49]

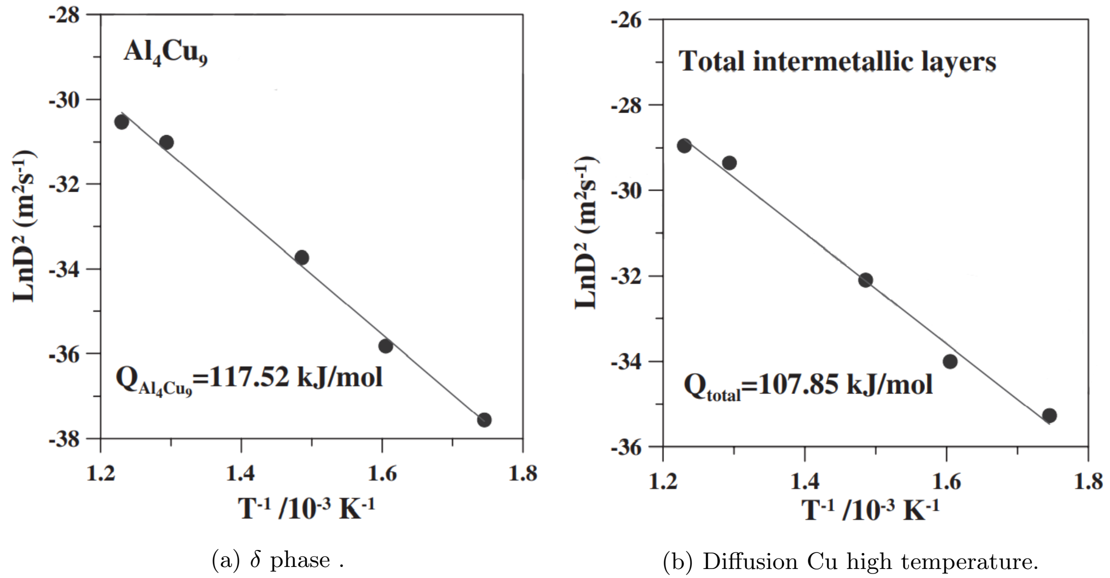

(a) δ phase .

(b) Diffusion Cu high temperature.

Figure 49: Phase and total interdiffusion coefficient.

Source: [49]

Each phase's diffusion coefficient is simplified into one IMC growth coefficient in Figure 49b. All interdiffusion coefficients reviewed, were modelled using the script in Appendix D. Not all temperatures are relevant. Low temperature diffusion coefficients cannot be determined by measuring high temperature diffusion. The max temperature that is relevant for this work is around 340°C. According to Braunovic and Aleksandrov, diffusion rate changes at temperatures above 340°C[75]. Visibly, this is illustrated in Figure 50 as the gradient constant increases. This is not something the theoretical diffusion equation 13 accounts for, meaning a model has to be made for each temperature range. This report is comparing its experimental work to data from 100 - 340°C. Larger temperatures cannot be used to predict busbar behaviour under normal working conditions. This unfortunately excludes a large part of the literature on Al - Cu diffusion bonding.

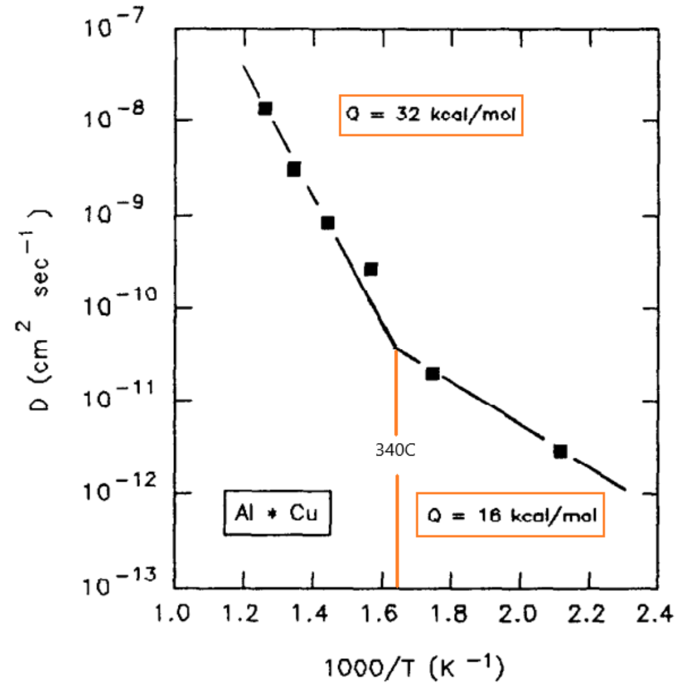

Figure 50: Shift in interdiffusion coefficient.

Source: [75]

6.1 Liu et al.

Liu et al. reported on Al - Cu IMC growth at three different temperatures and holding times shown in table 10. The welding technique was ball bonding, using the machine KS Maxum Elite automatic wire bonder. A 20.32 μm diameter Cu wire was bonded to a thin Al pad. The report had a start IMC thickness of 200 nm and analyzed the thickness with an SEM - Energy Dispersive X-ray Spectroscopy (EDX). The surface was etched with a nitric acid which slightly damaged the IMC. However, the layer thickness was not compromised.

Temperature ($^{\circ}C$)	Holding time (h)	k (m^2/s)
150	3000	$2.09 \cdot 10^{-}20$
200	2000	$1.38 \cdot 10^{-}19$
250	1000	$1.35 \cdot 10^{-}18$

Table 10: Liu et al. interdiffusion coefficient at different temperatures[71]

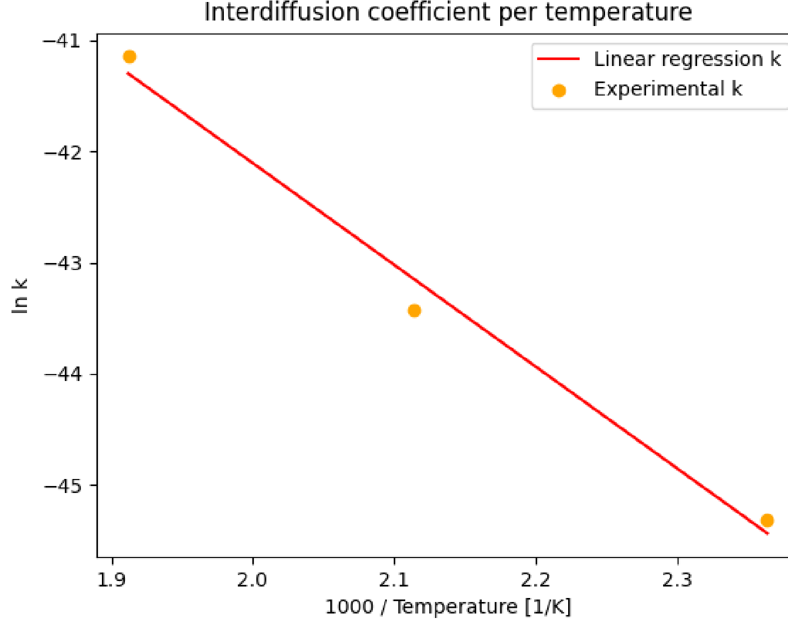

Figure 51: Liu et al. interdiffusion coefficient

Source: [71], Appendix D

This resulted in a $k_0 = 4.647e - 11m^2/s$ and a $Q_d = 76130J/mol$ resulting in an interdiffusion rate shown in equation 32.

$$k_{Liu} = 4.647 \cdot 10^{-11} e^{-\frac{76130}{RT}} \tag{32}$$

6.2 Xu et al.

Xu et al. bonded 50.8 μ diameter Cu wires to 3 μm thick Al plates. The welding was done by ball bonding, using an ASM Eagle 60 ball/wedge automatic bonder. The frequency used was 138 kHz. Temperature and holding times are shown in table 10. TEM - EDX were used to measure the IMC thickness which were clearly visible. The only observed phases were AlCu and Al_4Cu_9, and the crystallographic structure were of Al_4Cu_9 was identified as $P - 43m$ conforming with the theory from table 4.

Temperature ($°C$)	Holding time (h)	k (m^2/s)	Measurements
200	200	$2.27 \cdot 10^-18$	4
250	200	$2.46 \cdot 10^-17$	13
300	16	$1.67 \cdot 10^-16$	3

Table 11: Xu et al. interdiffusion coefficient[76].

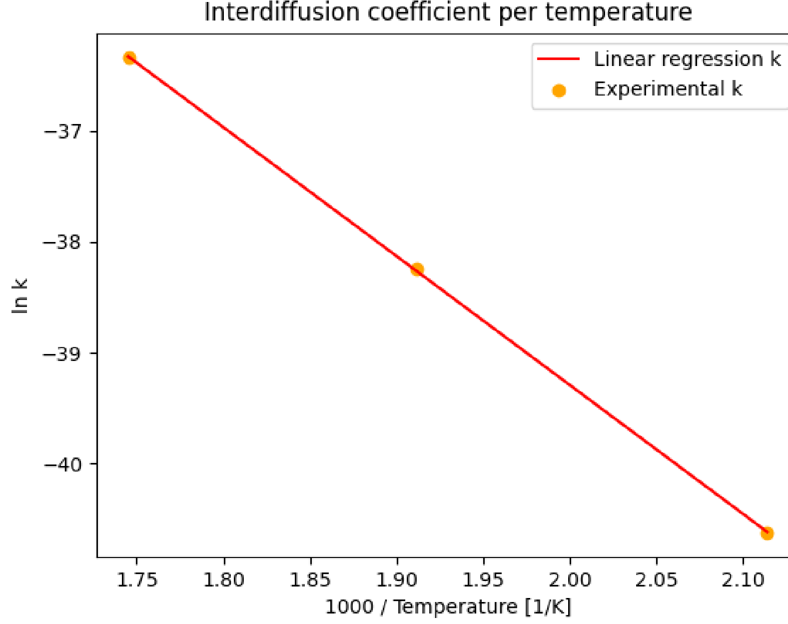

Figure 52: Liu et al. interdiffusion coefficient.

Source: [76], Appendix D

This resulted in a $k_0 = 1.043e - 7m^2/s$ and a $Q_d = 96505J/mol$ resulting in an interdiffusion rate shown in equation 33.

$$k_{Xu} = 1.043 \cdot 10^{-7} e^{-\frac{96505}{RT}} \quad (33)$$

6.3 Braunovic and Aleksandrov

Before starting the diffusion process, an Al rod was friction welded to a Cu rod. Resulting in a 5 cm diameter, 10 cm long bimetallic sample. Figure 50 shows all temperature plots for the IMC thickness. Isolating the lower temperature range of 250°C and 300°C gives us Figure 53. The IMC thickness was measured with SEM and Optical Microscope (OM). Looking at table 12, both diffusion processes were held for 240 hours and 5 thickness measurements were conducted. The pre-exponential diffusion coefficient differs quite alot from the previous two.

Temperature ($°C$)	Holding time (h)	k (m^2/s)	Measurements
250	240	$3.5 \cdot 10^-16$	5
325	240	$2.46 \cdot 10^-15$	5

Table 12: Braunovic and Aleksandrov interdiffusion coefficient[75].

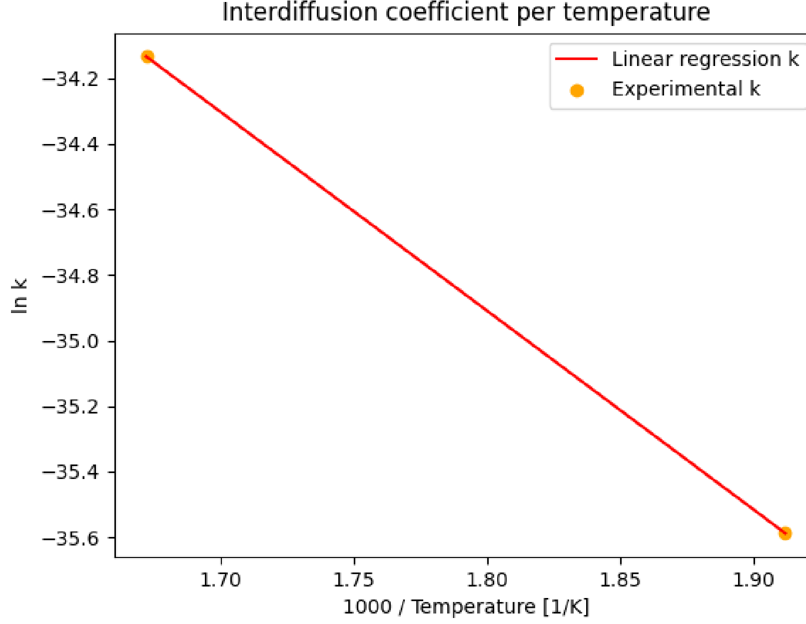

Figure 53: Braunovic and Aleksandrov interdiffusion coefficient.

Source: [75], Appendix D

This resulted in a $k_0 = 3.832e-11m^2/s$ and a $Q_d = 50457J/mol$ resulting in an interdiffusion rate shown in equation 34.

$$k_{Brau} = 3.832 \cdot 10^-11e^{-\frac{50458}{RT}} \tag{34}$$

6.4 Kim et al.

A Cu wire was bonded to a thin Al plate. The IMC growth were measured at three different temperatures shown in table 13. A convection oven was used and nitrogen gas was injected into the oven to prevent oxidation. SEM and OM were used in conjunction to measure IMC thickness. SEM images are able to view IMC thickness at 150°C after 24 h and only after 2 h at 250°C. The report managed to identify the IMC phases by EDX. Like Xu et al. AlCu and Al_4Cu_9 were found. In addition to these Al_2Cu was also formed. The authors have stated it being difficult to differ between the IMC phases.

Temperature ($°C$)	Holding time (h)	k (m^2/s)	Measurements
150	50	$1.878 \cdot 10^-20$	2
250	300	$6.833 \cdot 10^-18$	5
300	300	$6.027 \cdot 10^-17$	5

Table 13: Kim et al. interdiffusion coefficient[72].

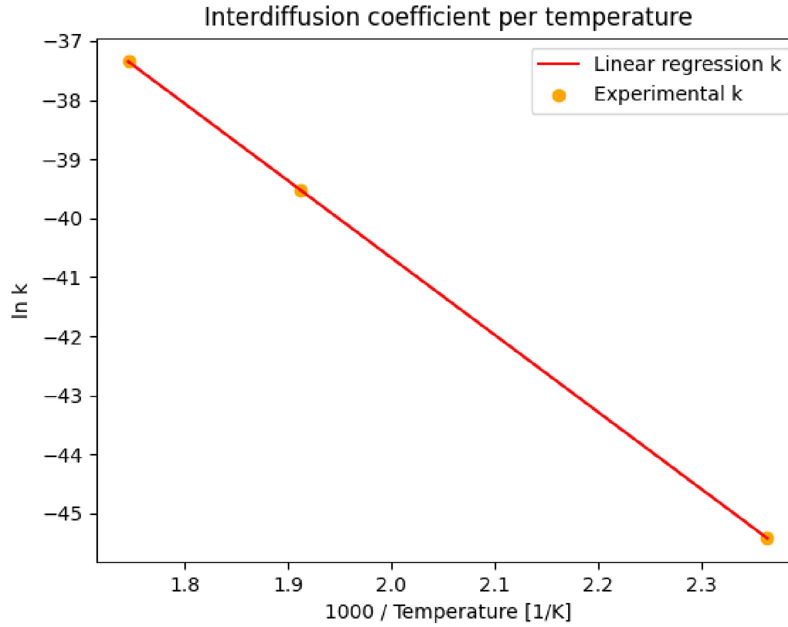

Figure 54: Kim et al. interdiffusion coefficient.

Source: [72]

This resulted in a $k_0 = 4.655e - 7m^2/s$ and a $Q_d = 108471 J/mol$ resulting in an interdiffusion rate shown in equation 35.

$$k_{Kim} = 4.655 \cdot 10^-7 e^{-\frac{108471}{RT}} \tag{35}$$

6.5 Comparison

The literature reports vastly different interdiffusion coefficients. Using the theory on isothermal interdiffusion from section 5.5, the different growth measurements can be used to predict growth. This model is shown in Appendix E. Figure 55 demonstrates the different growth of IMC for the reviewed literature. The temperature is 523 K (250°C) and held for one month.

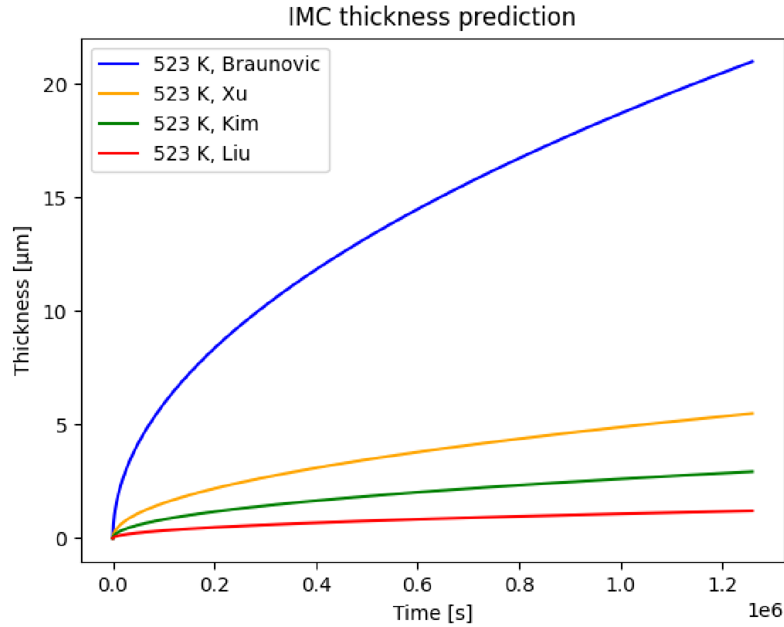

Figure 55: IMC growth from literature.

Source: [72, 75, 76, 71]

7 Observing IMC thickness

Numerous test samples were ground, polished and observed via microscope. The best samples were originally created by SINTEF as they had an automated polishing procedure. Like the pre-master project, it was difficult to create a smooth surface through grinding and polishing. This is probably due to the specimen being of dissimilar metals and being soft. After many attempts, access to new equipment, and help from the employees at the Department of Materials Science at NTNU, a procedure was made which created very well polished samples.

7.1 Optical microscope

SINTEF managed to create an even and smooth surface during polishing. The specimen was etched to highlight the IMC interface. Figure 56 has a shadow on the interface which is probably due to the IMC highliting etching. It looks problematic on both Figure 56 and 57a. However, when increasing the magnification, the interface becomes clear with a very smooth surface. No indication of IMC is visible at the scale of OM. OM is limited by Abbe's diffraction limit. This is the resolution of optical imaging (d). Normal aperture (NA) and the wavelength (λ) determine how small the resolution is. Equation 36 calculates the resolution[77].

$$d = \frac{\lambda}{2NA} \tag{36}$$

The diffraction in light creates an unavoidable cluster of photons that cannot be differed from one another. Meaning, the picture will not be clear no matter how large the lens is. This is only solved by lowering the wavelength to either UV or X-ray, or use other methods like SEM and TEM.

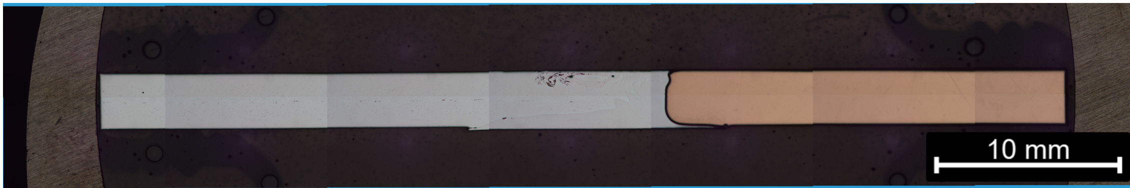

Figure 56: Macro perspective.

Source: This work.

(a) 50X magnification OM.

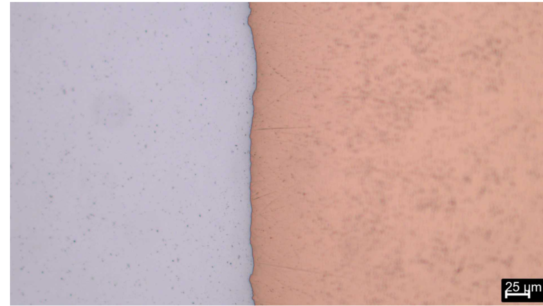

(b) 200X magnification OM.

Figure 57: 50, 200 and 500 magnification of HYB weld.

Source: This work.

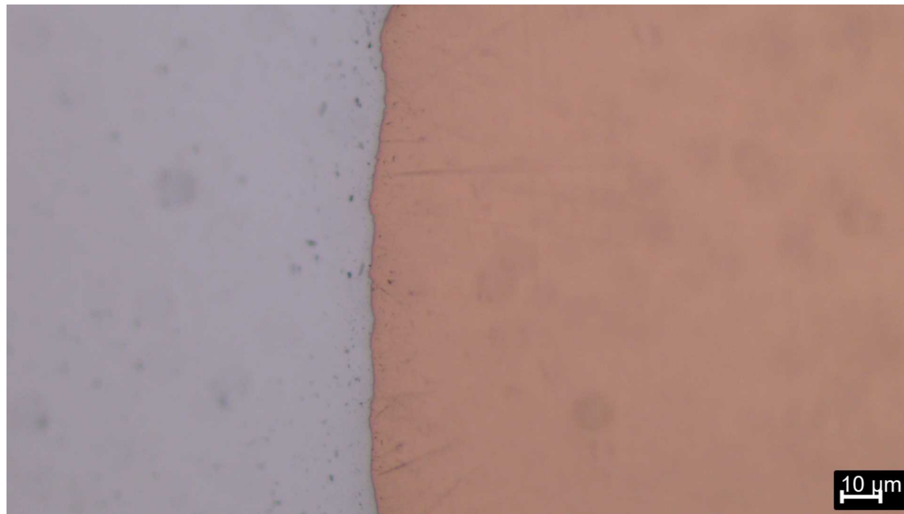

Figure 58: 500X magnification OM.

Source: This work.

7.2 Scanning electron microscope

SEM is one method which is able to go lower than Abbe's diffraction limit. The SEM used is the Zeiss Supra 55 VP. Electrons as opposed to light are used to create a picture. Electrons are shot by an electron gun in concentrated beams at the surface, scanning one row at a time. These electrons create different mechanisms which SEM is able to use when picturing a test piece. In this report both Secondary Electrons (SE) and Backscattered Electrons (BSE) are utilized. SE are electrons that get released from the test piece when the electron beam activates it through its energy. BSE are in contrast, a result of an elastic collision of the electron beam hitting the atom. The atom

will then scatter electrons which are detected in a sensor. BSE will come from deeper areas while SE will come from the very top of the surface[78].
The SEM samples has to be ground down as well as polished like the samples for OM. Once this is done, the sample has to undergo a degassing process for a minimum of 12 hours. This protects the SEM when the specimen is in the vacuum chamber. Figure 59a shows a macro picture of an AA1070 unheated sample interface. The SEM will show the Cu as lighter grey while Al is darker. As seen in Figure 59a, one Cu particle has dispersed into the Al SZ. Figure 59b shows the IMC interface at 1000X magnification. There, grinding lines are clearly visible caused by a poor grinding job. These affect the sample even worse when looking deeper like what is shown in Figure 60 at 30 000X magnification. The lines become deep valleys and other grooves are visible that also is created by grinding error.

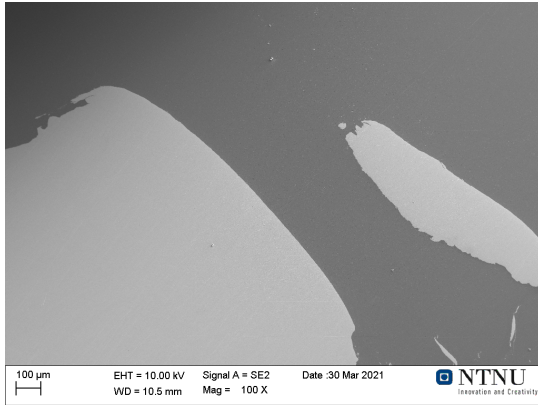

(a) Unheated 100X magnification SEM.

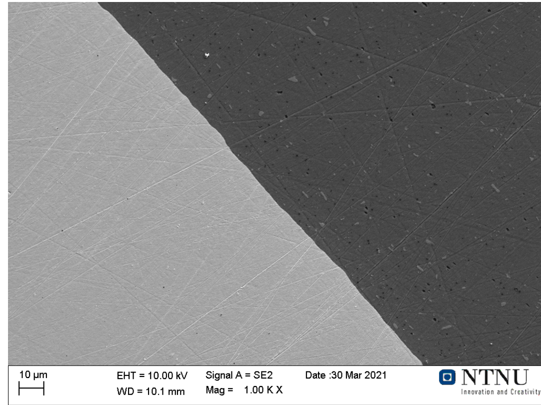

(b) Unheated 1000X magnification SEM.

Figure 59: Unheated 100 X and 1000 X magnification of HYB weld in SEM.

Source: This work.

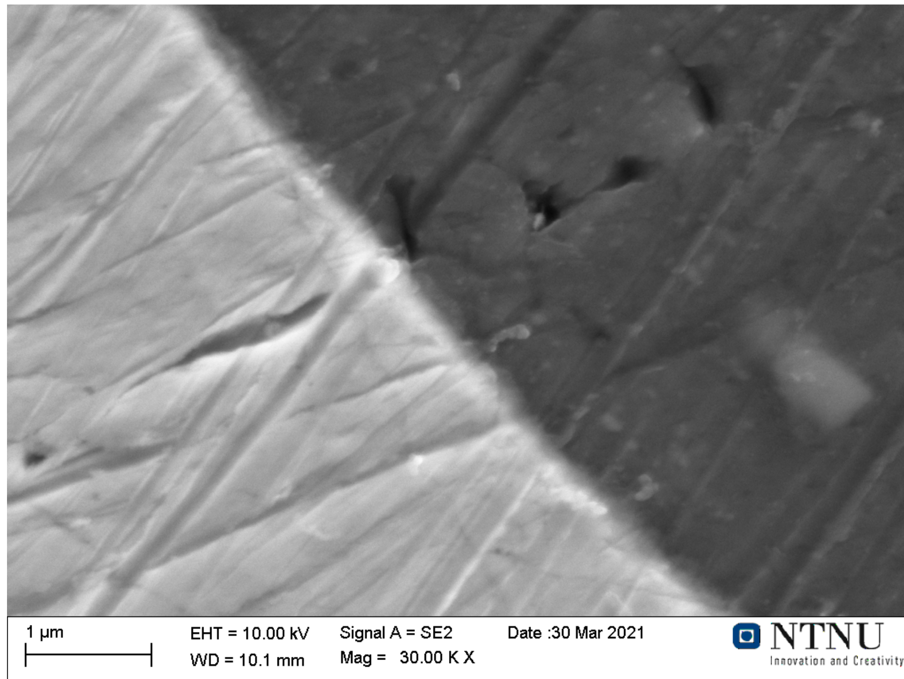

Figure 60: 30kX magnification SEM.

Source: This work.

Interestingly, the Cu and Al are separated by an unclear line. This line is difficult to analyse, but the indication is either IMC or a shadow effect caused by a valley at the interface. This image is not good enough for specifying how thick or if there is an IMC layer.

7.3 IMC thickness measurments

The best method for measuring IMC layer thickness is through TEM. TEM has the highest resolution and is able to be more accurate. However, TEM requires more expertise as supposed to the SEM. No IMC layer was visible in SEM so luckily, an unheated AA6101 sample was treated and analyzed in TEM. All other samples had to be analyzed in SEM due to high demand for the TEM at NTNU. The holding time is equal to the electric test samples shown in table 6.

Temperature ($^{\circ}C$)	Holding time (h)	Analyzed with
0	0	TEM
200	1152	SEM
250	242	SEM
250	430	SEM
250	731	SEM

Table 14: IMC thickness sample matrix.

7.3.1 Unheated 6101 TEM samble

TEM is similar to SEM in that electrons are used to construct an image. However, it is different in that TEM is transferring electrons through the sample and not detecting SE or BSE. The electron source is transferring electrons through electromagnetic lenses before it goes through the sample. The transmitted electrons will then go through more electromagnetic lenses before the detector collects the electrons. The TEM is able to detect single atoms and determine lattice parameters[79]. STEM is also utilized for identifying compounds and concentration.
The sample requires a special preparation due to the electrons having to go through it. The sample gets to around 100 nm thickness by Focused Ion Beam (FIB) milling system[80]. Figure 61 shows the lamella post FIB milling. Like the previous SEM images, SE are used to produce this image showing the dark section to the left as Al while the lighter section to the right as Cu.

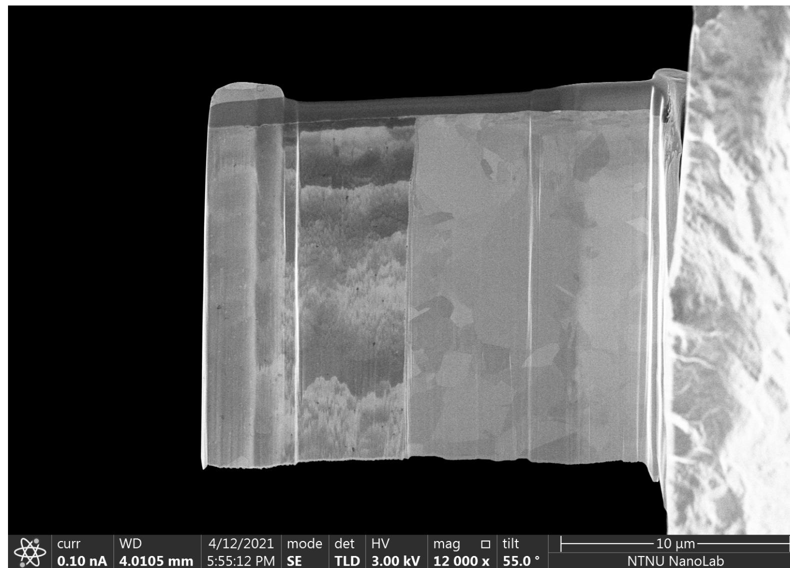

Figure 61: TEM sample post FIB.

Source: This work.

This lamella was then analyzed in TEM. The TEM shows Cu as darker while Al is the lighter material. The FIB milling managed to create an even smooth surface without any deformities or impurities. The IMC layer is slightly visible in Figure 62.

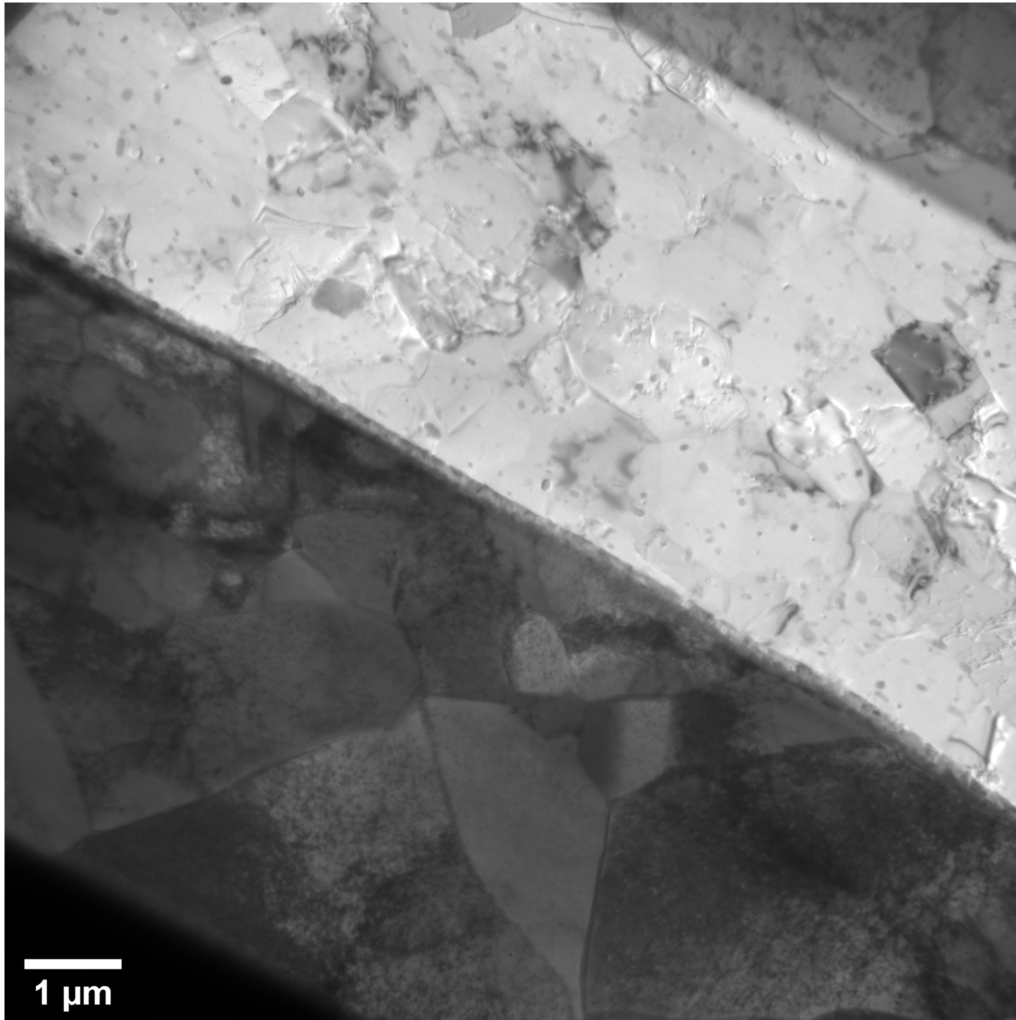

Figure 62: TEM sample post FIB.

Source: This work.

Increasing the magnification to 20 000X shown in Figure 63, allows for a clear view of the IMC layer. The mixing of Cu and Al are observed through the layer which clearly shows a mix of the metals. Separating the diffusion layers into phases is very difficult to accomplish at such a small thickness. However, some phases were observed. EDX analysis was conducted and managed to create a concentration profile like what is illustrated in Figure 47, and determine the alloying elements both within Al and Cu seen in Appendix J. Some indication of vacancy migration from the Cu is visible by its lack of structure near the IMC layer. The vacancies might have changed the structure when traveling to the IMC and Al. Figure 62 demonstrates this best and conforms previously mentioned diffusion theory on flux.

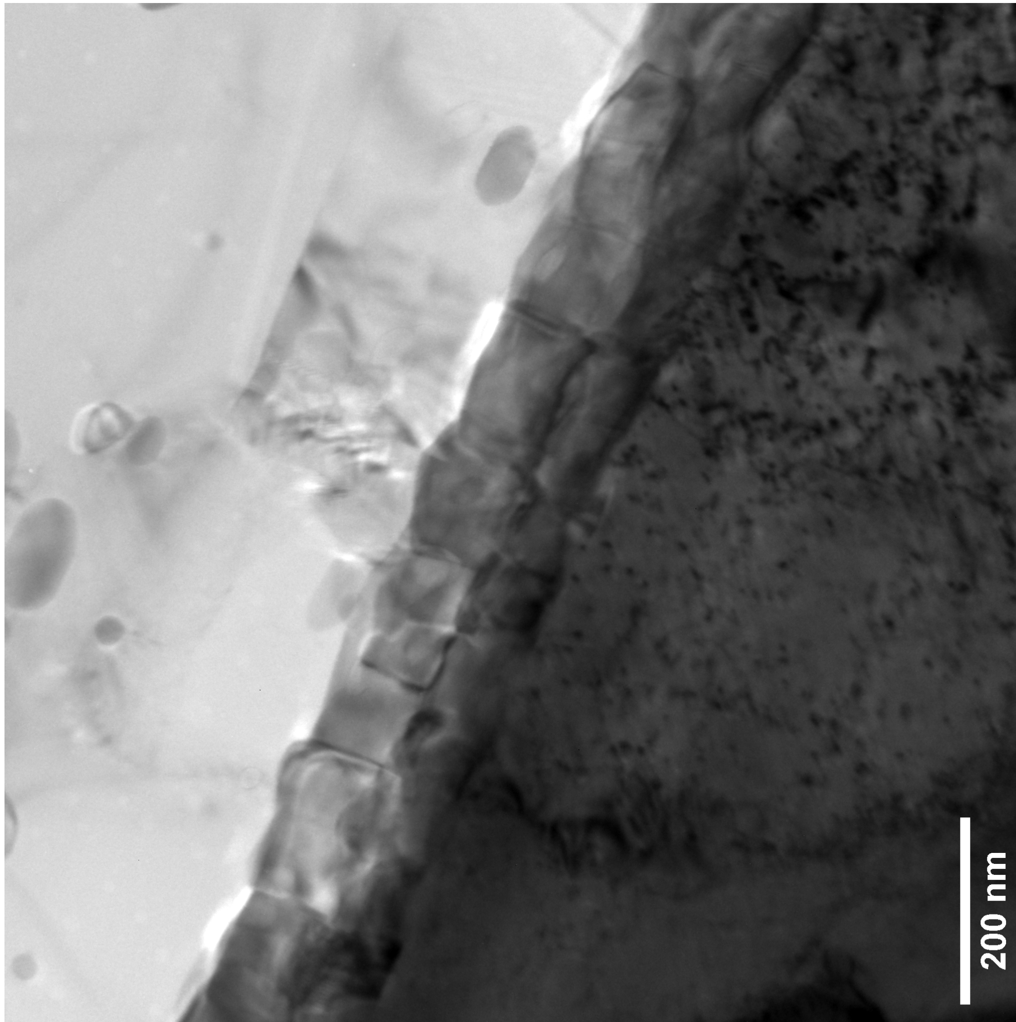

Figure 63: TEM sample post FIB.

Source: This work.

TEM EDX analysis of the sample created the concentration profile in Figure 64. As previously illustrated by Figure 47, a clear penetration of Cu atoms into Al as well as Al atoms into Cu is observed. The concentration is mostly smooth across the interface like what the theoretical equations are describing. However, a constant 33.3 % Cu is observed for around 70 nm. This conforms with IMC theory; indicating a layer of Al_2Cu (θ) phase. These two methods indicate a start IMC layer of 200 nm. Diffraction pattern analysis with TEM EDX found the phases Al_4Cu_9 and Al_2Cu. The images are in Appendix M. Note that not all diffraction patterns were identified so there is a possibility of more phases.

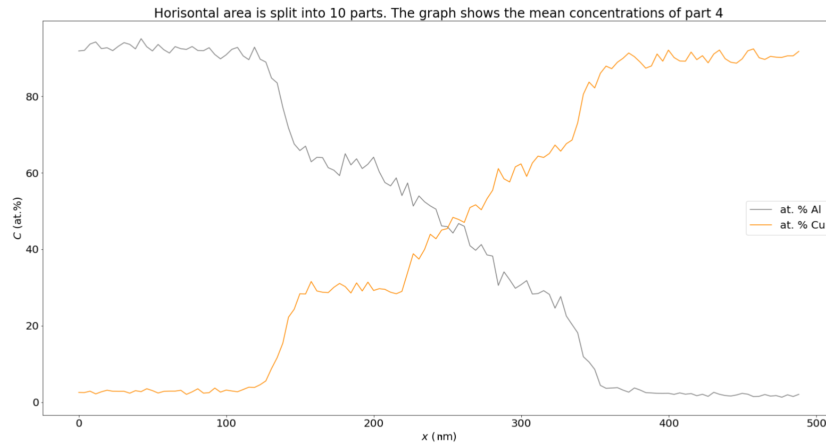

Figure 64: TEM EDX concentration profile.

Source: This work.

7.3.2 Heated samples

All heated specimens were observed in SEM and SEM EDX. The EDX are in Appendix L. The SEM pictures that follows have very little scratches and holes due to an improvement in grinding and polishing. The polishing and grinding problem was solved due to help from people experienced in polishing metal samples and an improvement in equipment. Silicon carbide grinding papers were used, starting coarse and going finer. The first paper was a 320 grid paper, this was followed by 500, 800, 1200, 2000 and then a 4000 grid paper. The samples were manually handled and held evenly while making sure scratches from the previous papers disappeared after each step. The samples were subsequently polished. First with a 3 μm polishing disc followed by a 1 μm disc. These were manually handled as well, and the samples are rotated opposite to the rotation of the disc. In this case, clockwise because the disc was rotating counter clockwise. The samples were manually rotated 200 times on the 3 μm and 50 times on the 1 μm disc. A mix of diamonds and blue lubricant is sprayed on the discs while this process is occurring. The last step was 20 second with oxide polishing.

7.3.3 200 degrees Celsius

A specimen was in the oven at 200°C for 48 days. The specimen was subsequently observed under SEM and analyzed both with BSE and SE. Both techniques revealed the same amount of IMC thickness. The thickness was measured at eight places and the average thickness was 0.876 μm. The technique used was visually measuring the layer. The IMC layer is visible because of the atomic number of Cu and Al. The higher atomic number, in this case Cu appears lighter than the lower atomic number Al[81]. The gray interface is caused by the materials metallurgically being bonded into an IMC layer appearing as a mix between the two.

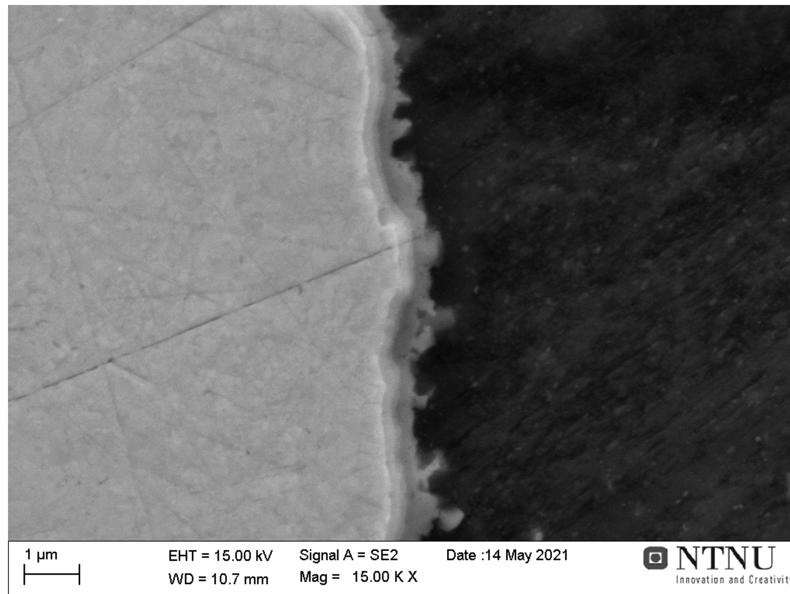

Figure 65: SEM SE 200°C.

Source: This work.

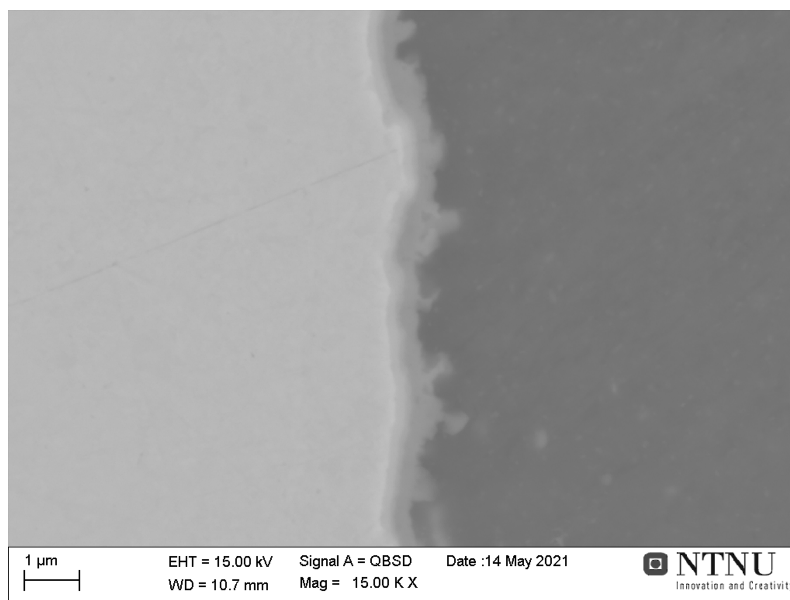

Figure 66: SEM BSE 200°C.

Source: This work.

7.3.4 250 degrees Celsius

Three pieces were measured in the SEM heated at 250°C. These were measured the same way the 200°C sample was measured; by visually observing the layers. The IMC layer is observed to grow as the time goes on. Figure 67 and 68 show the IMC layers in the way that the Cu becomes darker towards the Al side.

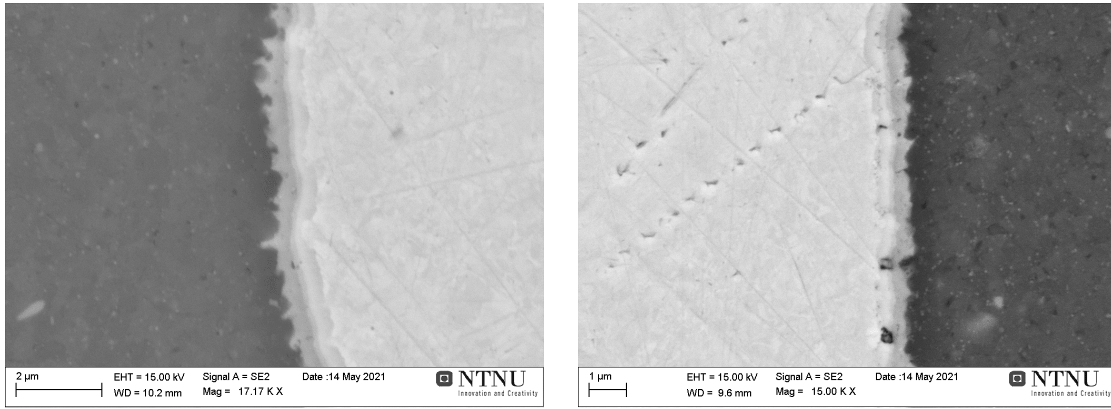

(a) 250°C 242 h. (b) 250°C 430 h.

Figure 67: 250°C for 242 h and 430 h SEM images.

Source: This work.

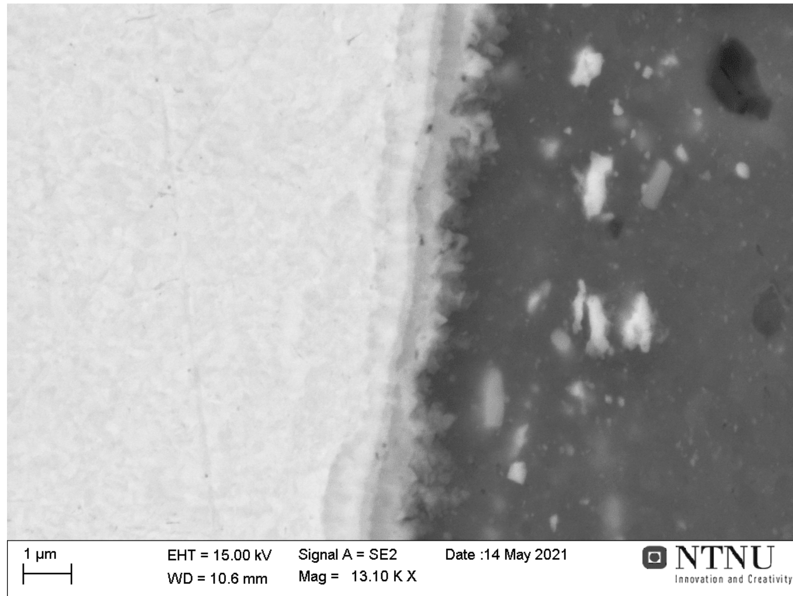

Figure 68: 250°C for 731 h SEM image.

Source: This work.

7.4 HYB intermetallic growth model

Temperature ($°C$)	Holding time (h)	thickness (μm)	SD	SE	measurements
Unheated	0	0.2	-	-	-
200	1152	0.77	0.192	0.064	9
250	242	0.876	0.0894	0.0316	8
250	430	1.074	0.164	0.055	9
250	731	1.655	0.28	0.089	10

Table 15: IMC thickness measurements with standard deviation and standard error.

These measurements shows the growth relationship between temperature and time visible in Figure 69. The vertical bars are the standard error in each measurement using equation 2 and 3, like the

hardness measurement. The graph starts from 200 nm as that is what TEM determined. The lower temperature sample is only one measurement which does not show the parabolic nature of the growth theory in equation 25. The higher temperature sample on the other hand should have its second measurement placed higher if it were to represent a perfect parabolic function.

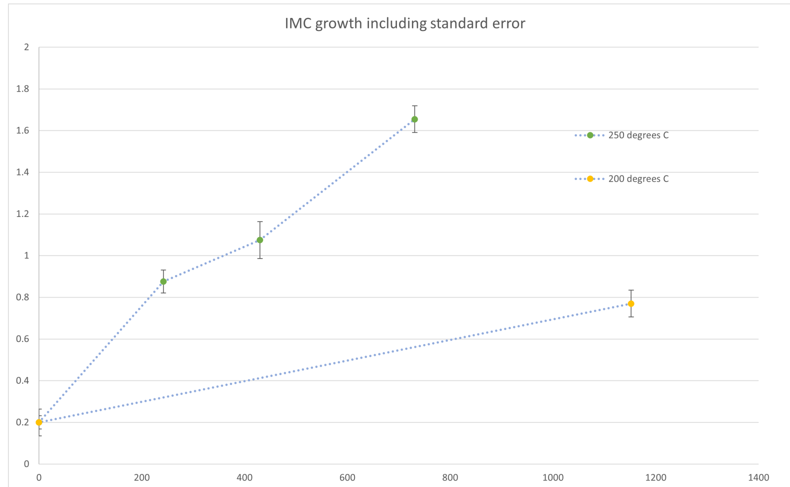

Figure 69: 200°C and 250°C growth with μm in y-axis and hours in x-axis.

Source: This work.

The interdiffusion coefficient is derived from the experimental data shown in Figure 69. Scikit - learn is used for deriving the interdiffusion coefficient at 200°C and 250°C[64]. The script is attached as Appendix G. The model retrieves each k value which is 1.44682903e-19 m^2/s for 200°C and 7.55184036e-19m^2/s for 250°C. Each graph is shown in Figure 70.

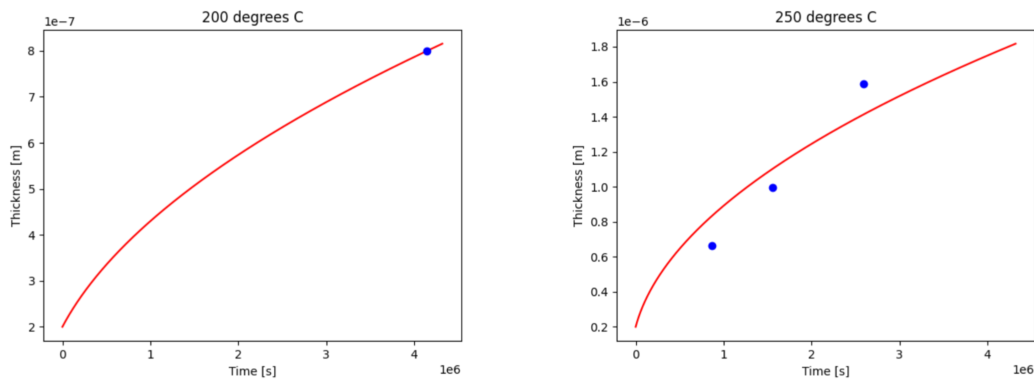

(a) Interdiffusion at 200°C.

(b) Interdiffusion at 250°C.

Figure 70: Interdiffusion from experimental data at 200°C and 250°C.

Source: This work.

Combining these two by using the model in Appendix D creates Figure 71. It also calculates the interdiffusion function. Only two temperatures result in a simple interpolation. It would be beneficial to have a third temperature as its placement on the line would be an indication of how exact the measurements have been.

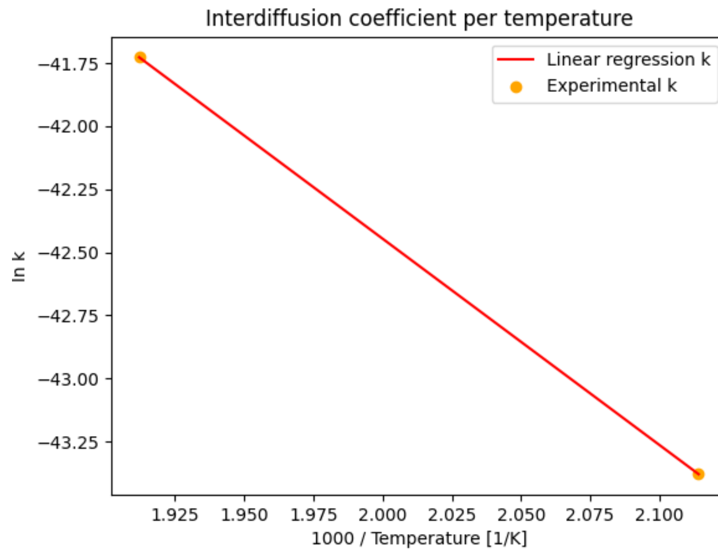

Figure 71: HYB k value.

Source: This work.

Equation 37 is the interdiffusion coefficient. The pre-exponential interdiffusion coefficient is $4.644 \cdot 10^{-12}$ m^2/s and the activation energy is 67975 J/mol.

$$k = 4.644 \cdot 10^{-12} e^{-\frac{67975}{RT}} \tag{37}$$

Using this, Figure 72 shows the predicted growth at 250 $°C$, 200 $°C$ and 150 $°C$ temperatures for 1 month.

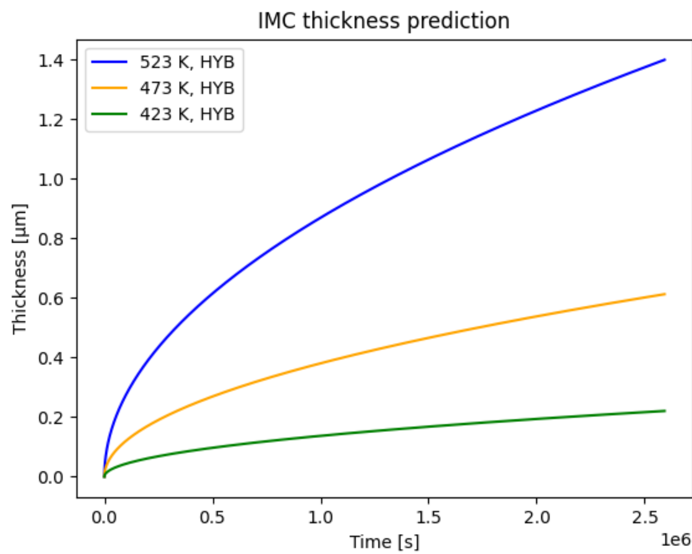

Figure 72: IMC growth from experimental data at different temperatures.

Source: This work.

8 Discussion

8.1 structural

The HYB technique is a new technique especially with regard to Al - Cu welding. This is the first report on the mechanical properties of an Al - Cu HYB weld. Initial tensile testing have been a success with the sample fracture outside of the weld interface. There was also a weld which showed a fracture on the interface. The bending tests showed a desirable outcome from the top down, but an undesirable outcome from the bottom up. Both the tensile tests and bending tests showed the weakness in the interface being on the bottom. Even the tensile test with a fracture outside of the SZ showed a small crack at the bottom of the interface. SEM and TEM analysis were conducted around the middle of the weld interface. No weld defect was observed when analyzing with the SEM as well as no SEM or TEM picture showed any weld defects. This indicates a solid bond in the middle and mechanical tests indicate a solid bond on both the top and middle of the interface. The hard and brittle nature of the IMCs makes any weld defect protrude easier along the IMC interface under stress. Therefore, the poor bond at the bottom of the interface is a weakness that affects the entire interface. Fatigue tests are highly relevant and will demonstrate more of the bond characteristics. A busbar might be under conditions with heavy vibrations in for example a boat with big electric battery packs. Corrosion tests are also of interest as it is a known problem in Al. More so than Cu because of its noble nature.

8.2 Conductivity

The expected results were an increased amount of resistance in regards to the IMC growth. However, the measurements did not link increase in IMC thickness to increased resistance. This is due to the source of error being larger than the increase in resistance. There are multiple sources of error regarding the resistance measurements. Very small amounts of error can render the results inconclusive. The cutter used was not precise enough to cut completely geometrically similar test samples. The samples also had a variance in thickness, meaning it had to be measured to get the true resistance over the test piece. Wire positions are able to also affect the results. Luckily, the series measurement method with linear regression negated some of that error. The FM is a thin wide layer on top while it is stirred in vortices and pushed downwards. Being thin in the middle and thickening towards the bottom. The FM has a higher resistance compared to the Al BM, which will in turn affect the linear regression and distort current flow lines. The pieces were ground down in thickness due to the contact area being large. This negated some of the error, but the contact area were still a little larger than the cross-section area, lowering the IMC resistance.

The goal was to connect the increase in IMC thickness to the increase in IMC resistance. The increase in resistance will in turn increase the temperature if the current is constant. This is an important factor for calculating the growth of IMCs and therefore the lifetime of the busbar. Some of the literature attributes an interface resistance to a bond resistance which has an unknown cause. This can be the case for the HYB samples and the increase in resistance from thicker IMC layer might not be large enough to detect the difference. Using Moiseenko et al. resistivity for IMC bulk resistivity, the resistance of a 4 mm^2 2 μm thick IMC layer would amount to 0.0388 $\mu\Omega$[52]. Al - Cu welds that are connected in parallel are also complicated. The conductivity reported are often worse than the theoretical conductivity for the BMs. The maximum temperatures of the ovens available were 250°C which made it difficult to grow large amounts of IMC. Detecting such small amounts of IMC with resistance measurements proved to be a great challenge. Thicker IMC layers or higher percision measurements are required to detect and characterize the HYB IMC resistance.

8.3 IMC thickness model

The literature differs widely on IMC growth. Some have vastly higher interdiffusion rates than others. The reviewed studies had different welding techniques although all were solid-state welding techniques. This probably had some effect on the growth rate. The friction welded joint had the

highest amount of growth. Any disbursement of BMs allows for IMCs to grow apart from the BMs which increases the IMCs. The reviewed studies used pure Cu, but the Al alloys were different. The amount of vacancies and and variation in alloys all create different interdiffusion coefficients which makes IMC grow differently. All these factors affect the growth of IMC and there are not literature which compares the same alloys. Figure 73 shows the reported HYB model compared to the literature.

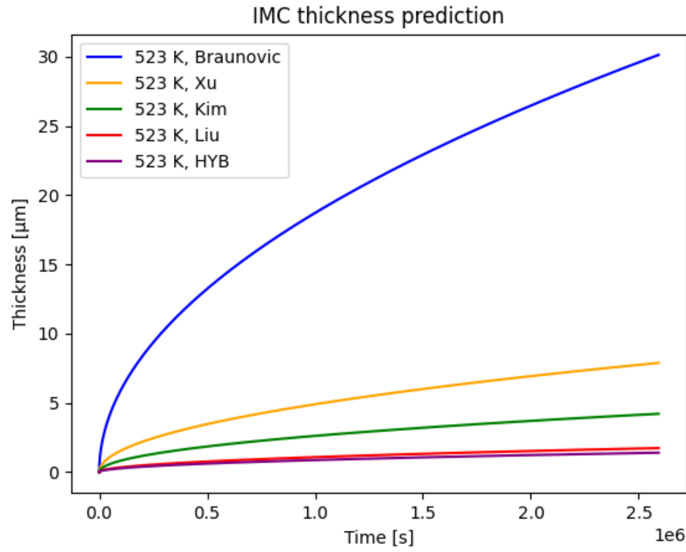

Figure 73: Isothermal growth with HYB.

Source: This work.

As seen the HYB shows the lowest amount of growth compared to the others. Liu et al. has the most similar growth compared to HYB and its comparison is shown in Figure 74. The result differ with the Liu et al. sample growing 23 % more compared to the HYB weld after one month.

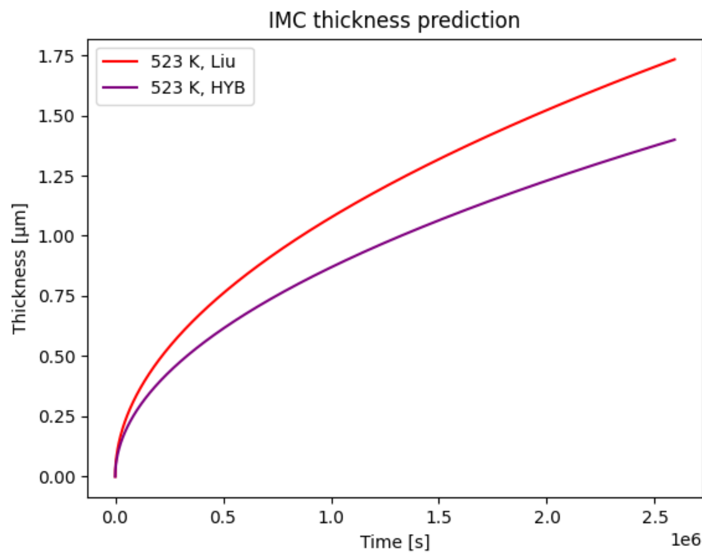

Figure 74: Liu et al. and HYB comparison.

Source: This work.

The TEM EDX were very consistent with the images produced. The SEM EDX did not show the same growth as the SE and pictures produced. The EDX images showed more growth. The TEM should be used to have better accuracy when measuring such small lengths in IMC thickness. That being said, the SEM EDX can be used as a worst case scenario as the growth is for certain not more than what the EDX shows. The data from the isothermal testing was used to create a isothermal model and a non-isothermal model. The non-isothermal model can be used to predict the lifetime of a busbar in real use. The temperature profile of the busbar. An example of another use case for the non-isothermal model is the welding process. Figure 75 shows a potential temperature profile for HYB weld.

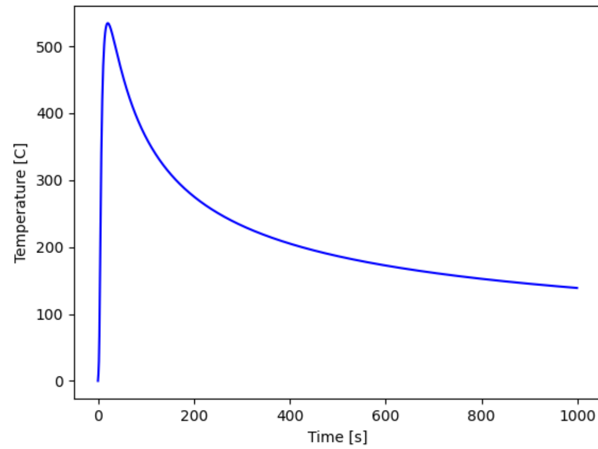

Figure 75: Temperature in HYB weld.

Source: This work.

Figure 76 is the isokinetic model with the temperature profile from Figure 75. Almost all the IMC growth occurs at the peak temperatures and rapidly tapers down. This makes sense due to the parabolic growth nature of IMC and temperature. The amount of IMC growth in HYB was found to be 200 nm after welding. The script shows approximately 19 nm growth after the welding process. This makes sense due to the fact that the model is not accounting for the diffusion rate having higher growth at temperatures above 340°C. Nevertheless, the data from this report cover the normal temperature range for a busbar and the isokinetic model can predict the lifetime of a busbar in terms of IMC growth.

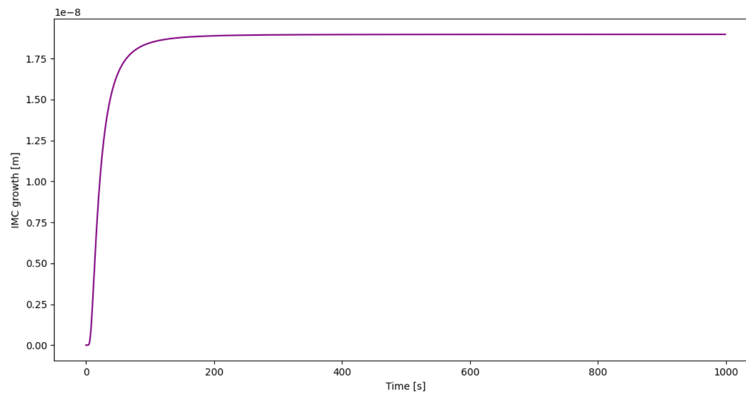

Figure 76: Isokinetic solution for IMC thickness in welding.

Source: This work.

9 Conclusion

1. HYB has managed to create a solid bond when welding Al - Cu. One set of welding parameters allows for the sample to break in the Al BM. This allows for the joint to be stronger than the weakened zone in HAZ. Bending tests also held at the interface from one side while the other broke along the weld interface. A root defect was observed in all tests. The FM has trouble applying sufficient pressure and heat throughout the entirety of the weld.

2. TEM and SEM images showed a solid bond without any weld defects. The images were taken from the middle of the weld interface.

3. The difference in IMC thickness did not grow the resistance enough for it to be detectable on the conductivity tests. All tests did show an increase in resistance at the interface indicating a "bond" resistance which is not caused by the IMCs inherent resistivity.

4. TEM and SEM analysis characterized the IMC thickness for the unheated sample, 200 °C and three 250 °C samples. IMC phases for an unheated weld was found to be Al_4Cu_9 and Al_2Cu. Other phases are also possible, but were not detected.

5. Apart from its fracture mechanic and corrosion properties, the report allows for analytical prediction of both isothermal and non-isothermal lifetime of the joint. Both in regards to structural integrity and IMC growth. Any configuration of geometry and current can be created by using the data and analytical models provided by this report.

6. This report has found that the first iteration of HYB busbars have sufficient structural integrity and electrical properties to be applied as busbars. Further iterations might be able to improve on its defects and electrical analysis. HYB busbars demonstrated a proof of concept at a minimum.

Bibliography

[1] Jean Pierre Bergmann et al. 'Solid-state welding of aluminum to copper—case studies'. In: *Welding in the World* 57.4 (2013), pp. 541–550.

[2] Andrey Z Zhuk et al. 'Use of low-cost aluminum in electric energy production'. In: *Journal of Power Sources* 157.2 (2006), pp. 921–926.

[3] Shaohua Yang and Harold Knickle. 'Design and analysis of aluminum/air battery system for electric vehicles'. In: *Journal of power sources* 112.1 (2002), pp. 162–173.

[4] William E Veerkamp. 'Copper-to-aluminum transitions in high DC bus systems'. In: *IEEE transactions on industry applications* 33.4 (1997), pp. 1027–1034.

[5] B Ravisankar et al. 'Diffusion bonding of SU 263'. In: *Journal of materials processing technology* 209.4 (2009), pp. 2135–2144.

[6] Jiahu Ouyang, Eswar Yarrapareddy and Radovan Kovacevic. 'Microstructural evolution in the friction stir welded 6061 aluminum alloy (T6-temper condition) to copper'. In: *Journal of Materials Processing Technology* 172.1 (2006), pp. 110–122.

[7] Kwang Seok Lee and KWON Yong-Nam. 'Solid-state bonding between Al and Cu by vacuum hot pressing'. In: *Transactions of Nonferrous Metals Society of China* 23.2 (2013), pp. 341–346.

[8] Chih-Yuan Chen, Hao-Long Chen and Weng-Sing Hwang. 'Influence of interfacial structure development on the fracture mechanism and bond strength of aluminum/copper bimetal plate'. In: *Materials transactions* 47.4 (2006), pp. 1232–1239.

[9] Peder Sørlie Rustad. 'A report on the hybrid metal extrusion bondingand other cold state welding methods with focus onaluminum to copper bonding'. Trondheim, Norway: Norwegian University of Science and Technology, 2020.

[10] Lise Sandnes et al. 'Exploring the hybrid metal extrusion and bonding process for butt welding of Al–Mg–Si alloys'. In: *The International Journal of Advanced Manufacturing Technology* 98.5-8 (2018), pp. 1059–1065.

[11] Filippo Berto et al. 'Using the hybrid metal extrusion & bonding (HYB) process for dissimilar joining of AA6082-T6 and S355'. In: *Procedia Structural Integrity* 13 (2018), pp. 249–254.

[12] Tina Bergh et al. 'Microstructural and mechanical characterisation of a second generation hybrid metal extrusion & bonding aluminium-steel butt joint'. In: *Materials Characterization* (2020), p. 110761.

[13] Ø Grong and T Austigard. 'Documentation report on the butt-welded Al-Cu busbars produced by HyBond'. In: (2020).

[14] Telmo G Santos, RM Miranda and Pedro Vilaça. 'Friction stir welding assisted by electrical Joule effect'. In: *Journal of Materials Processing Technology* 214.10 (2014), pp. 2127–2133.

[15] S Schlegel et al. 'Joint resistance of bolted copper-copper busbar joints depending on joint force at temperatures beyond 105 C'. In: *2010 Proceedings of the 56th IEEE Holm Conference on Electrical Contacts*. IEEE. 2010, pp. 1–8.

[16] YJ Bao et al. 'The study on the busbar system and its fault analysis'. In: *2013 5th International Conference on Power Electronics Systems and Applications (PESA)*. IEEE. 2013, pp. 1–7.

[17] Swapnil Jain. 'Emerging trends in battery technology'. In: *Auto Tech Review* 6.1 (2017), pp. 52–55.

[18] Sandra Wappelhorst et al. 'Analyzing policies to grow the electric vehicle market in European cities'. In: *International Council on Clean Transportation* (2020).

[19] Alex Mak. 'Corrosion of Steel, Aluminum and Copper in Electrical Applications'. In: *General cable* 770 (2002).

[20] Tian-Guo Zhou et al. 'A method to produce aluminum alloy tube busbars by continuous casting-expansion extrusion'. In: *Journal of Materials Processing Technology* 177.1-3 (2006), pp. 163–166.

[21] P Eslami, A Karimi Taheri and M Zebardast. 'A comparison between cold-welded and diffusion-bonded Al/Cu bimetallic rods produced by ECAE process'. In: *Journal of materials engineering and performance* 22.10 (2013), pp. 3014–3023.

[22] Øystein Grong, Lise Sandnes and Filippo Berto. 'A status report on the hybrid metal extrusion & bonding (HYB) process and its applications'. In: *Material Design & Processing Communications* 1.2 (2019), e41.

[23] Øyvind Frigaard, Øystein Grong and OT Midling. 'A process model for friction stir welding of age hardening aluminum alloys'. In: *Metallurgical and materials transactions A* 32.5 (2001), pp. 1189–1200.

[24] M Yu Murashkin et al. 'Enhanced mechanical properties and electrical conductivity in ultrafine-grained Al alloy processed via ECAP-PC'. In: *Journal of Materials Science* 48.13 (2013), pp. 4501–4509.

[25] Maxim Murashkin et al. 'Enhanced mechanical properties and electrical conductivity in ultrafine-grained Al 6101 alloy processed via ECAP-conform'. In: *Metals* 5.4 (2015), pp. 2148–2164.

[26] X Sauvage et al. 'Optimization of electrical conductivity and strength combination by structure design at the nanoscale in Al–Mg–Si alloys'. In: *Acta Materialia* 98 (2015), pp. 355–366.

[27] Jonas K Sunde et al. 'On the microstructural origins of improvements in conductivity by heavy deformation and ageing of Al-Mg-Si alloy 6101'. In: *Materials Characterization* (2021), p. 111073.

[28] Jonas Vestfjell Jakobsen. 'Microstructure and mechanical properties of welded AA6082 Aluminium alloys'. MA thesis. NTNU, 2016.

[29] Hursanay Turgun. 'Electron Microscopy Characterization of Aluminium-Copper-Titanium-Steel Joint made using the Hybrid Metal Extrusion Bonding Method'. MA thesis. Trondheim, Norway: Norwegian University of Science and Technology, 2020.

[30] James E Parks. 'Ohms Law III Resistors in Series and Parallel'. In: *Department of Physics and Anatomy, University of Tennessee* (2007).

[31] R Brandt and G Neuer. 'Electrical resistivity and thermal conductivity of pure aluminum and aluminum alloys up to and above the melting temperature'. In: *International Journal of Thermophysics* 28.5 (2007), pp. 1429–1446.

[32] Richard Allen Matula. 'Electrical resistivity of copper, gold, palladium, and silver'. In: *Journal of Physical and Chemical Reference Data* 8.4 (1979), pp. 1147–1298.

[33] Raymond A Serway and John W Jewett. *Principles of physics*. Vol. 1. Saunders College Pub. Fort Worth, TX, 1998.

[34] Uday A Bakshi. *Basic electrical engineering*. Technical Publications, 2020.

[35] Dagur Ólafsson, Pedro Vilaça and Jussi Vesanko. 'Multiphysical characterization of FSW of aluminum electrical busbars with copper ends'. In: *Welding in the World* 64.1 (2020), pp. 59–71.

[36] Linda Ager-Wick Ellingsen et al. 'Life cycle assessment of a lithium-ion battery vehicle pack'. In: *Journal of Industrial Ecology* 18.1 (2014), pp. 113–124.

[37] James B Friauf. 'The crystal structures of two intermetallic compounds'. In: *Journal of the American Chemical Society* 49.12 (1927), pp. 3107–3114.

[38] Paras Dubey and Netram Kaurav. 'Stoichiometric and Nonstoichiometric Compounds'. In: *Structure Processing Properties Relationships in Stoichiometric and Nonstoichiometric Oxides*. IntechOpen, 2019.

[39] Norman S Stoloff and Vinod K Sikka. *Physical metallurgy and processing of intermetallic compounds*. Springer Science & Business Media, 2012.

[40] Milenko Braunovic and N Aleksandrov. 'Effect of electrical current on the morphology and kinetics of formation of intermetallic phases in bimetallic aluminum-copper joints'. In: *Proceedings of IEEE Holm Conference on Electrical Contacts*. IEEE. 1993, pp. 261–268.

[41] Won-Bae Lee, Kuek-Saeng Bang and Seung-Boo Jung. 'Effects of intermetallic compound on the electrical and mechanical properties of friction welded Cu/Al bimetallic joints during annealing'. In: *Journal of Alloys and Compounds* 390.1-2 (2005), pp. 212–219.

[42] M Abbasi, A Karimi Taheri and MT Salehi. 'Growth rate of intermetallic compounds in Al/Cu bimetal produced by cold roll welding process'. In: *Journal of Alloys and Compounds* 319.1-2 (2001), pp. 233–241.

[43] Ji L Murray. 'The aluminium-copper system'. In: *International metals reviews* 30.1 (1985), pp. 211–234.

[44] Norbert Ponweiser, Christian L Lengauer and Klaus W Richter. 'Re-investigation of phase equilibria in the system Al–Cu and structural analysis of the high-temperature phase η1-Al1-δCu'. In: *Intermetallics* 19.11 (2011), pp. 1737–1746.

[45] Yu-chang Su et al. 'Thermodynamic analysis and experimental research on Li intercalation reactions of the intermetallic compound Al2Cu'. In: *Solid State Ionics* 177.5-6 (2006), pp. 507–513.

[46] EH Kisi and JD Browne. 'Ordering and structural vacancies in non-stoichiometric Cu–Al γ brasses'. In: *Acta Crystallographica Section B: Structural Science* 47.6 (1991), pp. 835–843.

[47] LARS Arnberg and SVEN Westman. 'Crystal perfection in a noncentrosymmetric alloy. Refinement and test of twinning of the γ-Cu9Al4 structure'. In: *Acta Crystallographica Section A: Crystal Physics, Diffraction, Theoretical and General Crystallography* 34.3 (1978), pp. 399–404.

[48] FA Calvo et al. 'Special features of the formation of the diffusion bonded joints between copper and aluminium'. In: *Journal of materials science* 23.6 (1988), pp. 2273–2280.

[49] Chih-Yuan Chen and Weng-Sing Hwang. 'Effect of annealing on the interfacial structure of aluminum-copper joints'. In: *Materials transactions* (2007), pp. 0706110009–0706110009.

[50] Sansan Ao et al. 'Microstructure evolution and mechanical properties of Al/Cu ultrasonic spot welded joints during thermal processing'. In: *Journal of Manufacturing Processes* 41 (2019), pp. 307–314.

[51] Rainer Pelzer et al. 'Growth behavior and physical response of Al-Cu intermetallic compounds'. In: *2014 IEEE 16th Electronics Packaging Technology Conference (EPTC)*. IEEE. 2014, pp. 372–377.

[52] Evgeny T Moiseenko, Roman R Altunin and Sergey M Zharkov. 'In situ electron diffraction and resistivity characterization of solid state reaction process in Cu/Al bilayer thin films'. In: *Metallurgical and Materials Transactions A* 51.3 (2020), pp. 1428–1436.

[53] Stephanie Pfeifer et al. 'Characterization of intermetallic compounds in Al-Cu-Bimetallic interfaces'. In: *2012 IEEE 58th Holm Conference on Electrical Contacts (Holm)*. IEEE. 2012, pp. 1–6.

[54] F d'Heurle et al. '2.22 The deposition by evaporation of Cu Al alloy films'. In: *Vacuum* 27.4 (1977), pp. 321–327.

[55] C Macchioni et al. 'Low temperature resistivity of thin film and bulk samples of CuAl2 and Cu9Al4'. In: *Thin Solid Films* 81.1 (1981), pp. 71–78.

[56] Jerry Janesch. 'Two-wire vs. four-wire resistance measurements: Which configuration makes sense for your application'. In: *no. May* (2013), pp. 2–4.

[57] Helmut Mehrer. 'Diffusion in intermetallics'. In: *Materials Transactions, JIM* 37.6 (1996), pp. 1259–1280.

[58] Yasuhiro Shiraki and Noritaka Usami. *Silicon-germanium (SiGe) nanostructures: Production, properties and applications in electronics*. Elsevier, 2011.

[59] *Diffusion Interdiffusion: In an alloy, atoms tend to migrate from regions of high concentration to regions of low concentration. Initially After some. - ppt video online download*. Oct. 2017. URL: https://slideplayer.com/slide/5320568/.

[60] Michael Pfeifer. *Materials enabled designs: The materials engineering perspective to product design and manufacturing*. Butterworth-Heinemann, 2009.

[61] HA Das. ‘Application of steady state diffusion in waste containment and related radiotracer measurements’. In: *Journal of Environmental Science & Health Part A* 29.9 (1994), pp. 1843–1857.

[62] Donald R Askeland. ‘Atom Movement in Materials’. In: *The Science and Engineering of Materials*. Springer, 1996, pp. 111–137.

[63] Aixia Mao et al. ‘The diffusion behaviors at the Cu-Al solid-liquid interface: A molecular dynamics study’. In: *Results in Physics* 16 (2020), p. 102998.

[64] Lars Buitinck et al. ‘API design for machine learning software: experiences from the scikit-learn project’. In: *ECML PKDD Workshop: Languages for Data Mining and Machine Learning*. 2013, pp. 108–122.

[65] David R Poirier and G Geiger. *Transport phenomena in materials processing*. Springer, 2016.

[66] Carl I Steefel and Kate Maher. ‘Fluid-rock interaction: A reactive transport approach’. In: *Reviews in mineralogy and geochemistry* 70.1 (2009), pp. 485–532.

[67] Helmut Mehrer. ‘Interdiffusion and Kirkendall effect’. In: *Diffusion in solids: fundamentals, methods, materials, diffusion-controlled processes* (2007), pp. 161–177.

[68] Aloke Paul. ‘The Kirkendall effect in solid state diffusion’. In: *Technische Universiteit Eindhoven* (2004).

[69] John Wyrill Christian. *The theory of transformations in metals and alloys*. Newnes, 2002.

[70] Øystein Grong et al. ‘An analytical framework for modelling intermetallic compound (IMC) formation and optimising bond strength in aluminium-steel welds’. In: *Material Design & Processing Communications* 1.3 (2019), e57.

[71] Chien-Pan Liu et al. ‘Cu-Al interfacial formation and kinetic growth behavior during HTS reliability test’. In: *Journal of Materials Processing Technology* 267 (2019), pp. 90–102.

[72] Hyoung-Joon Kim et al. ‘Effects of Cu/Al intermetallic compound (IMC) on copper wire and aluminum pad bondability’. In: *IEEE Transactions on Components and Packaging Technologies* 26.2 (2003), pp. 367–374.

[73] Vikas Jindal et al. ‘Reactive diffusion in the roll bonded iron–aluminum system’. In: *Materials letters* 60.13-14 (2006), pp. 1758–1761.

[74] Øystein Grong and HR Shercliff. ‘Microstructural modelling in metals processing’. In: *Progress in materials science* 47.2 (2002), pp. 163–282.

[75] M Braunovic and N Aleksandrov. ‘Intermetallic compounds at aluminum-to-copper and copper-to-tin electrical interfaces’. In: *Proceedings of the Thirty-Eighth IEEE Holm Conference on Electrical Contacts*. 1992, pp. 25–34.

[76] Hui Xu et al. ‘Growth of intermetallic compounds in thermosonic copper wire bonding on aluminum metallization’. In: *Journal of Electronic materials* 39.1 (2010), pp. 124–131.

[77] Hao Dong, Ling-Dong Sun and Chun-Hua Yan. ‘Upconversion emission studies of single particles’. In: *Nano Today* 35 (2020), p. 100956.

[78] Joseph I Goldstein et al. *Scanning electron microscopy and X-ray microanalysis*. Springer, 2017.

[79] Ludwig Reimer. *Transmission electron microscopy: physics of image formation and microanalysis*. Vol. 36. Springer, 2013.

[80] Daisuke TSURUMI et al. ‘Automating FIB Sample Preparation to Improve STEM Throughput’. In: *SEI TECHNICAL REVIEW* 89 (2019), p. 57.

[81] Geoffrey E Lloyd. ‘Atomic number and crystallographic contrast images with the SEM: a review of backscattered electron techniques’. In: *Mineralogical Magazine* 51.359 (1987), pp. 3–19.

Appendix

A Busbar specifications

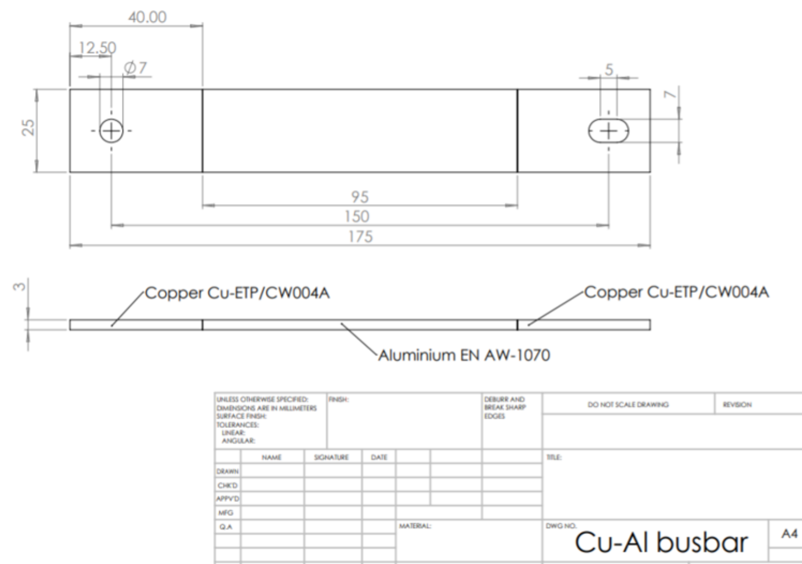

Machine drawing

B Temperature increase code

```
"""
Created Mars 06 2020

@author Peder Rustad
"""

import numpy as np
import matplotlib.pyplot as plt
import matplotlib.animation as animation
import matplotlib as style
T_0 = 20

c_al = 887 #J/kgK, heat capacity of aluminum at 20
rho1 = 3.03*10**-8#Ohm*m aluminum resistivity
height = 0.003 #meter height cross section
L = 0.2
g_al = 2700 #kg/m^3
alpha_al = 0.004308 # per degree celcius, Temperature Coefficients of Resistance

c_cu = 385 #J/kgK, heat capacity of copper at 20
rho2 = 1.72*10**-8# copper resistivity
g_cu = 8940 #kg/m^3
alpha_cu = 0.004041 # per degree celcius, Temperature Coefficients of Resistance


def resistance_function_al(I, width):
    A = height * width
    m_al = width * height * L * g_al # mass of aluminum
```

```
    R1 = rho1 * L / A # resistance Al at 20 C
    R = R1
    C_al = c_al * m_al #assumes bulk is aluminum when calculating temperature
    V = I * R
    dT = 0

    temperature_list_al = []
    energy_list_al = []
    resistance_list_al =[]
    voltage_list_al = []
    time_list_al = []

    for i in np.arange(0, 1000, 1):
        E = (V**2 / R) * (i) #increase in energy
        dT = E / C_al #increase in temperature each second
        T = dT + T_0 #total increase in temperature each second
        R = (R1) * (1 + alpha_al * (T - T_0)) #increase in resistance because of the temperature
        V = I * R    #increase in Voltage drop because of the increase in resistanc
        temperature_list_al.append(T)
        resistance_list_al.append(R)
        voltage_list_al.append(V)
        time_list_al.append(i)


        # print (i, E, R, T, V)
            #plt.plot(time_list, temperature_list, label='Temperature')


    return temperature_list_al, resistance_list_al


Result_5A_1mm_al = resistance_function_al(100, 0.0828)
Result_5A_2mm_al = resistance_function_al(5, 0.002)
Result_5A_3mm_al = resistance_function_al(5, 0.003)
Result_5A_4mm_al = resistance_function_al(5, 0.004)
Result_5A_5mm_al = resistance_function_al(5, 0.005)


T_5A_1mm_al = Result_5A_1mm_al[0]
T_5A_2mm_al = Result_5A_2mm_al[0]
T_5A_3mm_al = Result_5A_3mm_al[0]
T_5A_4mm_al = Result_5A_4mm_al[0]
T_5A_5mm_al = Result_5A_5mm_al[0]

R_5A_1mm_al = Result_5A_1mm_al[1]
R_5A_2mm_al = Result_5A_2mm_al[1]
R_5A_3mm_al = Result_5A_3mm_al[1]
R_5A_4mm_al = Result_5A_4mm_al[1]
R_5A_5mm_al = Result_5A_5mm_al[1]

# plt.plot(R_5A_1mm_al, label = '5A, 75mm^2, Aluminum')

plt.plot(T_5A_1mm_al, label = '100A, 248.33mm^2, Aluminum')

def resistance_function_cu(I, width):
    A = height * width

    m_cu = width * height * L * g_cu # if al volume = cu volume
```

```
    R2 = rho2 * L / A #resistance Cu
    R = R2 # start resistance at 20 C
    C_cu = c_cu * m_cu  #assumes bulk is aluminum when calculating temperature
    V = I * R
    dT = 0
    temperature_list_cu = []
    energy_list_cu = []
    resistance_list_cu =[]
    voltage_list_cu = []
    time_list_cu = []

    for i in np.arange(0, 1000, 1):
        E = (V**2 / R) * (i) #increase in energy
        dT = E / C_cu #increase in temperature each second
        T = dT + T_0 #total increase in temperature each second
        # R = (R2) * (1 + alpha_cu * (T - T_0)) #increase in resistance because of the temperature
        V = I * R    #increase in V oltage drop because of the increase in resistanc
        temperature_list_cu.append(T)
        resistance_list_cu.append(R)
        voltage_list_cu.append(V)
        time_list_cu.append(i)


        # print (i, E, R, T, V)
            #plt.plot(time_list, temperature_list, label='Temperature')


    return temperature_list_cu, resistance_list_cu


Result_5A_1mm_cu = resistance_function_cu(100, 0.025)
Result_5A_2mm_cu = resistance_function_cu(5, 0.002)
Result_5A_3mm_cu = resistance_function_cu(5, 0.003)
Result_5A_4mm_cu = resistance_function_cu(5, 0.004)
Result_5A_5mm_cu = resistance_function_cu(5, 0.005)


T_5A_1mm_cu = Result_5A_1mm_cu[0]
T_5A_2mm_cu = Result_5A_2mm_cu[0]
T_5A_3mm_cu = Result_5A_3mm_cu[0]
T_5A_4mm_cu = Result_5A_4mm_cu[0]
T_5A_5mm_cu = Result_5A_5mm_cu[0]

R_5A_1mm_cu = Result_5A_1mm_cu[1]
R_5A_2mm_cu = Result_5A_2mm_cu[1]
R_5A_3mm_cu = Result_5A_3mm_cu[1]
R_5A_4mm_cu = Result_5A_4mm_cu[1]
R_5A_5mm_cu = Result_5A_5mm_cu[1]

# plt.plot(R_5A_1mm_cu, label = '5A, 75mm^2, Copper')
plt.plot(T_5A_1mm_cu, label = '100A, 75mm^2, Copper')
plt.grid('both')
plt.xlabel('Time [s]')
plt.ylabel('Temperature [C]')
plt.title('Temperature per second')
plt.legend()
plt.show()
```

C Error function plotter

```
"""
Created April 02 2020

@author Peder Rustad
"""
import numpy as np
import matplotlib.pyplot as plt
import matplotlib.animation as animation
import matplotlib as style
from scipy import special
import math

dx = 0.01

x = np.arange(-1,1.1, dx)
C_1 = np.zeros(len(x))
C_2 = np.zeros(len(x))
C_3 = np.zeros(len(x))
C_4 = np.zeros(len(x))
C_0 = 1
t_1 = 0
t_2 = 0.01
t_3 = 0.1
t_4 = 0.4
D = 0.1
def concentration():
    for i in range(len(x)):

        C_1[i] =(C_0 / 2) * (1 - special.erf(x[i] / (2 * math.sqrt(D * t_1))))
        C_2[i] =(C_0 / 2) * (1 - special.erf(x[i] / (2 * math.sqrt(D * t_2))))
        C_3[i] =(C_0 / 2) * (1 - special.erf(x[i] / (2 * math.sqrt(D * t_3))))
        C_4[i] =(C_0 / 2) * (1 - special.erf(x[i] / (2 * math.sqrt(D * t_4))))


    return C_1, C_2, C_3, C_4

C = concentration()
C_1 = C[0]
C_2 = C[1]
C_3 = C[2]
C_4 = C[3]



plt.plot(x, C_1, label = 't = 0', color ='blue')
plt.plot(x, C_2, label = 't = 0.01', color = 'orange')
plt.plot(x, C_3, label = 't = 0.1', color = 'green')
plt.plot(x, C_4, label = 't = 0.4', color = 'red')
plt.xlabel('Position [x]')
plt.ylabel('Concetration [C]')
plt.legend()
plt.show()
```

D Diffusion Coefficient

```
"""
Created March 08 2020

@author Peder Rustad
"""
import numpy as np
from sklearn.linear_model import LinearRegression
import matplotlib.pyplot as plt
import matplotlib.animation as animation
import matplotlib as style
import math
R = 8.3145 # J/molK
#Cu-Al interfacial formation and kinetic growth behavior during HTS reliability test
T_1 = 423 #150c
T_2 = 473 #200c
T_3 = 523 #250c

K_1 = 2.09e-20 #150c
K_2 = 1.38e-19 #200c
K_3 = 1.35e-18 #250c
T = np.zeros(3)
D = np.log(np.array([K_3, K_2, K_1]))

T = 1000 / np.array([T_3, T_2, T_1])

T_increasing = np.array([T_1, T_2])

T_increasing = T_increasing.reshape(-1,1)
T = T.reshape(-1,1)
model = LinearRegression()
model.fit(T, D)
D_predict = model.predict(T)

a = model.coef_
b = model.intercept_
print(a)
print(b)

def diffusion():
    T_d = np.arange(600, 400, -10) # temperature [K]


    ln_d2 = np.zeros(len(T_d))
    ln_d = np.zeros(len(T_d))
    d = np.zeros(len(T_d))
    D_0 = math.exp(b) # pre-exponential diffusion coefficient [m^2]
    Q_d = - a * 1000 * R # activation energy [J/mol]
    for i in range(len(T_d)):


        ln_d[i] = (a * 1000 / T_d[i]) + b

        ln_d2[i] = np.log(D_0 * math.exp(- Q_d / (R * T_d[i])))

        d[i] = D_0 * math.exp(-Q_d / (R * T_d[i]))
```

```
    return T_d, ln_d, ln_d2, d, D_0, Q_d

diffusion = diffusion()

T_d = diffusion[0]

ln_d = diffusion[1]
ln_d2 = diffusion[2]
d = diffusion[3]
D_0 = diffusion[4]
Q_d = diffusion[5]

print('Q_d = ', Q_d, 'D_0 = ', D_0)
print('D = ', D_0, 'e^(-', Q_d, '/ (RT))')
print('linear formula = ', a, 'x + ', b)

# plt.plot(T_d, d, label = 'diffusion coefficient Al', color = 'blue')
# plt.xlabel('Temperature [K]')
# plt.ylabel('D [m^2]')

# plt.scatter(1000 / T_d, ln_d2, label = 'extended', color = 'blue')
plt.scatter(T, D, label = 'Experimental k', color = 'orange')
plt.plot(T, D_predict, label = 'Linear regression k', color='red')
plt.xlabel('1000 / Temperature [1/K]')
plt.ylabel('ln k')
plt.title('Interdiffusion coefficient per temperature')
plt.legend()
plt.show()
```

E Isothermal IMC growth model

```
"""
Created April 10 2020

@author Peder Rustad
"""
import numpy as np
import matplotlib.pyplot as plt
import matplotlib.animation as animation
import matplotlib as style
import math


R = 8.3145 # J/molK
dt = 1000 # Change in time
t = np.arange(0, 1260000, dt) # Time interval
T = 523 # Heat temperature in Kelvin

X_1 = np.zeros(len(t))
X_2 = np.zeros(len(t))
X_3 = np.zeros(len(t))
X_4 = np.zeros(len(t))

def k_1(T):
    k_1 = 3.8317733237294375e-11 * math.exp(- (50457.58568285) / (R*T)) #Braunovic
    return k_1
```

```
def k_2(T):
    k_2 =  1.0425982343536876e-07 * math.exp(- (96505.3784729) / (R*T)) #Xu
    return k_2
def k_3(T):
    k_3 = 4.6553511407603024e-07 * math.exp(- (108470.52246742) / (R*T)) #Kim
    return k_3
def k_4(T):
    k_4 = 4.64711e-11 * math.exp(-76130.235 / (T*R)) #liu
    return k_4



k_1 = k_1(523)
k_2 = k_2(523)
k_3 = k_3(523)
k_4 = k_4(523)

def IMC_thickness():


    for i in range(len(t)):
        X_1[i] = 1e6 * math.sqrt(t[i] * k_1)
        X_2[i] = 1e6 * math.sqrt(t[i] * k_2)
        X_3[i] = 1e6 * math.sqrt(t[i] * k_3)
        X_4[i] = 1e6 * math.sqrt(t[i] * k_4)

    return X_1, X_2, X_3, X_4

X = IMC_thickness()
X_1 = X[0]
X_2 = X[1]
X_3 = X[2]
X_4 = X[3]

plt.plot(t, X_1, label = '523 K, Braunovic', color = 'blue')
plt.plot(t, X_2, label = '523 K, Xu', color = 'orange')
plt.plot(t, X_3, label = '523 K, Kim', color = 'green')
plt.plot(t, X_4, label = '523 K, Liu', color = 'red')
plt.xlabel('Time [s]')
plt.ylabel('Thickness [m]')
plt.title('IMC thickness prediction')
plt.legend()
plt.show()
```

F Isokinetic growth model

```
"""
Created April 10 2021

@author Peder Rustad
"""
import numpy as np
import matplotlib.pyplot as plt
import math


dt = 0.1
```

```
k_0 = 4.643927706182987e-12 # m^2/s, pre exponential diffusion coeffisient
Q_d = 76.797490640785 # kJ/mol, activation energy
x_0 = 0 #initial thickness
R = 8.314 # gas constant J/mol-K
T_r = 200 # chosen referance temperature in celcius
t_r = 1800000 # chosen referance time
k_p_ref = k_0 * math.exp(-Q_d * 1000 / (8.314 * (T_r + 273))) # m^2/s, Diffusion coefficient incre
Y_r = math.sqrt(2 * k_p_ref * t_r)

t = np.arange(0, 100, dt)
T = np.zeros(len(t)) #Temperature
k_p = np.zeros(len(t))
t_s = np.zeros(len(t))
T_average = np.zeros(len(t))
sum_tid = np.zeros(len(t)) # what is this
Y = np.zeros(len(t))
def growth_function():

    for i in range(len(t)):
        if i == 0:
            T[i] = 0

        else:
            T[i] = 20 + (1200 / math.sqrt(t[i])) * math.exp(-1 / t[i])

        T_average[i] = (T[i] + T[i-1]) / 2 #average time
        k_p[i] = k_0 * math.exp(-Q_d * 1000 / (R*(T_average[i] + 273))) #k
        t_s[i] = t_r * k_p_ref / k_p[i]
        sum_tid[i] = (1 / t_s[i]) * dt + sum_tid[i-1]
        Y[i] = Y_r * math.sqrt(sum_tid[i])


    print (k_p, t_s, sum_tid, Y, Y_r,)
    # plt.plot(T)
    #plt.plot(T_average, color = 'blue')
    plt.plot(Y, color = 'purple')
    plt.xlabel('Time [s]')
    plt.ylabel('IMC growth [m]')
    plt.show()

growth_function()
```

G Calculate interdiffusion coefficient from experimental data

```
"""
Created May 12 2021

@author Peder Rustad
"""
import numpy as np
import matplotlib.pyplot as plt
from scipy.optimize import curve_fit
x_0 = 0.2e-6
#250
x_10 = 0.86575e-6
x_18 = 1.198e-6
x_30 = 1.7875e-6
```

```
#200
x_48 = 0.8e-6

def func(x, a):
    return (a*x + x_0**2)**0.5

#250
# yData = np.array([x_10, x_18, x_30]) - x_0
# xData = np.array([864000, 1.555e6, 2.592e6])
#200
xData = np.array([4.147e6])
yData = np.array([x_48])

popt, pcov = curve_fit(func, xData, yData)
print(popt)
xFit = np.arange(0.0, 4.32e6, 20)



plt.plot(xFit, func(xFit, popt), 'r')

plt.plot(xData, yData, 'bo')


plt.show()
```

H Calculate the relationship between measured and average area

```
"""
Created june 10 2021

@author Peder Rustad
"""
import numpy as np
import matplotlib.pyplot as plt

y1 = np.array([ 1.035483609, #E1 measured area / average
                1.017079696,
                1.001432316,
                0.996243548,
                0.94976083
])


y2 = np.array([ 1.001030304, #E2 measured area / average
                1.016265125,
                1.004423958,
                0.996025274,
                0.98225534
])
y3 = np.array([ 0.988496617, #E3 measured area / average
                1.01459834,
                0.99339925,
                1.004354852,
                0.999150941
])
```

```
y0 = np.array([ 0.904910064, #E0 (Unheated) measured area / average
                0.998451895,
                1.028808867,
                1.039020307,
                1.028808867
])
x = np.array([0, 12.5, 25, 37.5, 50]) # Position of each measurement

def interpolation(y):
    a = np.zeros(len(x))
    b = np.zeros(len(x))
    for i in range(len(x)-1):
        a[i] = (y[i+1]-y[i]) / (x[i+1] - x[i]) #creating a in y = ax + b
        b[i] = y[i] - a[i] * x[i]#creating b in y = ax + b
    return a, b

a1, b1 = interpolation(y0)[0][0:4], interpolation(y0)[1][0:4] # change the y variable to get a plo

def d(x):
    x = np.array([0,12.5])
    d = a1[0] * x + b1[0]
    return plt.plot(x, d, label = 'y = %.4f x + %.4f' %(a1[0],b1[0]))

def d2(x):
    x = np.array([12.5,25])
    d2 = a1[1] * x + b1[1]
    return plt.plot(x, d2, label = 'y = %.4f x + %.4f' %(a1[1],b1[1]))


def d3(x):
    x = np.array([25,37.5])
    d3 = a1[2] * x + b1[2]
    return plt.plot(x, d3, label = 'y = %.4f x + %.4f' %(a1[2],b1[2]))

def d4(x):
    x = np.array([37.5,50])
    d4 = a1[3] * x + b1[3]
    return plt.plot(x, d4, label = 'y = %.4f x + %.4f' %(a1[3],b1[3]))

print (a1, b1)

d(x)
d2(x)
d3(x)
d4(x)
plt.legend()
plt.show()
```

I Hardness plots

	Test 1	Test 2	Test 3	Average	Standard	Error
-10	73.2	74.7	74.3	74.0666667	0.63420992	0.36616127
-9.5	74.3	73.2	73.5	73.6666667	0.46427961	0.26805196
-9	74.3	73.9	75	74.4	0.45460606	0.26246693
-8.5	73.2	73.8	74.3	73.7666667	0.44969125	0.25962937
-8	69.4	73.7	73.8	72.3	2.05101601	1.18415464
-7.5	69.8	70.4	75.2	71.8	2.41660919	1.39522997
-7	70.4	71.9	70.8	71.0333333	0.63420992	0.36616127
-6.5	68.9	70	70.4	69.7666667	0.63420992	0.36616127
-6	65.6	66.3	66.5	66.1333333	0.38586123	0.22277709
-5.5	61.6	66.4	64.2	64.0666667	1.96185853	1.13267955
-5	60.3	61.9	63.9	62.0333333	1.4727148	0.85027229
-4.5	60	62.2	62.9	61.7	1.23558353	0.71336449
-4	59.3	60.4	60.8	60.1666667	0.63420992	0.36616127
-3.5	57.2	57.6	59.5	58.1	1.0033278	0.57927157
-3	57.6	56.7	56.7	57	0.42426407	0.24494897
-2.5	57.5	58.4	57.6	57.8333333	0.4027682	0.23253833
-2	57.2	57.3	55.5	56.6666667	0.82596745	0.47687253
-1.5	55	56.5	53.5	55	1.22474487	0.70710678
-1	54.9	53.5	54.4	54.2666667	0.57927157	0.3344426
-0.5	53	52.9	51.3	52.4	0.7788881	0.44969125
0	52.2	53.9	51	52.3666667	1.18977122	0.68691473
0.5	52.8	53.6	53.9	53.4333333	0.46427961	0.26805196
1	53.6	53.6	54.1	53.7666667	0.23570226	0.13608276
1.5	65.7	62	73.4	67.0333333	4.74856704	2.74158646
2	68.3	72.7	71.3	70.7666667	1.83545332	1.05969947
2.5	71.1	73.9	71.6	72.2	1.21928941	0.70395707
3	71.1	71.8	72	71.6333333	0.38586123	0.22277709
3.5	112.5	110.5	117.7	113.566667	3.03461511	1.75203585
4	116.7	115.5	117.3	116.5	0.74833148	0.43204938
4.5	117.5	114.7	114.4	115.533333	1.39602611	0.80599605
5	117.4	114.5	113.5	115.133333	1.6539515	0.95490934
5.5	120.1	113.1	113.1	115.433333	3.29983165	1.90515869
6	115.6	118.3	116	116.633333	1.18977122	0.68691473
6.5	112.4	113.1	115.1	113.533333	1.14406682	0.66052729
7	110.5	111.5	112.5	111.5	0.81649658	0.47140452
7.5	108.9	112.3	109.9	110.366667	1.42672897	0.82372236
8	109.2	111.1	108.4	109.566667	1.13235252	0.65376403
8.5	107.7	108.9	107.9	108.166667	0.52493386	0.3030707
9	106.9	109.8	108	108.233333	1.19536141	0.69014223
9.5	107.7	109.8	107.4	108.3	1.06770783	0.6164414
10	108.1	108.1	107	107.733333	0.51854497	0.29938208

Hardness values with standard deviation and error.

J TEM EDX

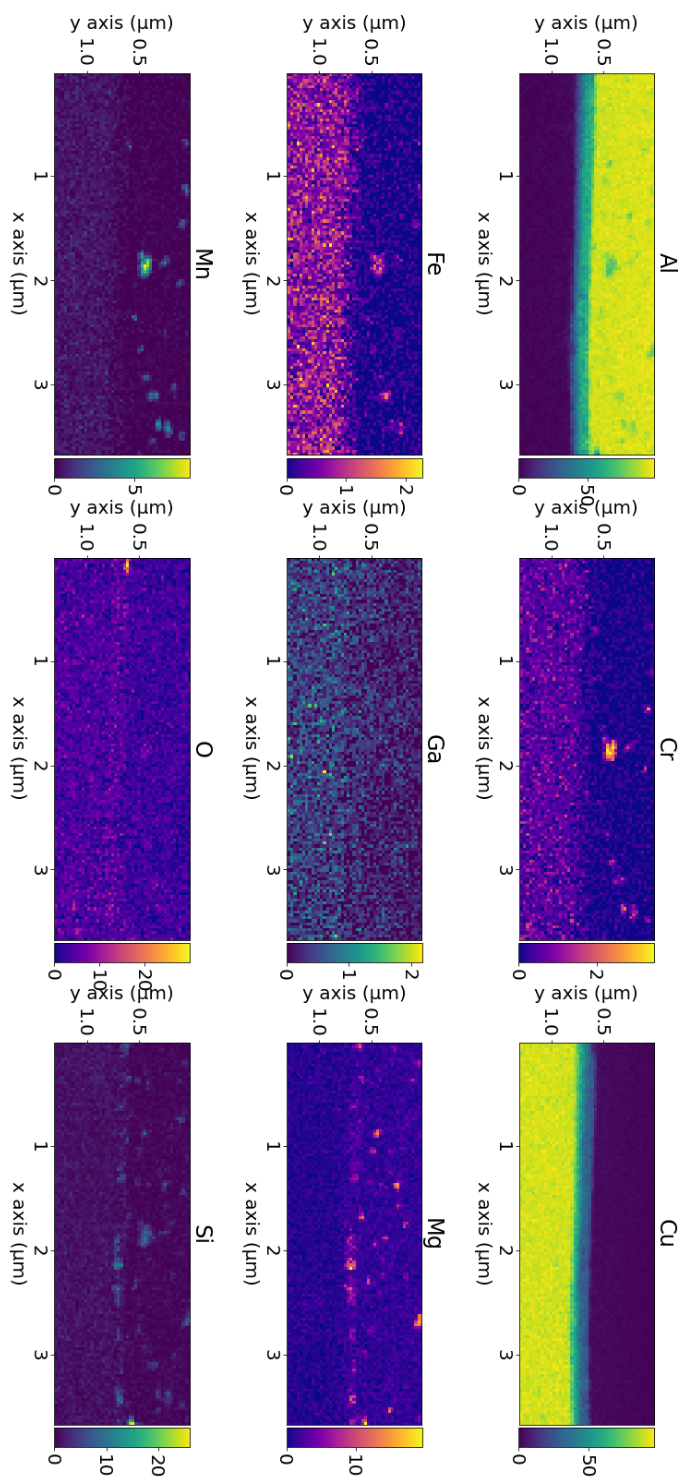

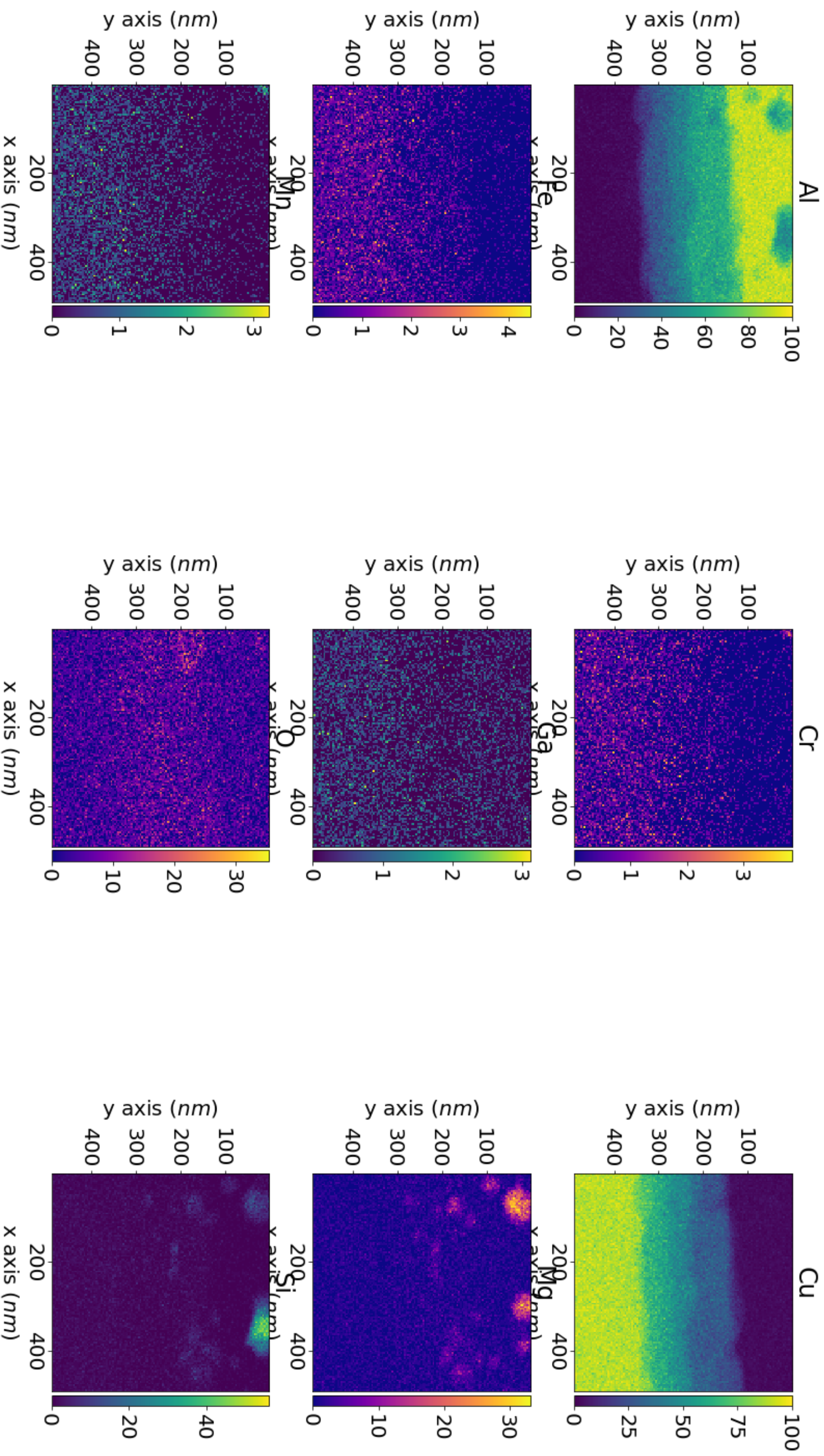

atomic percent of
Al
Cr
Cu
Fe
Ga
Mg
Mn
O
Si
y axis (nm)
x axis (nm)

K Distance from interface to wires

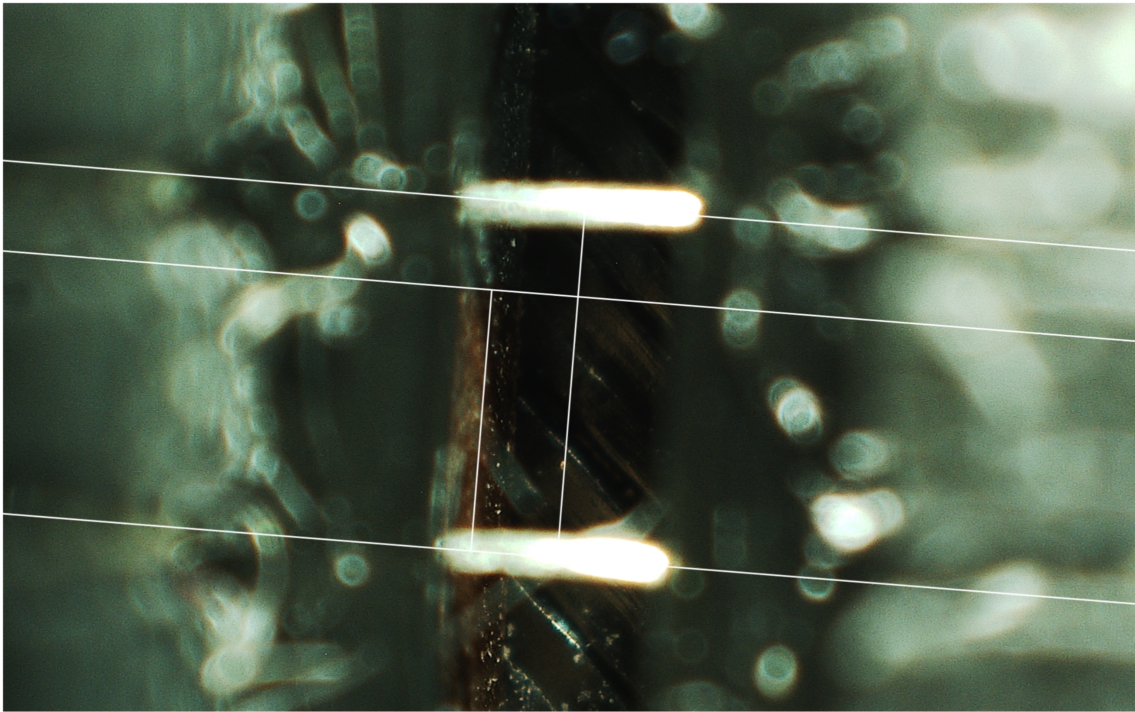

E0 sample

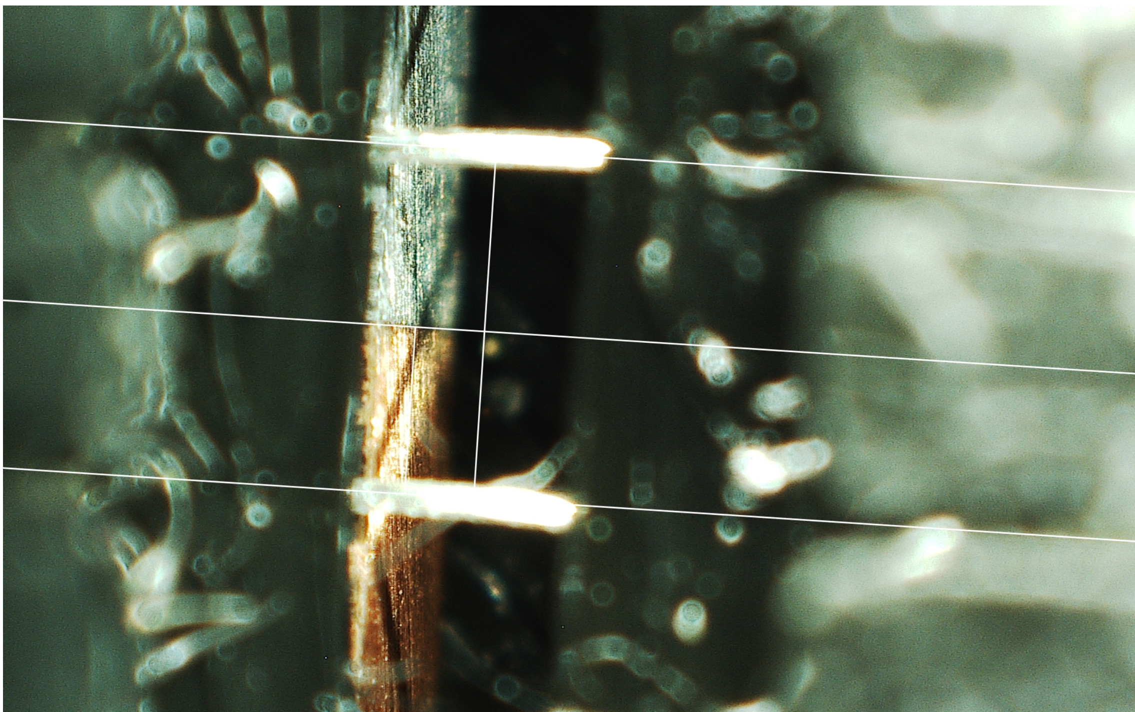

E1 sample

E2 sample

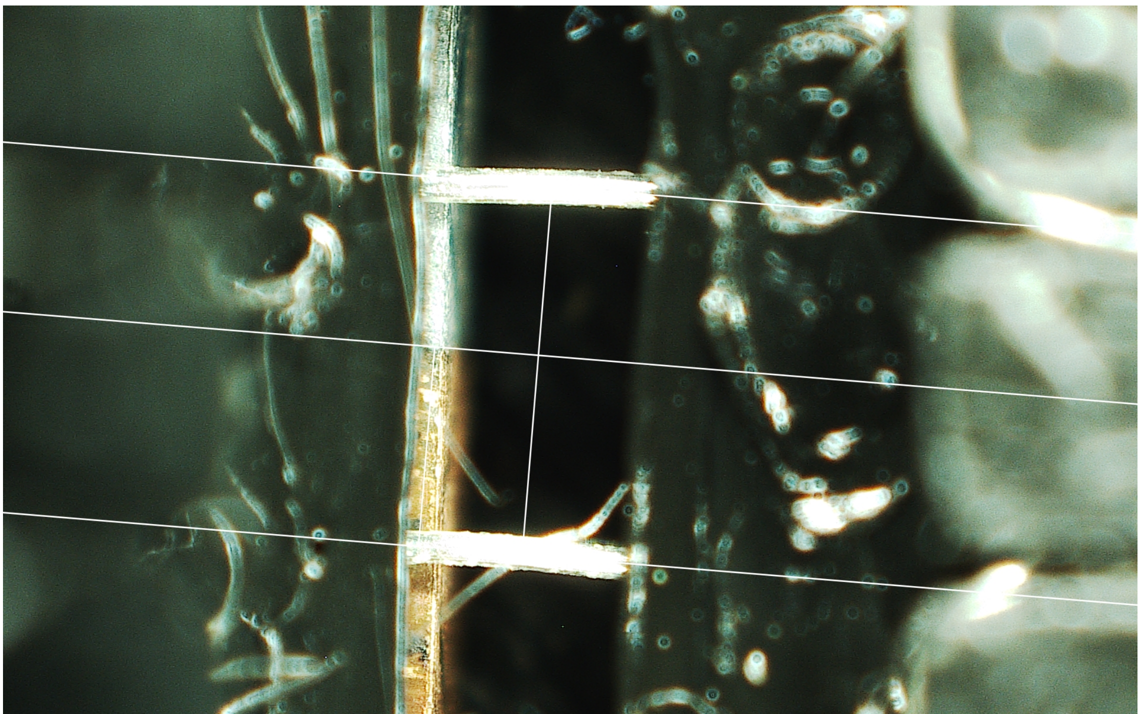

E3 sample

L SEM EDX analysis

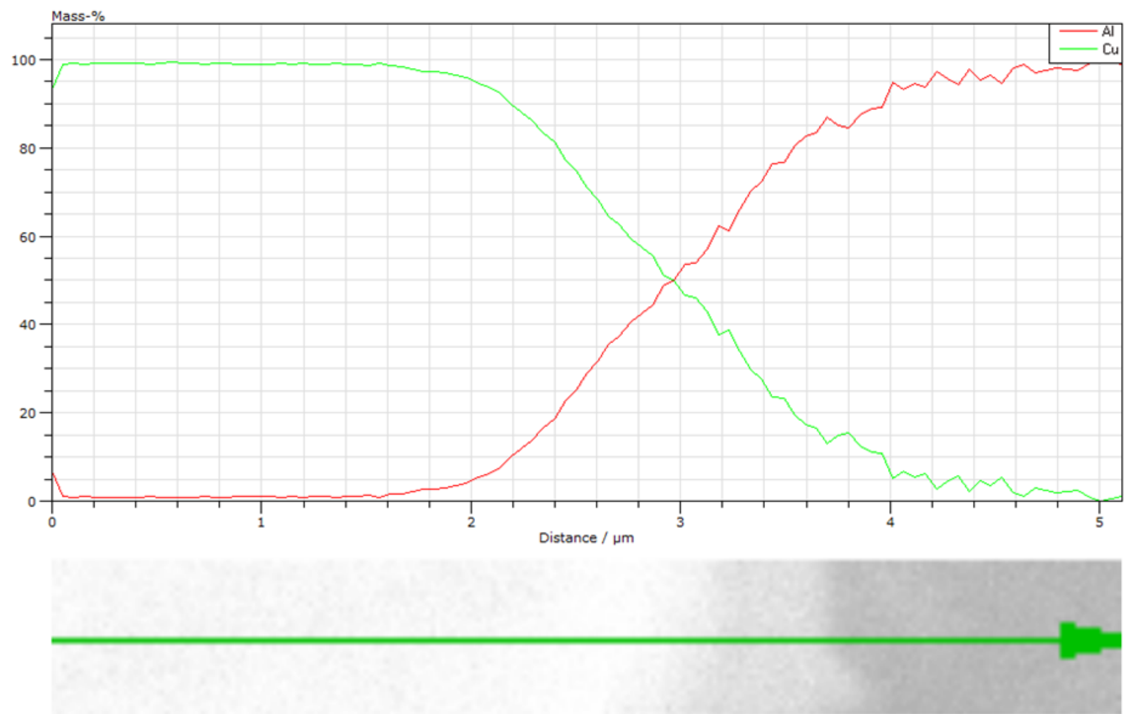

200 °C Heated EDX

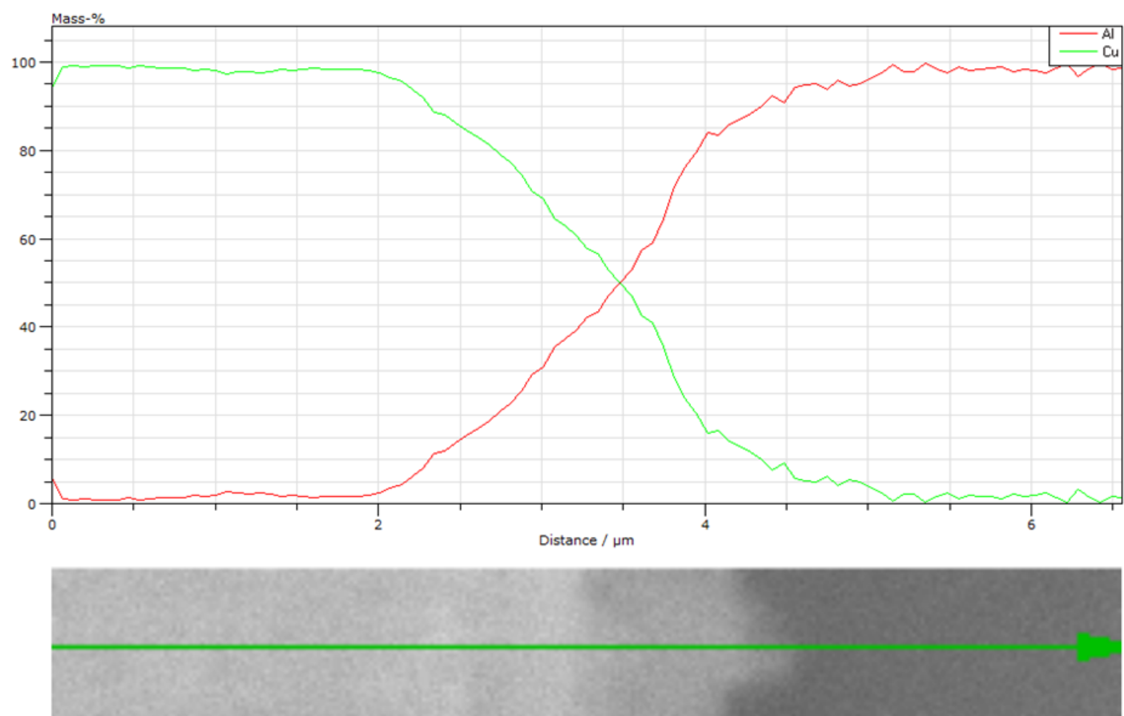

250 °C Heated EDX for 242 hours

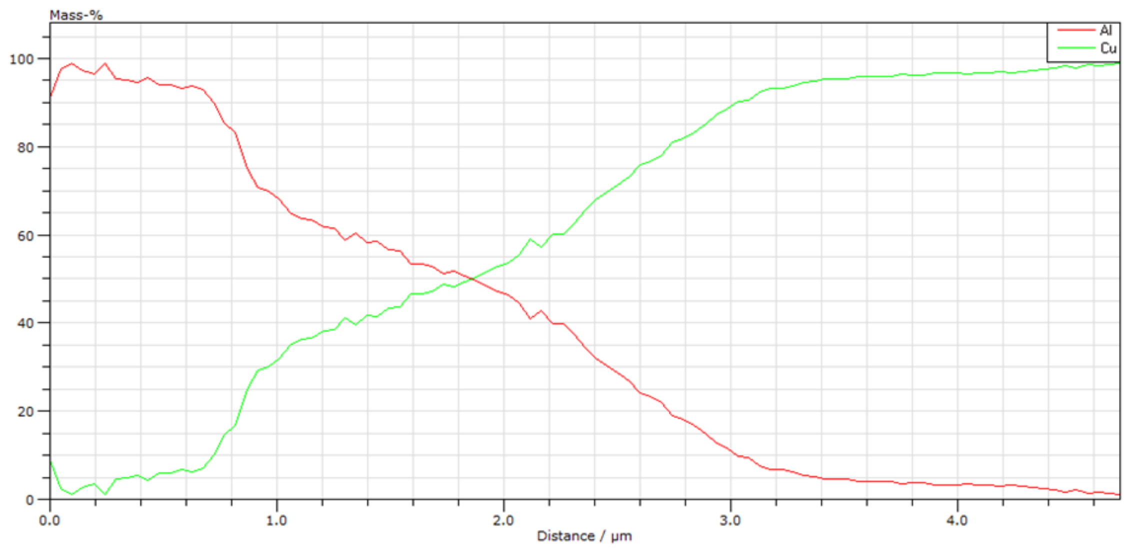

250 °C Heated EDX for 430 hours

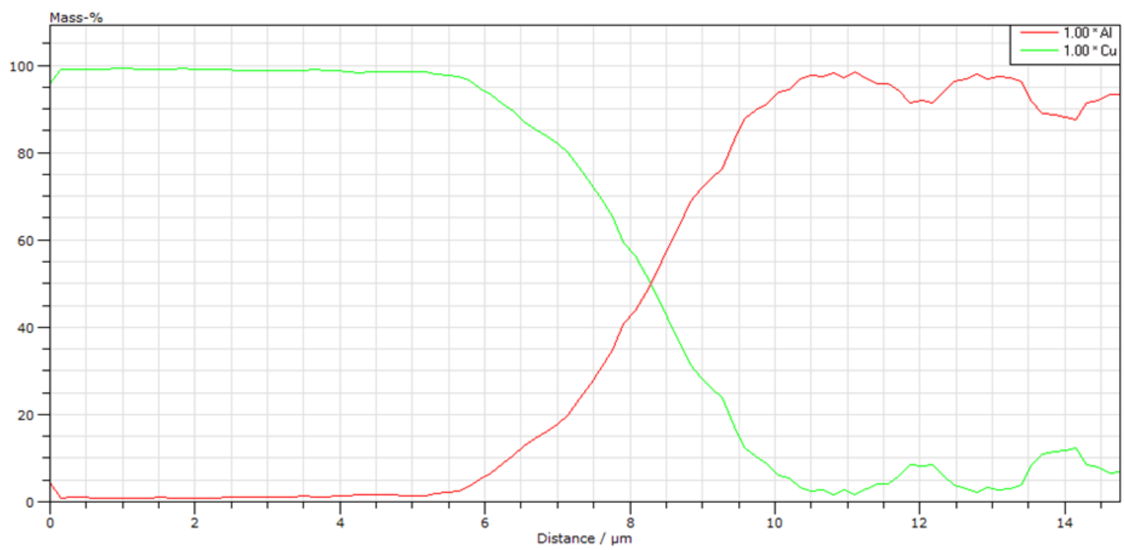

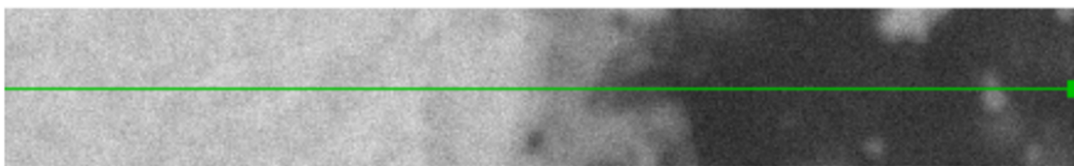

250 °C Heated EDX for 731 hours

M IMC phase characterization

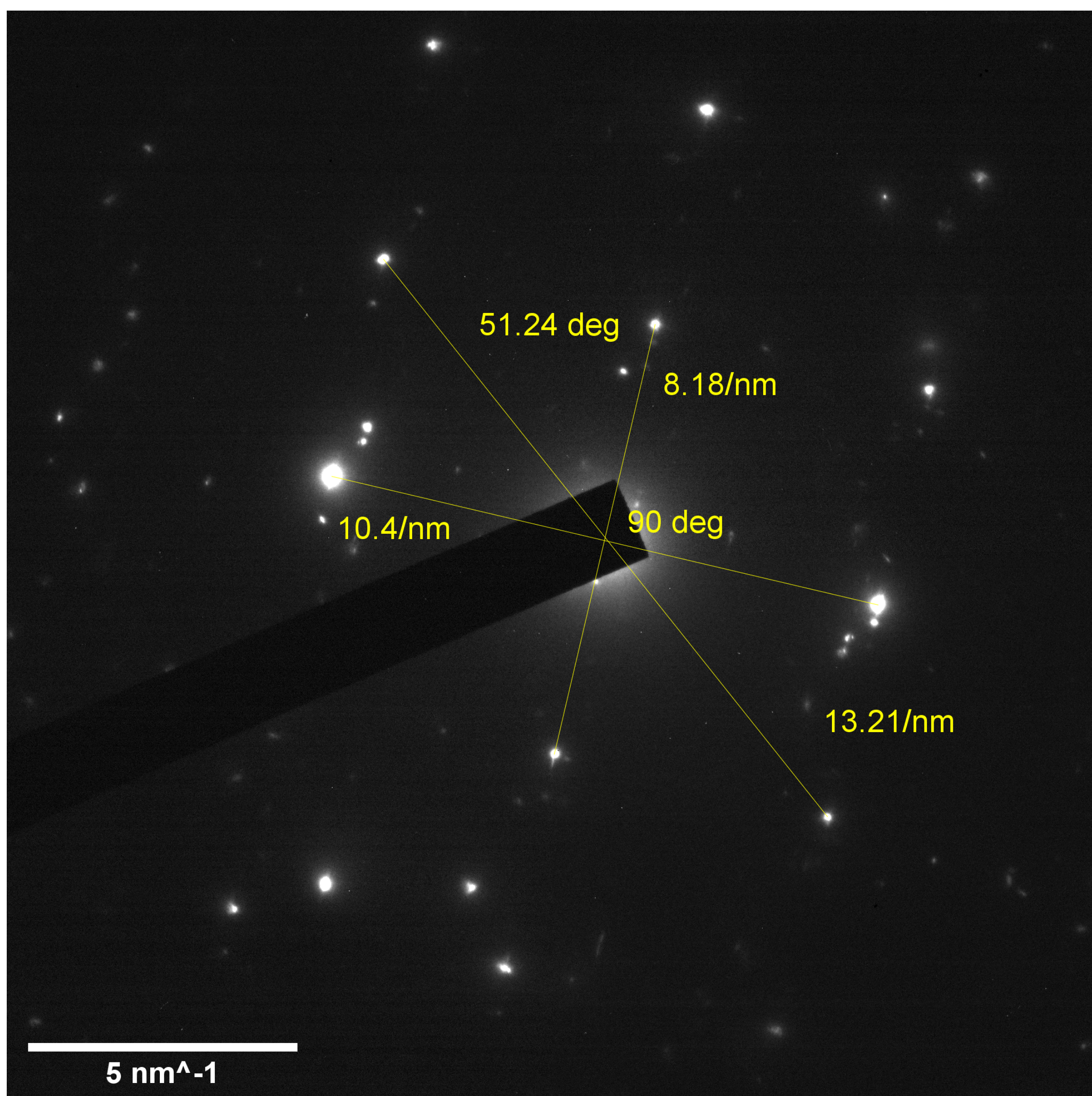

IMC phase characterization

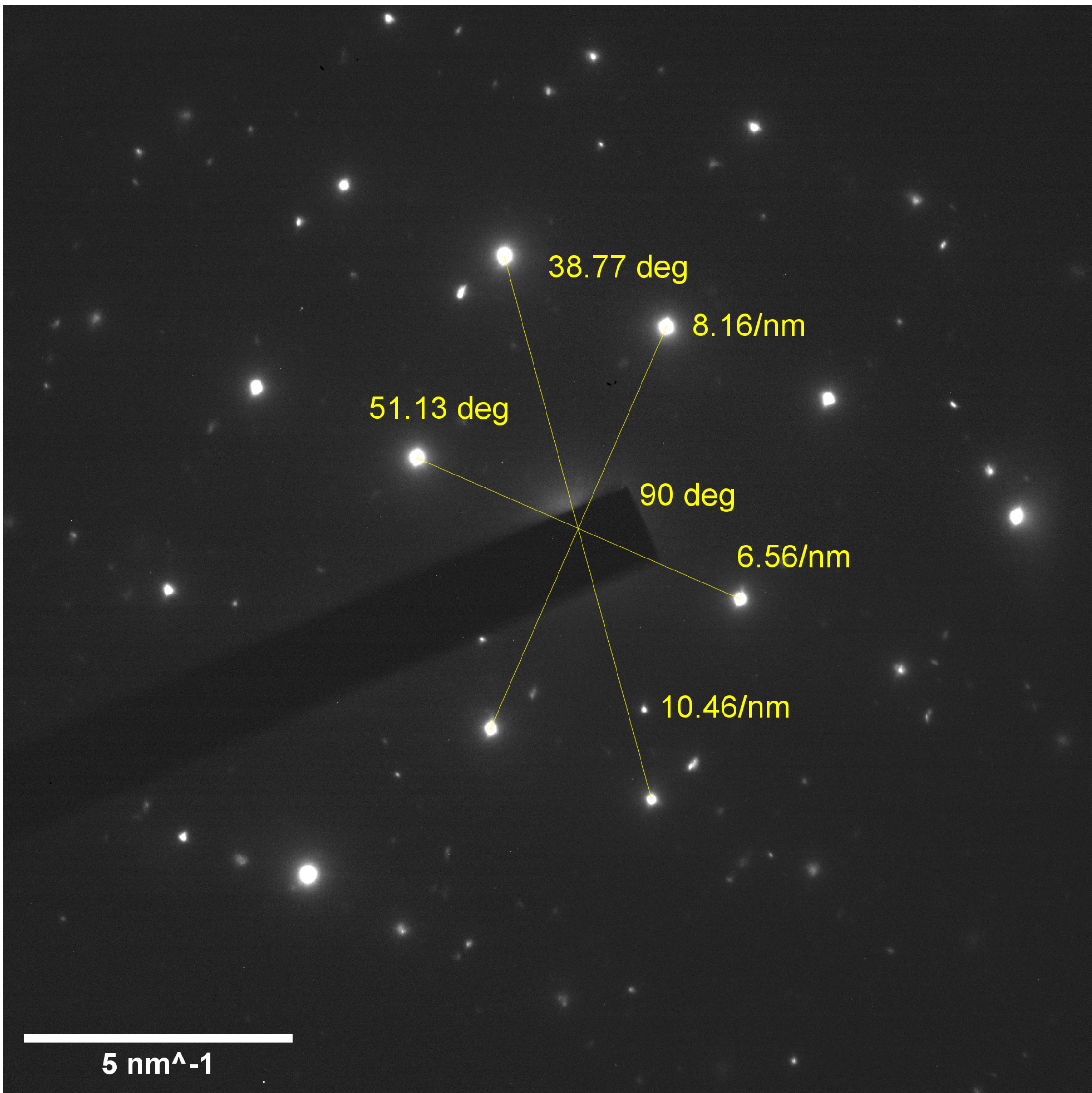

IMC phase characterization

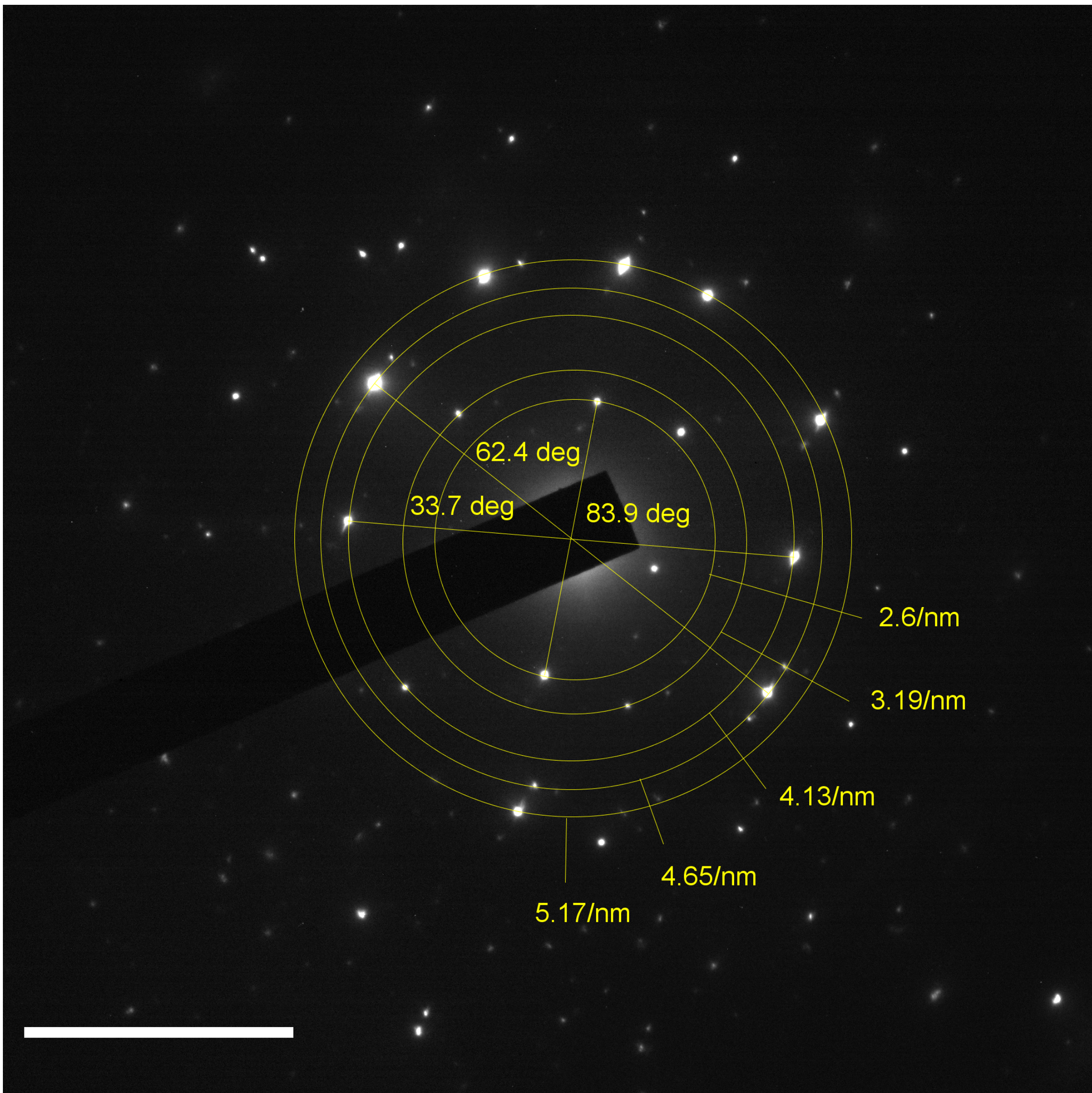

IMC phase characterization

N Excel files

See attached excel files

O Pre-master project

See attached file for pre-master project

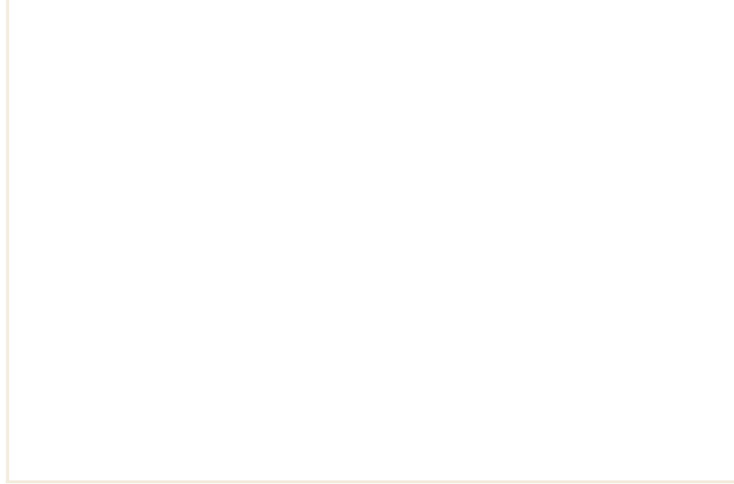

NTNU

Norwegian University of
Science and Technology